Institut für Angewandte Photophysik
Fachrichtung Physik
Fakultät Mathematik und Naturwissenschaften
Technische Universität Dresden

Potential Energy Minimization as the Driving Force for Order and Disorder in Organic Layers

Dissertation
zur Erlangung des akademischen Grades
Doktor der Naturwissenschaften
(Doctor rerum naturalium)

vorgelegt von
Christian Wagner
geboren am 12. August 1979 in Leipzig

Dresden 2010

TECHNISCHE
UNIVERSITÄT
DRESDEN

The electronic version of this document contains hyperlinks that are highlighted for the reader's convenience.

Eingereicht am 21.12.2009

1. Gutachter: Prof. Dr. rer. nat. Karl Leo

2. Gutachter: Prof. Dr. rer. nat. Friedrich Th. Reinert

Verteidigt am 07.06.2010

Abstract

The topic of this work is the structural characterization and theoretical modeling of organic single and heterolayers. The growth of sub-monolayers and monolayers (ML) of the two polycyclic aromatic hydrocarbons quaterrylene (QT) and hexa-*peri*-hexabenzocoronene (HBC) on Ag(111) and Au(111) was investigated. A transition from a disordered, isotropic phase to an ordered phase with increasing coverage was found. The lattice of the ordered phase turned out to be coverage dependent. The intermolecular potential was modeled including Coulomb and van der Waals interaction by a force-field approach. The postulated repulsive character of the potential could be connected to the non-uniform intramolecular charge distribution and to a screening of the van der Waals forces. Furthermore, the influence of the variable lattice constant on the epitaxial growth of HBC was studied. The second part of this work deals with a ML of 3,4,9,10-perylenetetracarboxylic dianhydride (PTCDA) on a ML of HBC. In dependency on the initial lattice constant of HBC, a total of three line-on-line (LOL) and point-on-line coincident phases of PTCDA (with respect to HBC) was found. Following an analysis of the general properties of LOL coincident systems via force-field calculations, a new method to predict the structure of such systems is introduced.

Kurzfassung

Thema dieser Arbeit ist die strukturelle Charakterisierung von organischen Einfach- und Heterolagen sowie deren theoretische Beschreibung und Modellierung. Es wurden Submonolagen und Monolagen (ML) der polyzyklischen Kohlenwasserstoffe Quaterrylen (QT) und Hexa-*peri*-hexabenzocoronen (HBC) auf Ag(111) und Au(111) Einkristallen untersucht und ein Übergang von einer ungeordneten, isotropen Phase zu einer geordneten Phase mit steigender Bedeckung beobachtet. Die geordnete Phase wies dabei bedeckungsabhängige Gitterkonstanten auf. Das intermolekulare Potential wurde unter Berücksichtigung von Coulomb und van der Waals Anteilen mittels Kraftfeldmethoden modelliert. Der postulierte repulsive Charakter des Potentials konnte auf die Ladungsverteilung im Molekül und eine Abschwächung des van der Waals Potentials zurückgeführt werden. Weiterhin wurde der Einfluss der variablen HBC Gitterkonstante auf die epitaktische Relation des Gitters zum Metallsubstrat untersucht. Der zweite Teil der Arbeit widmet sich der Untersuchung einer ML 3,4,9,10-Perylenetetracarboxylic dianhydrid (PTCDA) auf einer ML HBC. Dabei wurden, in Abhängigkeit von der HBC Gitterkonstante, insgesamt drei verschiedene Typen von line-on-line bzw. point-on-line Epitaxie nachgewiesen. Im Anschluss an eine Analyse der generellen Eigenschaften solcher epitaktischer Lagen mittels Kraftfeldrechnungen wird eine neue Methode zur Vorhersage der Struktur konkreter Systeme vorgestellt.

To my family

Contents

1 Introduction

Today, the investigation of organic thin films has become an important field of solid state physics and chemistry. A variety of different aspects like structure, electronic properties, chemical reactivity, and thermal stability are studied. The research extends over bulk properties as well as over properties of organic-inorganic and organic-organic interfaces. The motivations driving these research efforts are numerous. While the hope for better catalysts and sensors triggers the study of chemical properties of interfaces, structure and electronic properties are important aspects for any electronic functionality. Very elaborate layer systems with a complex vertical and sometimes even a lateral structure are currently investigated and produced. They function as organic light emitting diodes (OLEDs), organic solar cells, or organic thin film transistors (OFETs). Advantages of such devices, compared to inorganic semiconductor devices, include low cost, flexibility, and the strong coupling of the aromatic molecules to light. Another motivation for the study of structural and electronic properties of organic adsorbates is given by the hope to create future devices which realize functionality on the smallest scale imaginable. One of the most popular and frequently cited expressions of the hope for control over atomic scale structures is the statement “There’s plenty of room at the bottom” by R. Feynman from 1959. It was perhaps not until the seminal proposal of a single-molecular rectifier by Aviram and Ratner [1] that organic molecules were realized as very suitable buildings blocks of such future devices. Instead of assembling each diode atom by atom in a bottom-up approach or using more and more advanced lithography techniques in a top-down approach, the inherent electronic properties and self-ordering capabilities of tailored organic molecules should be exploited to create complex “molecular electronics”. Although, while several proof-of-concept devices have been successfully developed, the overall progress is probably slower than initially expected. Difficulties creating highly ordered complex assemblies of functional molecules and well defined contacts as well as the thermal stability of such structures are among current problems.

In this work, the structure of monolayer thin films of prototypical organic adsorbates on metal substrates is investigated. Besides the important descriptive part, a major focus is on the modeling of the interaction amongst the adsorbed molecules and between molecules and substrate. The importance of a model description results on the one hand from the aim of gaining a certain predictive power: Findings made for one organic model system should be generalized and made transferable to other systems as well. A quantitative model is, on the other hand, necessary to gain a deeper insight into the basic physical principles that govern (in the present case) the forces between molecules and between molecule and surface.

The molecules studied here comprise hexa-*peri*-hexabenzocoronene (HBC), 3,4,9,10-perylenetetracarboxylic dianhydride (PTCDA) and quaterrylene (QT). HBC and QT are large but compact planar aromatic hydrocarbons which are therefore sometimes called “nano-graphenes”. PTCDA, perhaps the most intensely studied molecule in the field of highly ordered layers, is a perylene derivative that includes heteroatoms, namely oxygen. Most of the thin film investigations described here have been conducted on the close-packed Au(111) single crystal surface, while Ag(111) substrates are used for comparative purpose only. All samples consist of either a single molecular species at sub-ML and ML coverage or two MLs of different molecular species stacked on top of each other. The latter type, an organic-organic heterosystem, is used as a model to study the ordering mechanisms between physisorbed organic layers. The main focus of this work is on the growth of HBC on Au(111) and of PTCDA on HBC on Au(111). Although both systems have been described in literature already, important aspects were missing, and hence the physical principles governing the structure of theses systems remained unrevealed. It turns out that the hydrocarbons HBC and QT do not form ordered islands at sub-ML coverage and possess no fixed lattice constant at ML coverage. Starting from this observation, an important part of this work is dedicated to the creation of a model for the intermolecular interaction between adsorbed HBC molecules and to the question whether epitaxial growth still plays a role in case of a varying overlayer lattice. The question of epitaxial growth, i.e., of a distinct geometric relation between substrate and adsorbate lattice, is also central for the investigation of the heterosystem PTCDA on HBC on Au(111). As a prerequisite for a successful analysis, the principles of epitaxy are rigorously derived from the basic rule of energy minimization. All existing types of epitaxy, commensurate, point-on-line (POL), and line-on-line (LOL), emerge naturally from these considerations. All alignments between PTCDA and HBC lattices found in the heterosystem follow the POL and LOL principles. A link between the specific, tunable properties of the HBC layer and the occurrence of different PTCDA-HBC overlayer structures is established. The present work represents the first observation and analysis of several epitaxial structures in one and the same organic heterosystem. The last major part is therefore dedicated to an analysis of general properties of POL and LOL epitaxy with a strong focus on practical aspects. A “natural order” of different epitaxial structures in terms of potential energy gain is discussed. Proportionality between this gain for the growth on a certain substrate lattice line and the intensity of respective spots in low energy electron diffraction (LEED) is reported and theoretically substantiated. Finally, a method is proposed and implemented that allows a prediction of epitaxial overlayer structures. While numerous methods have already been reported on this subject, the proposed one combines advantages and properties of lattice-matching algorithms and full potential energy calculations. Its major advantage is a combination of an appropriate accuracy and the full overview over the probable epitaxial relations.

Parts of the experiments discussed in this work were performed in our group in the framework of co-supervised diploma theses by Rainer Jacob [2] and Moritz Eßlinger [3].

2 Experimental Methods

Quite naturally, the research results described in this work are highly specialized and represent only a very small fraction of a broad field of research that has been accomplished in the area of organic thin films. In the following two chapters, the basic experimental techniques that were used are outlined and theoretical concepts are presented that are inevitable for the subsequent discussion of the actual experimental and theoretical results.

2.1 Organic molecular beam epitaxy

Organic molecular beam epitaxy (OMBE) represents one possible way to create ordered organic thin films on organic or inorganic substrates under vacuum conditions. OMBE is a type of physical vapor deposition (PVD) which basically means a condensation of previously evaporated material on the sample surface. A related technique is the supersonic molecular beam epitaxy (SuMBE), while other deposition techniques span chemical vapor deposition, pulsed laser deposition, and deposition from the liquid phase. The advantages of OMBE include the precise rate control via a quartz crystal microbalance (QCM) and the very clean ultra-high vacuum (UHV) environment, together with a quite basic setup (compared to SuMBE). The sample preparation requires an evacuated recipient containing the substrate crystal and a so called *Knudsen cell*, which is an elongated crucible made from a chemically inert and thermally stable material (here boron nitride is used) that is wrapped into a filament and surrounded by a metal heat shield. A shutter allows a precise control of the evaporation time and also functions as a heat shield, if closed.

In order to deposit material, the crucible is heated and emits a (weakly) focused molecular beam when the sublimation temperature of the filled-in organic material is reached. The temperature can be used to adjust the molecular flux. If the rate is chosen low enough, it is expected that single molecules instead of larger clusters leave the crucible. Although the term “epitaxy” in OMBE already anticipates an ordered or even epitaxial growth of the material condensed on the substrate, this is not necessarily the case but depends on the chosen substrate material, crystallinity, temperature, and, as will be discussed later, the coverage. As a general rule, a higher substrate temperature

Figure 2.1: Often, town planing follows the principles of Stranski-Krastanov growth: wetting layer and islands.

increases the mobility of the adsorbed molecules which might foster the ordering process, but may also lead to disorder (increasing the entropy of the film), or the growth of 3-dimensional crystals instead of thin films [4]. Furthermore, the condensation probability (and thus the effective deposition rate) decreases with increasing substrate temperature.
Three specific types of molecular growth can be distinguished:

- *Volmer-Weber* [5] or *island growth* occurs if the intermolecular interaction outweighs the molecule-substrate interaction. The molecules grow in single crystals, not wetting the entire substrate which primarily works as a support holding the crystals.

- *Frank-van der Merwe* [6] or *layer-by-layer growth* is characteristic for the opposite case of strong molecule-surface interaction. Here, the surface is entirely covered with molecules and the second layer starts to grow by the time the first layer is fully closed. This growth principle is maintained for a large number of layers. Either the molecules grow in their bulk crystal structure already in the first layer, or the growth of the native crystal structure is inhibited even for a large layer thickness. In the latter case, the structure is often determined by the orientation of the first layer, which is in turn influenced by the substrate.

- *Stranski-Krastanov* [7] or *island-on-layer growth* is situated in between the two types discussed so far and combines a wetting layer with subsequent island growth (Fig. 2.1). A characteristic candidate for Stranski-Krastanov growth is the molecule PTCDA. If the layers are prepared

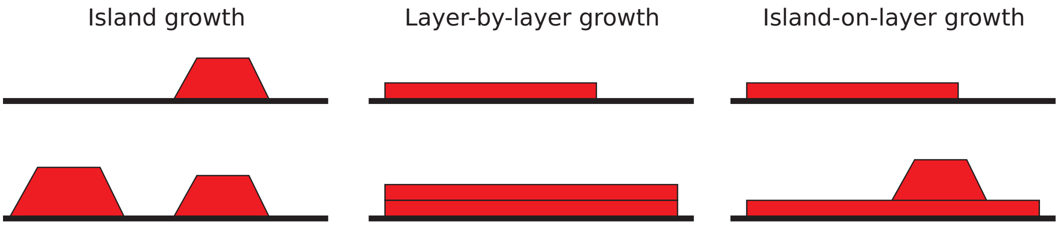

Figure 2.2: Scheme of the different growth modes observed for organic adsorbates. The nominal coverage is 0.7 ML (upper row) and 2.0 ML (lower row).

> by deposition of the molecules at room temperature followed by thermal annealing, PTCDA exhibits Stranski-Krastanov growth on the metallic substrates Cu(110), Cu(111) and Au(111) [8].

All three growth modes are summarized graphically in Fig. 2.2. The different molecular species discussed in this work, as well as the substrates used in the OMBE process, will be briefly introduced in Section 2.4 together with mentioning relevant results from literature.

2.2 Scanning tunneling microscopy (STM)

The invention of the scanning tunneling microscope (STM) in 1982 by Binnig and Rohrer [9] opened up the possibility to investigate the topography and electronic properties of a conducting sample at atomic resolution. It takes advantage of the quantum mechanic tunneling effect that allows small particles, e.g., electrons to pass “through” potential energy barriers they would be unable to overcome in classical physics. The effect is a consequence of the finite norm of the wave function in classically forbidden regions. A detailed theoretical study of these charge transport processes that is aimed for a better understanding of tunneling spectroscopy data has been performed. The respective discussion can be found in the Appendix as it is not directly related to the scope of this work. In this section the practical use of the STM is in the focus. A very broad description of all major applications of the STM can be found in Ref. 10.

A commercial STM-1 (Omicron) operating at room temperature was used in this work to record the STM images. The STM was exclusively operated in the constant-current mode, where a feed-back loop is employed to maintain a pre-defined value for the tunneling current while scanning. The feed-back thus continuously adjusts the tip-sample distance following an iso-conductance surface or “z-map”. A typical STM image of a HBC ML on Au(111) and the corresponding tunneling current image is displayed in Figure 2.3. Several corrections have been applied to the raw images. If the sample surface is macroscopically inclined, a wedge is superimposed on the z-maps. As this

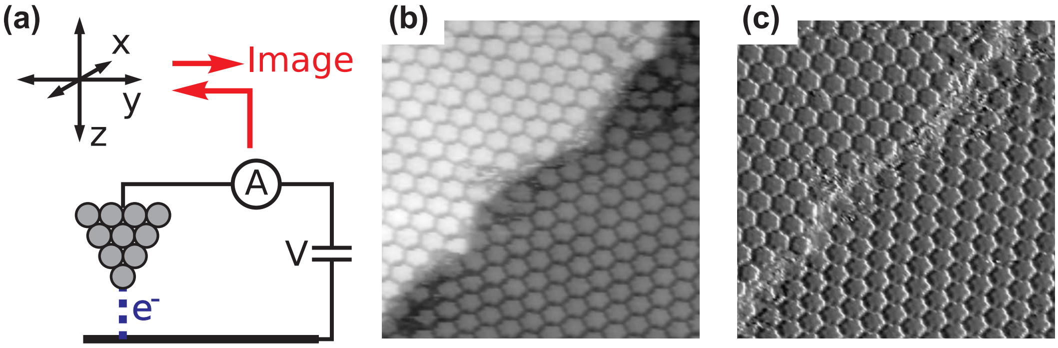

Figure 2.3: **(a)** In a STM the sample is scanned by a tip while holding the (average) tunneling current constant. **(b)** Topographic information, i.e., a map of z-displacement values. **(c)** Map of the tunneling current in constant-current mode. The information in this map is due to the finite response time of the feed-back control.

easily masks the relevant information, it is removed by fitting the image with a plane that is subsequently subtracted. The software WSxM [11] was used to tune the image contrast.

The STM images are usually distorted. Reasons for such a distortion include thermal or mechanical drift and nonlinearities of the piezo scanner. Any constant drift can be removed from an image by comparing the positions of eye-catching objects in two subsequent images. As the nonlinearity can, however, not be compensated a posteriori, the STM is not the tool of choice for measuring the absolute size of objects or lattices.

An important subject of STM investigations in this work are organic heterolayers consisting of two different molecular species in a vertical stack. As mentioned above, STM images represent iso-conductance surfaces of the scanned area. As conductance means the tunneling probability *and* the conductivity of the sample surface, the information obtained is a mix of topographic and electronic properties. As the (local) conductance path *through* an organic multilayer system is mainly coupled to overlapping π-systems, it is obvious that the conductance holds information about all participating layers. While in thicker films the information from deep layers is averaged out, as the electrons take different paths,[1] it is fully preserved in case of a two monolayer (ML) system like the ones investigates here. This ability to look "beneath" the surface is an advantage of the tunneling microscopy method in contrast to force microscopy methods which are sensitive to total electron density, i.e., topographical information, and not to conductance.

---

[1] In the simple picture of a 2D brick wall arrangement of molecules in subsequent layers, an electron can always "choose" between two molecules on each step closer to the substrate, leading to a Galton's Board-like behavior of the conductance paths.

2.3 Low-energy electron diffraction (LEED)

The low-energy electron diffraction (LEED) method is, like other diffraction methods, based on the dual nature of quantum mechanical objects which have characteristic properties of particles as well as waves. The probes used in LEED are monochromatic electrons emitted from a heated filament (here: LaB_6) and accelerated to an energy E_0 between a few eV and a few hundred eV. As free particles, they can be described by (complex) plane waves

$$\Psi(\mathbf{r}, t) = A_0 e^{i(\omega t - \mathbf{kr})}. \tag{2.1}$$

The suitability of such low-energy electrons for the investigation of surface structures results from their specific wavelength, as well as from their surface sensitivity (low penetration depth). With the nonrelativistic dispersion relation for a free electron $E = \hbar^2 k^2 / 2m$, one obtains velocities of

$$1 \cdot 10^6 \, \frac{\mathrm{m}}{\mathrm{s}} < v < 1 \cdot 10^7 \, \frac{\mathrm{m}}{\mathrm{s}}$$

and with $\mathbf{k} = \mathbf{p}/\hbar$ wavelengths λ of

$$5\,\text{Å} > \lambda > 0.5\,\text{Å},$$

i.e., of the same order of magnitude than typical surface lattice constants. The penetration depth is, due to the strong Coulomb interaction, in the order of a few Ångstrom only [12]. Specific theoretical considerations on the occurrence and interpretation of LEED patterns are, for sake of clarity, given in Section 3.1 together with a general discussion of reciprocal space and the Fourier transform. Here, the focus shall be on the instrumentation and data evaluation.

Instrumentation

The LEED instrument used in this work is a commercial four-grid display-type system fabricated by Omicron which follows the basic design concept of spherical screen and grids introduced by Lander [13] (Fig. 2.4). The electrons emitted from the LaB_6 filament are accelerated to the desired kinetic energy $E_0 = eV_0$ and focused by a system of electrostatic lenses onto the sample crystal. The backscattered electrons pass a total of four grids. The inner grid, kept at ground potential, provides a field-free region around the sample, while inelastically scattered electrons with $E < E_0$ are repelled by the negative potential of the retarding grids that is just above V_0. Finally, the remaining electrons are accelerated onto a fluorescent screen kept at a high positive potential of 7 kV. The LEED pattern is recorded by a standard CCD camera mounted in front of the screen.

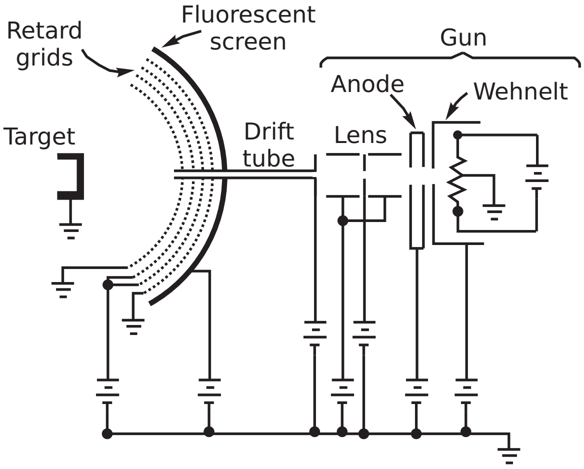

Figure 2.4: This scheme, adapted from Refs. 13 and 14, illustrates the LEED setup used. Electrons emitted from a filament are focused by a system of electrostatic lenses onto the sample crystal. The backscattered electrons pass a total of four grids (inelastically scattered electrons with $E < E_0$ are repelled by the negative potential of the retarding grids) until they are finally accelerated onto a fluorescent screen kept at a high positive potential.

Data evaluation

As the diffracted electrons are visualized on a fluorescent screen, a loss of phase information occurs that prohibits the direct calculation of the real space lattice from the LEED pattern. Instead, the analysis has to be performed in a forward approach by calculating the LEED pattern for a model overlayer. Starting with an initial guess, this model is adjusted iteratively until the simulation fits the experiment sufficiently well. As meaningful initial parameters are required, LEED can be used effectively only in combination with a real-space imaging technique that reveals the rough composition of the unit cell, i.e., number and orientation of molecules.

Here, the commercially available software LEEDSim by S. C. B. Mannsfeld [15] has been used to evaluate the acquired LEED patterns. The PTCDA and HBC overlayers discussed in this work exhibit either a rectangular or a hexagonal unit cell. Hence, the unit cell dimensions a_1 and a_2 can be derived directly and without simulation by measuring the distances $r_{1,2}$ of the (10) and (01) Bragg reflexes to the zero order spot in the LEED pattern. As these lengths scale inversely to the respective lattice constants $a_{1,2} = C \cdot r_{1,2}^{-1}$, a direct conversion is possible if the voltage-dependent scaling factor C is known. For the purpose of a precise evaluation of a large number of LEED patterns, the following route was hence taken:

- All LEED patterns were recorded with an electron energy of 10.4 eV.
- The scaling factor C was calculated for *one* pattern by means of a LEEDSim analysis.

- All other images were analyzed by using a graphics software to measure $r_{1,2}$.

Besides the speed gain, this procedure significantly increases the accuracy of the derived data. By increasing the zoom level, the center of gravity of each spot could be located with very high precision. Especially a quantitative comparison of different structures found in one and the same LEED image is possible with an accuracy that exceeds the absolute accuracy of the analysis by far. The following part is dedicated to a summary of all important experimental errors in the performed LEED analysis.

Experimental errors

In order to derive accurate information on the size of the unit cell, the LEED system needs to be calibrated by a sample of known geometry. Here, the absolute scaling was performed using the LEED pattern of a Au(111) crystal taken at 205 eV. Two additional corrections have to be applied to allow a quantitative evaluation of a recorded pattern:
(i) The image distortion caused by the lens of the CCD camera is corrected using a software tool by S. C. B. Mannsfeld that was initially calibrated by means of a 7×7 reconstructed Si(111) crystal [16].
(ii) The displayed primary electron beam energy is corrected according to a method proposed by Günther [17]. To do so, the distances $d(V_0)$ between opposite first order spots in the hexagonal LEED pattern of a HBC ML on Au(111) were measured for several voltages V_0. The corrected voltage $V_{corr} = V_0 + V_{\text{offset}}$ has been estimated from a linear extrapolation of $d^{-2}(V_0)$ as this fit intersects the abscissa at $-V_{\text{offset}}$. A value of $V_{\text{offset}} = -1.2\,\text{V}$ was found in accordance to earlier works employing the same LEED apparatus [16]. Here, all LEED energy values denoted E_0 refer to *corrected* energies.

The result of every LEED pattern analysis is subject to a number of possible errors which are listed below together with a specification of their estimated magnitude in square brackets. Additionally, absolute values in Ångstrom are given for the exemplary parameters $E_0 = 10.4\,\text{eV}$ and $a_1 = 15\,\text{Å}$.

1. Uncertainty of the primary energy of the electrons E_0 which is displayed with an accuracy of 0.1 eV by the instrument. [$\Delta E = \pm 0.05\,\text{eV}$, $\Delta a_1 = \pm 0.036\,\text{Å}$]

2. The mentioned correction of the primary energy by an offset eV_{offset}. [$\Delta E = \pm 0.05\,\text{eV}$, $\Delta a_1 = \pm 0.036\,\text{Å}$]

3. Occasionally, an asymmetry in the LEED patterns at low energies occurred. This effect is probably caused by electrostatic charging of parts of the sample holder as sputtering reliably puts an end to this problem. Nevertheless, sputtering was not always feasible. [$0.003 < |\Delta d/d| < 0.02$, $0.05\,\text{Å} < |\Delta a_1| < 0.3\,\text{Å}$]

4. Measuring of the actual spot position by means of a graphics software. Here, the main problem is the width of the spots. Always the center of a broad spot has been selected for the measurement. [$0.0015 < |\Delta d/d| < 0.005$, $0.02\,\text{Å} < |\Delta a_1| < 0.08\,\text{Å}$]

5. The error from connecting relative to absolute values by means of the calibration by an Au(111) LEED pattern. Here, all the above mentioned errors have to be included. [$\Delta d/d = \pm 0.004$, $\Delta a_1 = \pm 0.06\,\text{Å}$]

Three different types of investigations can now be distinguished which are subject to different errors:

- Comparison of lattices in *one and the same* LEED pattern. Here the error is minimal. It arises only from points 3 and 4 in the list given above.

- Analysis of differences in the absolute lattice constants extracted from *different* LEED measurements (like "lattice constant increased by 0.2 Å"). Here, the absolute scaling error as well as the error of eV_{offset} is canceled out.

- The absolute lattice constant values given in this work have the largest error interval as they are subject to all mentioned errors. The error ranges from $\Delta a_1 = \pm 0.2\,\text{Å}$ to $\Delta a_1 = \pm 0.45\,\text{Å}$ depending on the sharpness of the respective LEED pattern.

The instrumental limitations of a LEED setup are given by the instrument response function [18] and can be summarized in form of a transfer width equal to an effective coherence length. Surface structures with a lateral separation larger than the coherence width of the incident electrons essentially produce no interference but simply add intensity to the LEED pattern. In turn, electrons scattered from a surface consisting of many small domains ($1\,\text{nm} < d < 10\,\text{nm}$) do interfere, weakening the spot intensity and sharpness. A sharp and bright LEED pattern is therefore indicative of a high surface quality with large uniform domains. In the setup used, the coherence length is $\approx 30\,\text{nm}$ at $100\,\text{eV}$ [14].

2.4 Molecules and substrates: Basic properties and literature review

The topic "Investigation of organic thin films on metal substrates" allows to study a theoretically almost unlimited variety of possible systems, as the number of organic chemical compounds is enormous. Therefore, the question which molecular species to select and why to do so, is rather important. Several aspects were considered when selecting the molecules discussed in this work:

- **Size/Thermal stability:** As the OMBE method is used to deposit the organic films, and as the investigation is performed at room temperature, constrains exist concerning the size and thermal stability of the molecules: They need to stay intact during the sublimation process (which is not given for very large or branched molecules), and the sublimation temperature should be significantly above room temperature to allow the condensation on the substrate (which is not given for small organic compounds).

- **Shape:** Although non-planar molecules are also a rewarding field of research and exhibit remarkable physical properties on surfaces, only planar molecules have been selected for this work. The growth of highly ordered single- and heterosystems, consisting of MLs of one or more organic species, constitutes a major topic here. Consequently, the use of planar, π-conjugated molecules is probably the best option as it is expected to foster the growth of different organic species on top of each other. It also reduces the degrees of freedom severely, as no sterical distortion has to be considered.[2] Furthermore, the use of planar molecules allows to profit from the large experience accumulated in our research group concerning the epitaxial growth of this particular type of molecules.

- **Comparability:** As the amount of physical properties and effects related to organic molecules in crystals or thin films is quite remarkable, and also the number of techniques used to investigate these properties is large, one significantly profits from using a material which is or was already under investigation. This allows accessing a large number of published results. Only in doing so, a deep understanding of the complex relations and thus access to subtle effects is possible. The most well-known compound under investigation here is PTCDA, while there are much less publications on thin film properties of quaterrylene.

---

[2] The carbon body of the molecules stays practically flat upon adsorption on Au(111), while non-planar molecules may distort significantly.

2.4.1 3,4,9,10-Perylenetetracarboxylic dianhydride

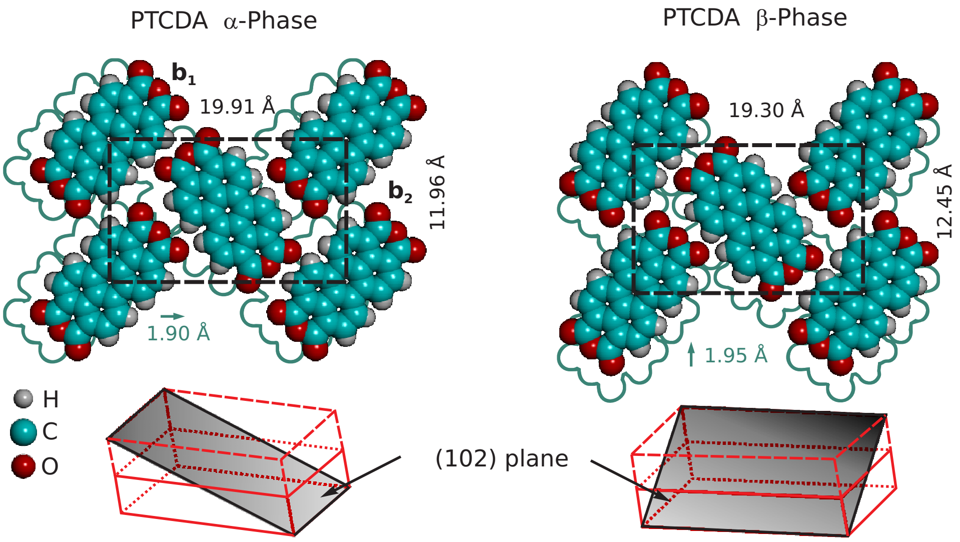

Figure 2.5: Illustration of the bulk lattice of PTCDA in the α and β modification with a focus on the (102) plane that features coplanar and in-plane PTCDA molecules. The stacking of the (102) planes is indicated by the silhouettes of molecules in the plane right below. The lower part of the figure shows the position of the (102) plane in the bulk lattices of both modifications [19].

PTCDA is a substituted polycyclic hydrocarbon, a perylene derivative with six oxygen heteroatoms (Fig. 2.5). It is commercially available[3] and mainly used as a red pigment in industrial applications. In the context of fundamental research, it is probably the most widely studied molecular species in the field of organic layers.

Initially, investigations of PTCDA were triggered by the semiconducting properties of this molecule in the bulk phase. It was utilized in the creation of a contact barrier diode by evaporating 100 nm-200 nm PTCDA on p-type silicon [20]. This basic property, a band gap in the region of the visible light, is also the reason why many of the molecules investigated in the context of organic electronics serve as dyes in industrial applications.

The bulk structure of PTCDA was first studied by Forrest (Ref. 21 and references therein). Due to its crystal structure PTCDA possesses a large anisotropy in the conductivity with the conductivity being highest in the direction perpendicular to a substrate surface [22]. This is optimal for the use in a sandwich configuration, being one of the reasons for the initial research interest in PTCDA.

Details on the bulk crystal structure have been reported by Moebus et al. [23] and Ogawa et al. [19] (Fig. 2.5): The individual PTCDA molecules are

---

[3] The PTCDA used in this work has been obtained from Sigma Aldrich, Taufkirchen, Germany and purified by temperature-gradient vacuum sublimation.

almost coplanar and oriented parallel to the (102) plane of the monoclinic crystal (space group $P2_1/c$) [23]. Furthermore, the two molecules in the unit cell have no displacement perpendicular to this plane. The (102) facet of a PTCDA crystal features, in other words, molecules packed as shown in Fig. 2.5. Quite naturally, the motif of PTCDA thin films bears a strong resemblance to the arrangement in this specific plane. Two different polymorphs of PTCDA single crystals are reported in literature that exhibit slight differences in the dimensions of the unit cell, the molecular orientation, and the stacking of subsequent (102) planes (Fig. 2.5).

PTCDA on decanethiol on Au(111) was one of the first reported organic-organic heterosystems consisting of MLs only [24]. In-plane organic heterosystems or "mixed layers" employing PTCDA were reported by Bobisch et al. (CuPc and PTCDA on Cu(111)) [25]. These particular systems only appear if the CuPc is evaporated first, while for the inverse sequence, PTCDA islands are obtained which do not reorganize, indicating a high stability of the PTCDA domains. Organic-organic heteroepitaxial systems using the very same molecular species were reported by Chen et al. (PTCDA on CuPc on graphite) [26]. The bonding height of PTCDA on Au(111) and Ag(111) was reported by Henze et al. [27]. PTCDA grows on most substrates in the herringbone phase, similar to the (102) bulk plane. Exceptions are the growth of PTCDA on the highly corrugated Ag(110) surface where a brick-wall structure is observed [28] and the square-phase observed on Au(111) [29].

2.4.2 Hexa-peri-hexabenzocoronene

Hexa-*peri*-hexabenzocoronene (HBC) is a hexagonal-shaped polycyclic hydrocarbon.[4] To check for a potential application of HBC derivatives in organic solar cells, the photoinduced electron transfer in a donor-acceptor system was studied [30]. The single-crystal structure of unsubstituted HBC has been derived from X-ray diffraction [31]. Figure 2.6 shows its monoclinic lattice (space group $P2_1/a$) that is characterized by alternating stacks of strongly inclined molecules. The two molecules that form the basis of the lattice are marked in purple. In a closed ML, HBC grows planar in a hexagonal arrangement on most substrates [32–35]. Recently, also studies of HBC on Au(111) at very low coverage have been performed, showing a non-planar adsorption at step edges in face-centered cubic (fcc) regions [36, 37].

HBC holds a prominent position as a first layer in several organic-organic heterosystems. A phase of PTCDA on HBC on graphite was described by Schmitz-Hübsch et al. [38], and later explained in terms of line-on-line epitaxy by Mannsfeld et al. [39]. HBC on Au(111) has been used as template for the heteroepitaxial growth of PTCDA and quaterrylene [40–42]. Often substi-

---

[4] HBC was provided by Prof. K. Müllen, MPI für Polymerforschung, Mainz, Germany.

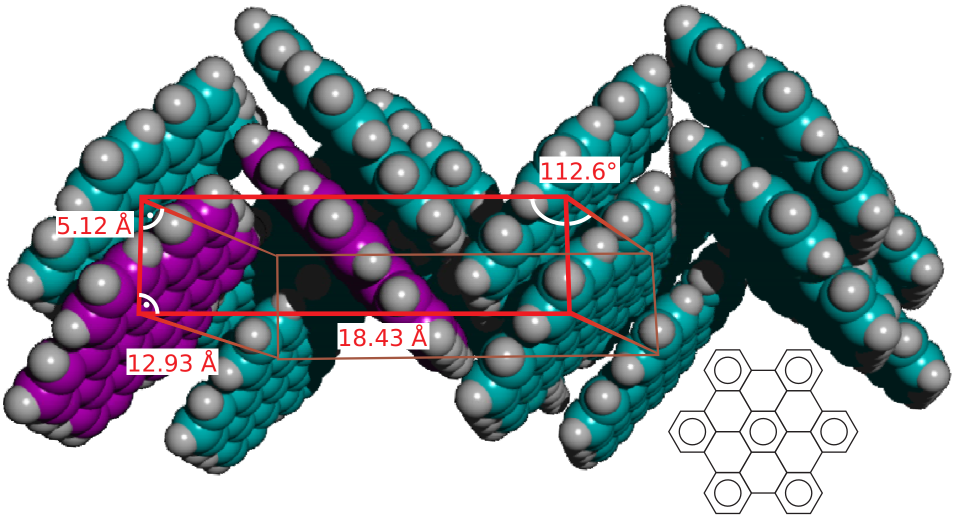

Figure 2.6: Illustration of the bulk crystal structure of HBC. The basis of the lattice consists of two molecules oriented almost perpendicular to each other as indicated in purple. In contrast to PTCDA, no plane of coplanar molecules exists in the HBC bulk [31].

tuted HBC molecules which, among other properties, offer a higher solubility compared to the unsubstituted species, are subject to investigation [43–45].

2.4.3 Quaterrylene

Quaterrylene (QT) is an unsubstituted polycyclic hydrocarbon consisting of four naphthalene units.[5] Quaterrylene derivatives have the capability to absorb and even emit light in the near infrared [46] making them interesting for specific organic-electronics applications [47, 48]. They are currently used as coating for heat protection glass [49]. The first accurate determination of the bulk crystal structure (space group $P2_1/a$) by X-ray data was reported by Kerr et al. [50] (Fig. 2.7). Compared to PTCDA and HBC, only little thin-film data is available for quaterrylene [51, 52]. As in the case of HBC, the poor solubility of QT results in a focus on substituted species [53]. Several nm thick films of QT on KCl were investigated by Maeda et al. using high-resolution TEM [54]. The ML and double layer growth on Au(111) was investigated by Franke et al. [55]. The optical absorption of these films has been studied by Roman Forker [56]. QT was successfully used as the second layer in the organic-organic heterosystems QT on HBC on Au(111). For this system, an electronic decoupling between QT and Au(111) was found by optical absorption measurements [41]. The epitaxial relation between QT and HBC follows the line-on-line principle [42].

---

[5] QT was purchased from Dr. W. Schmidt, Institut für PAH-Forschung, Greifenberg, Germany.

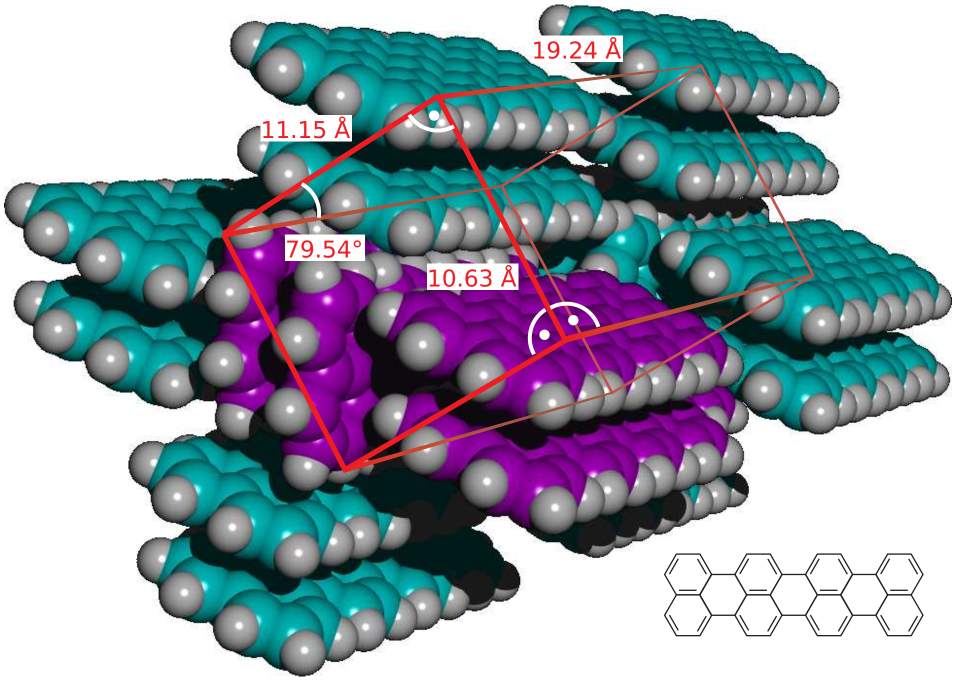

Figure 2.7: Illustration of the bulk crystal structure of QT [50]. The basis of the lattice consists of four molecules arranged pairwise in a sandwich motif [57] (purple). The two pairs are oriented almost perpendicular to each other and hence no plane of coplanar molecules exists in the QT bulk phase.

2.4.4 Metal substrates: Au(111) and Ag(111)

Metals posses a well defined crystal structure, which, in comparison to covalent crystals, is formed by packed ion cores and a free electron gas. As the metal atoms are free of restricting bond angles, a high packing density is usually achieved, resulting in body centered cubic (bcc), face centered cubic (fcc), and hexagonal close packed (hcp) structures. The Au crystal has a fcc structure with a lattice constant of 4.079 Å [58]. Hence, the Au(111) *bulk* plane has a hexagonal symmetry with a primitive lattice vector length of 2.884 Å.

A surface means a disturbance in the high periodicity of a crystalline structure and results in two major changes in its properties, compared to the bulk crystal. First, the density of electronic states (DOS) at the surface is different from the bulk DOS due to the existence of *surface states* which decay exponentially into the bulk. Second, the relief of surface stress [59] leads to a rearrangement of the topmost atomic layer of Au(111), the so-called *surface reconstruction*. In combination with the underlying bulk structure, a characteristic Moiré pattern is created, which can be observed in STM as the stacking changes from fcc (ABCABC...) to hcp (ABAB...) and back [16] (Fig. 2.8). As the lattice vectors of the overlayer are parallel to those of the bulk surface, the reconstruction can be described in the “Wood-notation”, i.e., the two numbers u and v for which $\mathbf{A}_1 = u \cdot \mathbf{a}_1$ and $\mathbf{A}_2 = v \cdot \mathbf{a}_2$. In this notation a $22 \times \sqrt{3}$ re-

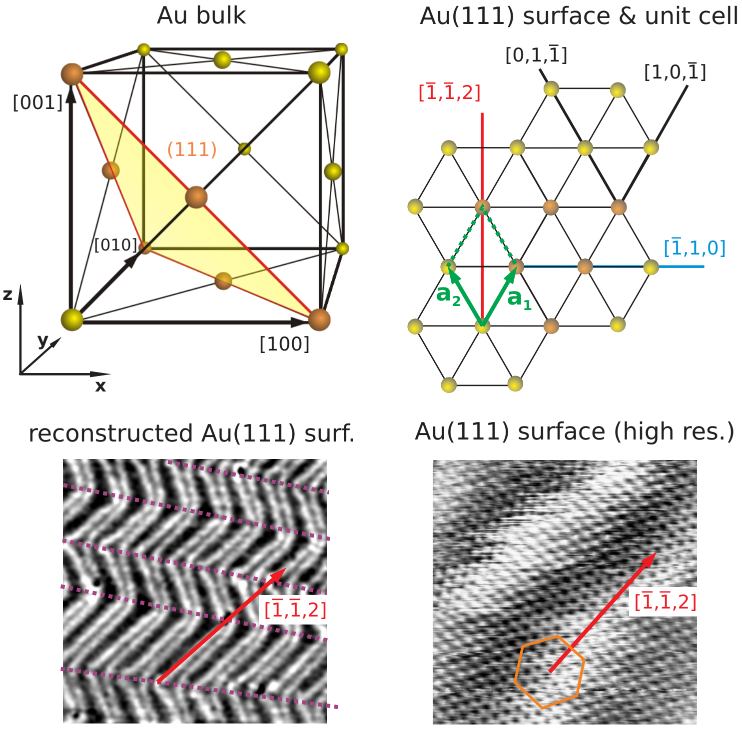

Figure 2.8: Crystal structure of the Au(111) surface. The reconstructed surface lattice is compressed along the $[\bar{1},1,0]$ direction (blue). In the $[\bar{1},\bar{1},2]$ direction (red), the lattice is uncompressed. Consequently, the Moiré stripes in the STM images are parallel to the $[\bar{1},\bar{1},2]$ direction. The boundaries between the different rotational domains are indicated by dotted purple lines. In this work, the Au(111) unit cell is defined by the vectors $|\mathbf{a}_1| = |\mathbf{a}_2|$ (green) that enclose the $[\bar{1},\bar{1},2]$ direction and an angle of $\alpha = 57.82°$.

construction is observed for the bare Au(111) surface, meaning a compression of the surface lattice parallel to one of its primitive vectors by about 4 %. The $22 \times \sqrt{3}$ reconstruction is accompanied by a buckling of the top layer with a vertical amplitude of ≈ 0.15 Å [60]. Moreover, the distance between the terminal and the second atomic layer of Au(111) increases by $\approx 3\,\%$ compared to the spacing of $(111)_{Au}$ planes in the bulk [60].

The original six-fold symmetry of the surface is then replaced by three equivalent rotational domains with a mirror plane each. On a well-prepared Au(111) surface, two of the three rotational domains are alternating, each with a stripe-like shape, resulting in the characteristic zigzag Moiré pattern which is shown in Figure 2.8. The stripes of the rotational domains are not identical to the stripes of the Moiré pattern of the reconstruction and usually much broader. The reconstruction of the Au(111) surface is also reflected in LEED patterns of a well-prepared crystal. Electrons which are diffracted by the first layer *and* the bulk create the characteristic side-spots visible in Fig. 2.9.

The bulk crystal structure of Ag is very similar to that of Au. It has a fcc structure with a lattice constant of 4.09 Å [58]. Hence, the Ag(111) bulk plane

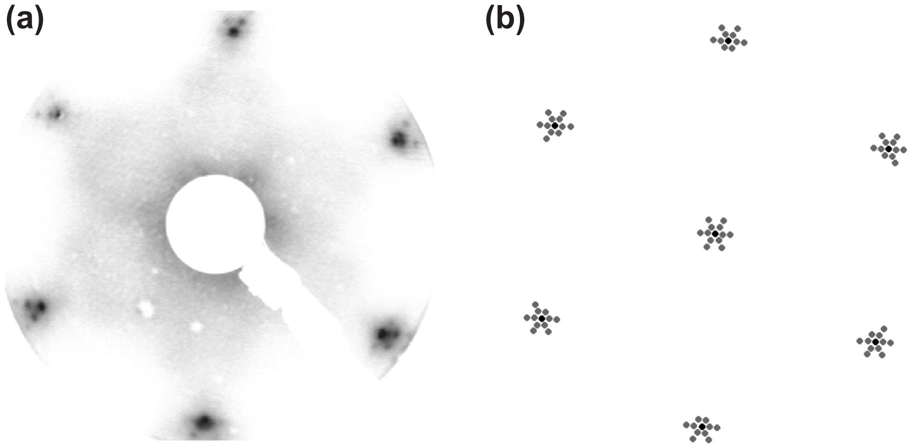

Figure 2.9: **(a)** LEED pattern of a clean, reconstructed Au(111) single crystal surface ($E_0 = 58.1\,\mathrm{eV}$). Visible are first order spots which are surrounded by first and second order double-scattering spots. **(b)** Geometric LEED simulation of (a), including double-scattering processes.

has a hexagonal symmetry with a primitive lattice vector length of 2.889 Å. In contrast to Au, the Ag(111) surface is not reconstructed, i.e., the hexagonal symmetry is kept. Both single crystal substrates,[6] Au and Ag, were cleaned by up to three cycles of Ar^+ sputtering ($E = 600\,\mathrm{eV}$) and annealing.

---

[6] Metal single crystals have been purchased from MaTecK GmbH, Jülich, Germany.

3 Theory and Modeling

A theoretical description of physical phenomena is important for a deeper understanding of the underlying mechanisms as well as in order to gain a certain predictive power. In this chapter, the focus is put on two specific aspects that are of high importance for this work. The first one deals with an adequate interpretation of LEED measurements and the limits of such a description. The second topic resides in the large field of computational chemistry. Here, a quantitative model for the potential energy of organic adlayers is discussed.

3.1 Reciprocal space and LEED theory

3.1.1 Fourier transform and geometrical LEED theory

The Fourier transform $F(k)$ of a one-dimensional function $f(x)$ is defined in a "conjugated" space that is linked to the function $f(x)$ in "real" space by the expression:

$$F(k) := \frac{1}{2\pi} \int\limits_{-\infty}^{\infty} f(x) e^{-\mathrm{i}kx} dx, \tag{3.1}$$

and vice versa

$$f(x) := \int\limits_{-\infty}^{\infty} F(k) e^{\mathrm{i}kx} dk, \tag{3.2}$$

which means an expansion of the original function into (standing) plane waves with continuous wavelengths $\lambda = 2\pi/k$ and amplitudes $F(k)$. Typical combinations of domains for $f(x)$ and $F(k)$ are time vs. frequency or real space vs. reciprocal space. The latter case contains the definition of the reciprocal lattice used in crystallography as will be outlined now. If $f(x)$ is a periodic function with a periodicity a, only plane waves with this periodicity contribute to the expansion.

$$F(k) = \frac{1}{2\pi} \int\limits_{-\infty}^{\infty} \sum_n f(x) \delta(k - nk_a) e^{-\mathrm{i}kx} dx, \tag{3.3}$$

with $k_a = 2\pi/a$. Hence, $F(k)$ is no continuous function anymore, but a sum of weighted δ-functions separated by a distance k_a in k-space.

$$F(k) = \sum_n F_n \delta(k - nk_a) \tag{3.4}$$

and vice versa

$$f(x) = \sum_n F_n e^{\mathrm{i}nk_a x} \tag{3.5}$$

The weights are a discrete set of values, the *Fourier coefficients*.

$$F_n = \frac{1}{2\pi} \int_{-\infty}^{\infty} f(x) e^{-\mathrm{i}nk_a x} dx, \tag{3.6}$$

One appeal of this approach is that the continuous function $f(x)$ can now be described by a set of numbers F_n. If $f(x)$ represents a physical quantity, F_n will usually vanish for large values of n. The extension of this formalism to three dimensions shall not be discussed here step by step. The major correspondence is given by the fact that now the vectors $\mathbf{k}_{1,2,3}(\mathbf{a}_{1,2,3})$ represent the *reciprocal lattice vectors* usually denoted as $\mathbf{a}^*_{1,2,3}$.

The reciprocal space is a concept that is mainly known from crystallography where it is used to describe crystal planes. The definition of a reciprocal lattice vector $\mathbf{a}^*_1$ is given by

$$\mathbf{a}^*_1 = \frac{\mathbf{a}_2 \times \mathbf{a}_3}{V_a} \tag{3.7}$$

(and cyclic rotation of the indices), with the volume of the real-space unit cell given by $V_a = (\mathbf{a}_1 \times \mathbf{a}_2) \cdot \mathbf{a}_3$. The relation between real- and reciprocal-space vectors is essentially $\mathbf{a}_i \mathbf{a}^*_j = \delta_{ij}$. As the scope of this work involves only the investigation of surfaces and adsorbates, the structural investigation is limited to the case of 2D lattices with $\mathbf{a}_1$ and $\mathbf{a}_2$ defining an unit cell of the area A_a. In this case, one obtains the simplified relations for the two in-plane vectors of the reciprocal lattice

$$\mathbf{a}^*_1 = \begin{pmatrix} a_{2y} \\ -a_{2x} \end{pmatrix} A_a^{-1} \tag{3.8}$$

$$\mathbf{a}^*_2 = \begin{pmatrix} -a_{1y} \\ a_{1x} \end{pmatrix} A_a^{-1}, \tag{3.9}$$

while the third reciprocal lattice vector $\mathbf{a}^*_3$ that is normal to the surface is degenerate with a length of zero. In this aperiodic situation, the length of the corresponding “lattice vector” $\mathbf{a}_3$ is infinite.

A direct observation of the reciprocal space is associated with the phenomena of interference and diffraction. The different descriptions of these effects all boil down to the important relation that constructive interference of diffracted

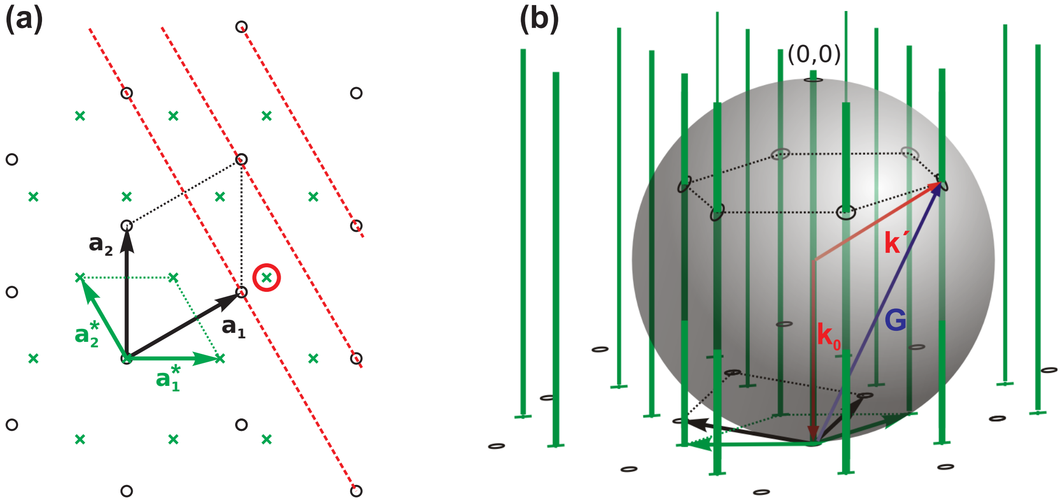

Figure 3.1: **(a)** 2D hexagonal real- and reciprocal-space lattice indicated by circles and crosses, respectively. The reciprocal lattice point that corresponds to the real-space (21) lines (dotted red) is the (21) point marked by a red circle. Note that there is a point symmetry, i.e., the $(\bar{2}\bar{1})$ point describes the same lattice lines. **(b)** Illustration of the Ewald-sphere construction for the 2D reciprocal-space lattice in (a). LEED spots of zero and first order emerge where the reciprocal lattice rods (perpendicular to the lattice plane) intersect the sphere with radius $|\mathbf{k}_0|$. At these points the relation $\mathbf{k}' - \mathbf{k}_0 = \mathbf{G}$ is fulfilled.

waves occurs only if the difference in the wave vectors of diffracted and incident wave $\Delta\mathbf{k} = \mathbf{k}' - \mathbf{k}_0$ is equal to an arbitrary reciprocal lattice vector[1]

$$\mathbf{G} = h\mathbf{a}_1^* + k\mathbf{a}_2^* + l\mathbf{a}_3^* = \mathbf{k}' - \mathbf{k}_0. \tag{3.10}$$

For the case of elastic scattering, i.e., without loss of energy, this requirement can be visualized nicely by means of an Ewald sphere construction. The sphere with radius $|\mathbf{k}_0|$ is centered on the origin of the incident wave vector $\mathbf{k}_0$ that terminates at a reciprocal lattice point. The wave vector of a diffracted wave $\mathbf{k}'$, in turn, terminates at a point where a lattice rod intersects the sphere. At these points the relation $\mathbf{k}' - \mathbf{k}_0 = \mathbf{G}$ is fulfilled. An example of a two dimensional reciprocal lattice and a respective Ewald sphere is given in Figure 3.1. The notation used for lattice lines is exemplified in Fig. 3.1(a). The construction in Fig. 3.1(b) allows the simplest possible interpretation of a LEED pattern, the so called *geometric* LEED theory.

Under the assumption that only the 2D surface lattice is probed in the diffraction experiment, the reciprocal lattice points are degenerate into lattice rods by the arguments given above. The incident wave vector $\mathbf{k}_0$ that connects the center of the sphere (radius $|\mathbf{k}_0|$) with the (00) rod of the reciprocal lattice is shown for normal incidence, a common situation in LEED experiments. The condition expressed by Eq. 3.10 is fulfilled wherever a reciprocal lattice rod

---

[1] A prove for this relation can, for example, be found in Ref. 61.

intersects the sphere. The respective positions, marked by ellipses, represent wave vectors with a constructive interference (in reflection geometry) leading to the first order LEED spots. If the backscattered electrons are displayed on a spherical screen, the LEED pattern is indeed a direct representation of the 2D reciprocal lattice shown in Fig. 3.1(a). The geometric LEED theory just outlined allows to explain the *positions* of spots only. In addition, a probe of perfect surface sensitivity is assumed, i.e., only a 2D lattice is probed. The next section is dedicated to a more sophisticated analysis of the diffraction of low-energy electrons. For a very detailed discussion of this issue, see Ref. 62.

3.1.2 Kinematic and dynamic LEED theory

Given an appropriate wavelength, in principle all kinds of quantum mechanical particles (photons, neutrons, ions, and electrons) make suitable probes for crystal structure analysis experiments. However, one prerequisite for the investigation of surface structures is a small mean free path (penetration depth) in the solid. Among possible candidates (neutrons, ions, electrons), a monochromatic beam of low-energy electrons can be produced most easily, making LEED the most widely used diffraction method for surface analysis. When approaching and entering the crystal, the electrons are subject to a strong Coulomb interaction resulting in a penetration depth that varies between 1 and 5 MLs [12]. There are at least two different ways to interpret a LEED pattern: The first one is a scattering approach, starting from the wave equation in the presence of a potential $\varphi(\mathbf{r})$.

$$\left[\nabla^2 + 4\pi^2 k_0^2 + \mu\varphi(\mathbf{r})\right] \Psi = 0 \tag{3.11}$$

Here, μ specifies the strength of the interaction and k_0 the wave number of the incident wave. The limit of a very weak interaction and thus a diffracted intensity that is small compared to the incident intensity ("Born approximation") is assumed. At a distance of observation large in comparison with the size of the scattering region, one finally obtains a scattering amplitude

$$f(\mathbf{q}) = \frac{\mu}{4\pi} \int \varphi(\mathbf{r}) e^{-2\pi \mathrm{i} \mathbf{q}\mathbf{r}} \mathrm{d}\mathbf{r} \tag{3.12}$$

in the direction of the point of observation $\mathbf{q} = \mathbf{k} - \mathbf{k_0}$. In case of constructive interference, i.e., for a reciprocal lattice vector $\mathbf{G}$, one obtains

$$f_{\mathbf{G}} \propto \int \varphi(\mathbf{r}) e^{-\mathrm{i}\mathbf{G}\mathbf{r}} \mathrm{d}\mathbf{r}. \tag{3.13}$$

Despite the fact that the differential scattering cross-section is proportional to $|f(\mathbf{q})|^2$, the intensity distribution can be understood as the Fourier transform of the scattering potential $\varphi(\mathbf{r})$.

The second approach originates from wave optics and starts with Huygens' principle of a generation of secondary waves that mimic the original wave front. In the limit of a detector far from the source of radiation at a distance z ("Fraunhofer diffraction"), the amplitude $\Psi(x_d, y_d)$ recorded in the detector plane is related to the transmission function $q(x_s, y_s)$ by

$$\Psi(x_d, y_d) \propto \iint q(x_s, y_s) exp\left\{-\frac{ik}{z}(x_s x_d + y_s y_d)\right\} dx_s dy_s. \tag{3.14}$$

Both descriptions are essentially equal in their mathematical structure, as both employ Fourier transforms. Unfortunately, the applicability to the case of LEED is limited: While a significant advantage of LEED is the electrons' small penetration depth due to the strong Coulomb forces, it also constitutes a major drawback as, consequently, Borns approximation is not valid and single scattering represents no accurate description of the LEED pattern. Only the so called "dynamic" LEED theory can fully account for multiple scattering events (and inelastic scattering not discussed here) by extensive numerical simulation.

The equivalent of the Born approximation in scattering theory is the assumption of a single diffraction plane in the Fraunhofer picture. The scheme of diffraction planes is better in providing an *intuitive* model of the scattering process in layered systems. When assuming a double-scattering process where electrons are diffracted first by the substrate and subsequently by the adsorbate, the resulting pattern is (again in a somewhat simplified picture) a convolution of both single-scattering diffraction patterns. This fact is of importance for the particular case of an adlayer with a thickness of one atom and an unit cell large compared to the unit cell of the (inorganic) substrate

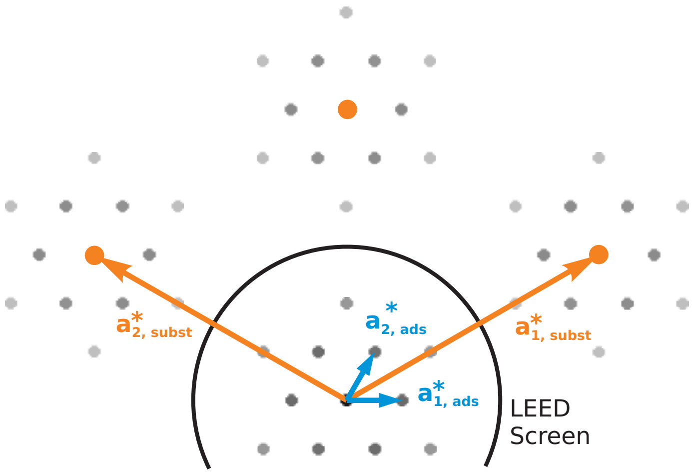

Figure 3.2: Suggestive illustration of the role of multiscattering in the formation of a LEED pattern of an organic adlayer. First order beams scattered by the substrate (orange) are scattered again at the organic layer leading to a convolution of spots from both lattices. The double-scattering adsorbate spots of high intensity are consequently located close to the substrate spots and hence outside the LEED screen.

surface. As the reciprocal substrate lattice is much wider than the reciprocal adsorbate lattice, the adsorbate diffraction patterns centered on the reciprocal (10), (01) ect. substrate lattice points barely overlap (Fig. 3.2). Under these conditions, the influence of multiscattering effects on a LEED pattern taken at low energy is consequently smaller, and the validity of the kinematic LEED theory is better than one would assume at first. In such a convolution scheme, quite descriptive, the intensity of a spot decreases with increasing number of scattering events necessary to produce the spot. Therefore, third order scattering can readily be excluded in most cases. If an observed spot cannot be associated with a double-scattering spot of high intensity, its intensity can be explained by kinematic theory alone. The software LEEDSim used for the evaluation of LEED patterns in this work is able to simulate geometric, kinematic and (geometric) double-scattering LEED patterns. A nice example for a prominent double-scattering mechanism without any adsorbate is given by the LEED pattern of a clean, reconstructed Au(111) surface. The side-spots in Fig. 2.9(a) are created by electrons scatterred at the bulk as well as at the slightly distorted surface layer.

3.1.3 Further applications of the Fourier transform

For direct imaging methods like STM, scanning force microscopy (SFM), and other techniques, the reciprocal space information obtained by calculating the Fourier transform allows to obtain precise information on the periodicities (the lattices) involved. Here, the Fast Fourier Transform (FFT) method is used. For STM images, the real-space pattern is a constant-conductivity map mixing electronic and topographical information. For a periodic surface, the spot positions in a LEED pattern and in the FFT of a STM image are similar, as both represent the reciprocal space and thus the reciprocal lattice as expressed by the analogy between Eq. 3.1 on the one hand and Eqs. 3.11 and 3.12 on the other hand. As the (local) conductance path *through* an organic heterolayer system is mainly coupled to overlapping π-systems, the image holds information about all participating layers (Section 2.2). In such a case, a FFT is the only proper way to identify and separate the contrast.

A third application of the Fourier transform is to calculate the FFT of potential energy maps. The maps themselves are calculated according to Chapter 4 by moving a single adsorbate molecule above a periodic surface. Here, the real-space pattern has the periodicity of the substrate lattice and hence the FFT spot positions equal LEED and FFT of a STM image of the respective substrate. The interpretation of the spot intensities is straightforward for potential energy maps: The intensity of the spot belonging to a reciprocal lattice vector $\mathbf{G}$, equals the amplitude of the respective potential energy plane wave in the Fourier expansion (Eq. 3.5). It is, in other words, a measure for the energetic gain of a growth along the respective lattice line in a point-on-line (POL) or line-on-line (LOL) fashion. This will be discussed in detail in Chapter 4.

3.2 Computational chemistry

For this work, dealing with thin layers of organic molecules adsorbed on metal surfaces, two aspects of computational chemistry are of great importance: Firstly, the correct description of single molecules, i.e., a method to calculate the atomic structure of and the electron distribution in a single molecule, and secondly a method to calculate the potential energy (PE) between individual molecules as well as between molecules and substrate.

3.2.1 Calculating molecular properties

The basic principle of a chemical interaction is the merger of the electron wave functions belonging to individual atoms in close proximity. This redistribution of electron density is accompanied by a lowering of the system's potential energy which stabilizes the created molecule. As the many-electron wavefunction involved is hard to comprehend and hard to deal with mathematically, representations based on single electron wave functions are used. The *valence bond* theory fits best to an intuitive picture of a covalent bond. One main idea of this theory is to explain a covalent σ bond as an overlap between *hybrid orbitals* constructed from regular atomic orbitals. The hybrid orbitals have a distinct angular localization and point in the direction of the bond. Fig. 3.3 shows the σ bonds in a benzene molecule that enclose angles of 120°. For π bonds, resulting from an overlap between (aligned) p orbitals of carbon atoms, the picture of a localization between two binding partners, i.e., atoms is not necessarily valid. In aromatic (= cyclic or polycyclic) compounds, which contain at least one benzene ring, the π electrons are delocalized over the whole ring (Fig. 3.3).

All molecular species investigated here are substituted or unsubstituted polycyclic hydrocarbons and, hence, contain an extended π system. The intramolecular bonding is dominated by the carbon atoms and their specific electronic properties. With a total of six electrons, carbon atoms are tetravalent. In organic substances, carbon occurs in sp^2 hybridization, i.e., three electrons

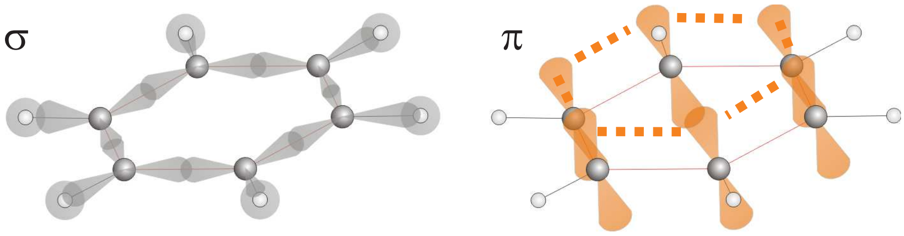

Figure 3.3: Illustration of the σ and π bonds in a benzene molecule.

participate in covalent σ bonds, whereas the remaining electron contributes to a π bond. In aromatic systems, the optimal geometry is an arrangement of all C atoms in a single plane, allowing an optimal overlap between neighboring p orbitals. An illustration of the σ and π bonds in benzene is shown in Fig. 3.3.

For the calculation of molecular properties by numerical algorithms, i.e., *computational chemistry*, a different representation of the many-electron wave function is commonly used. In a specific case of the *molecular orbital* theory, the "Hartree-Fock self-consistent field method", a (Coulomb) potential well, created by the nuclei and the electron density, is filled by a set of orthonormalized single-electron wave functions. Consequently, most "electrons" are delocalized over the whole molecule. As wave functions themselves are no observables, neither the valence bond nor the molecular orbital wave functions are superior in terms of physical meaning. In the Hartree-Fock method, the wave functions are optimized iteratively with the aim of reducing the total potential energy according to the variational principle. Unfortunately, the computational effort for each iteration scales with n^4 with n being the number of orbitals. For medium or large sized molecules and in case of limited computational power, severe simplifications have to be introduced.

The so-called *semiempirical* methods replace very time and memory consuming calculations within the Hartree-Fock method by a set of parameters which are optimized using experimental results. This is done in advanced algorithms by using a certain training set of molecules with well known properties and optimizing the parameter set until the calculated results come close to the measured values. As a rule of thumb, the accuracy of a semiempirical calculation of an arbitrary molecule is therefore best if the molecule is similar to a molecule of the training set. There is an evolution among the semiempirical methods, where the algorithms differ in the kind of Hartree-Fock calculations which are replaced. The way up to the PM3 method used in this work is therefore illustrated best by the names of the "precursors":

1. CNDO (complete neglect of differential overlap)
2. INDO (intermediate neglect of differential overlap)
3. NDDO (neglect of diatomic differential overlap)

There are even variances in each of these methods. PM3 (Parameterized Model 3) [63] is a member of the NDDO family and widely used in literature.

Compared to the calculation of the properties of covalently bound molecules, the quantitative analysis of the intermolecular forces and the forces between a molecule and an extended solid are much harder to tackle. This is, in particular, due to the quantum mechanical nature of the van der Waals forces responsible for the non-bonded interaction. The two contributions to this interaction are called *exchange* and *correlation* between electrons and refer to a repulsion from the Pauli exclusion principle and to an induced dipole - induced dipole attraction (London force), respectively. While the exchange interaction is inherent to the Hartree-Fock method and leads to the demand for orthonormalized wave functions, the correlation between electron wave functions is *not* included. Two ways to correct for this deficiency are either the *configuration interaction* (CI) method which includes excited states in the calculation, or the *Møller-Plesset* (MPx) method which includes x-th order perturbation theory. Both methods scale with at least n^5 and are consequently no option for the study of larger systems or many molecules. The use of *density functional theory* (DFT) is no option for the same reason. In DFT, the energy of a system is calculated as a functional of the electron density distribution. As standard DFT includes neither exchange nor correlation, both have to be introduced by an exchange-correlation functional. Most state-of-the-art functionals are of no use here: The corrections made to the energy values depend either on the local charge density only (local density approximation, LDA), or include also the derivative of the local charge density (generalized gradient approximation, GGA). Both methods are unable to account for the explicitly non-local correlation part of the van der Waals interaction where electron densities at *different* positions are relevant.

The calculations of van der Waals potentials conducted in this work are thus based on atomic force fields which are parameterized empirically. The fundamental assumption behind this approach is that the complex non-local interaction can be broken down into pairwise-additive interactions between atoms. This method is part of the framework of *molecular mechanics* which includes a large number of published parameter sets, each with a large number of parameters. The focus of molecular mechanics is, however, mainly on the modeling of covalent bonds and the description of non-bonding parameters takes only a small fraction of the efforts in such publications.

Unfortunately, the stigma of being outdated which is generally attributed to molecular mechanics thus also sticks on the modeling of van der Waals interaction via empirical methods. While this criticism might be justified at least partially for the calculation of molecular properties via empirical methods, it is certainly inappropriate for the treatment of non-bonding interaction since there are no comparable methods available. Far from it, the corrections used to include *long range* dispersion into DFT are practically identical to the atomic force-field method [64, 65]. The still persisting problems with the calculation of molecule-substrate interaction energies by DFT can, for example, be seen by an attempt to predict the adsorption geometry of PTCDA on Ag(111) (Ref. 66 incl. comment and reply). First-principles calculations are still far from being applicable to systems of medium size. Recently, results for small benzene-like molecules and for the short interaction distance between molecule and metal substrate were published [67].

3.2.2 The atomic force-field method

In the force-field approach, the van der Waals potential energy between two molecules (or a molecule and an extended solid) is expressed as a sum over all pairs of atoms (u,v) which are *not* located on one and the same molecule.

$$V_{mol-mol}^{vdW} = \sum_{u=1}^{m} \sum_{v=1}^{n} V_{aa}(\mathbf{r}_u, \mathbf{r}_v) \tag{3.15}$$

The atom-atom potential V_{aa} is only a function of the interatomic distance and parameterized by the types of both atoms. As the electron configuration in a covalently bound atom depends not only on the atom type, but also on its binding partners, there are usually more atom types than elements in a parameter set.

The force fields used in this work are parameterized either especially for the interaction between hydrocarbons (OPLS [68, 69]), or, more general, for the non-bonded interaction between any two types of atoms in the periodic table (universal force field (UFF) [70]). For aromatic molecules, it is necessary to consider the delocalized π electron system: While the dipole fluctuations modeled by the force field are usually located at the individual atoms, here also dipole fluctuations in the extended aromatic system of the molecule contribute to the overall attraction. The UFF parameters provide rather a measure for the potential between individual atoms (or cations in case of a metal), while the OPLS parameters, due to their different “training set”, should account for the van der Waals force between aromatic molecules, including the contribution of the delocalized electronic system.

In both force fields used in this work, the atom-atom potential is of Lennard-Jones type

$$V_{aa} = 4\epsilon \left\{ \left(\frac{\sigma}{r}\right)^{12} - \left(\frac{\sigma}{r}\right)^{6} \right\}. \tag{3.16}$$

The values for ϵ and σ are the force-field parameters which are usually averaged geometrically (ϵ) or arithmetically (σ) in case of an interaction between unequal atoms.

The molecule-molecule van der Waals potential $V_{mol-mol}^{vdW}$ is modeled by the OPLS force-field parameters, while the UFF parameters are used to model the van der Waals interaction with the metal. The latter interaction represents only a fraction of the entire molecule-substrate potential. There are additional contributions caused by an overlap (and redistribution) of free metal electrons and delocalized π electrons. This explains why the binding energy of a single molecule to the Au(111) surface V_{single} which results from the calculation is generally too small. Still, it is assumed that the van der Waals potential between the atoms in the molecule and the Ag or Au ions is a good estimate for the corrugation of the molecule-substrate potential, while the remaining attractive part can be assumed to provide merely a constant offset. This assumption should especially be valid in the absence of any heteroatoms as in the case of HBC and QT. The discrepancy between the calculated van der Waals potential V_{single} and experimental data for the total adsorption energy is significant. According to an extrapolation of existing thermal desorption spectroscopy (TDS) data on hydrocarbons [71, 72], the adsorption energy of HBC on Au(111) is in the range of $(-3.9 \pm 0.5)\,\mathrm{eV}$, while the pure van der Waals calculation yields only -1.4 eV.

This limitation applies obviously to the molecule-metal interaction only as the force-field method is able to reproduce the adsorption energy per molecule in a HBC *multilayer* system[2] ($(-2.2 \pm 0.1)\,\mathrm{eV}$ from TDS data [73]) with accuracy of about 10 percent.

A second type of interaction with an important influence on the intermolecular potential is the Coulomb interaction $V^{Coulomb}_{mol-mol}$. The non-uniform charge distributions in chemical compounds creates electrostatic dipole or quadrupole moments. The interaction between these *permanent* moments contributes to the total potential in the same fashion as the fluctuating moments of the London attraction do. The Coulomb forces are modeled by pairwise additive atom-atom potentials as well. The respective charges result from a projection of the total charge density on each atom. The calculation of these *partial charges* is part of the PM3 calculation conducted to optimize the molecular geometry. The electrostatic part of $V_{mol-mol}$ is, in equivalence to Eq. 3.15, a sum over all atom-atom pairs in a standard Coulomb term

$$V^{Coulomb}_{mol-mol} = \frac{1}{4\pi\epsilon} \sum_{u=1}^{m} \sum_{v=1}^{n} \frac{q_u q_v}{|\mathbf{r}_u - \mathbf{r}_v|} \tag{3.17}$$

The total molecule-molecule interaction is then calculated as

$$V_{mol-mol} = V^{vdW}_{mol-mol} + V^{Coulomb}_{mol-mol}.$$

In the following part the practical aspects of the force-field calculation will be addressed.

3.2.3 Potential energy calculations in extended systems

Here, a method is outlined that allows to calculate the potential energy V_{total} per molecule of a whole adsorbed layer of organic molecules. The potential V_{total} is split up into the (pairwise calculated) intermolecular interaction in the film V_{intra}, and the molecule-substrate interaction V_{inter}.

$$V_{total} = V_{intra} + V_{inter}$$

---

[2] Here, the substrate has no influence and the respective energy solely stems from intermolecular interaction.

The potential V_{intra} (per molecule) in the whole layer is obtained by adding $V_{mol-mol}$ for all n molecules in the layer, each with its i next neighbors, while avoiding double counting and dividing by n:

$$V_{intra} = \frac{1}{2n} \sum_{s=1}^{n} \sum_{t=1}^{i} V_{mol-mol}(s,t) \tag{3.18}$$

The molecule-substrate potential (per molecule) is calculated in a similar fashion as the sum over all single molecule potentials:

$$V_{inter} = \frac{1}{n} \sum_{s=1}^{n} V_{single}(s) \tag{3.19}$$

Several simplifications have to be applied in order to perform the respective task within a reasonable amount of time with today's computational power. The molecular geometry is calculated by the PM3 method described above and remains unchanged during the potential energy calculations, i.e., the molecules are rigid as is the substrate. To speed up the calculation for a large number of molecules and even allow structural optimization, the potential energy values $V_{mol-mol}$ and V_{single} are pre-calculated and stored in a hash table called *Gridfile.* This implies a limitation for the substrate, as the pre-calculations of V_{single} are performed for one unit cell only and mapped onto the respective arbitrary positions in a periodic fashion. Long range substrate variations like unordered substrates or large surface reconstruction periodicities (e.g. Au(111)) hence cannot be treated with reasonable complexity. The respective calculations of the van der Waals and Coulomb potential have been performed using the software PowerGrid by S. C. B. Mannsfeld [16, 39, 74], which allows to compute a large variety of different scenarios due to its freely programmable script language interface.

4 Epitaxy in terms of potential energy

In this chapter the concepts of epitaxial growth are introduced. In contrast to previous discussions of this topic in literature which mainly focus on a geometric approach based on the epitaxial matrix $\mathbf{C}$*, here the entire argumentation is based on the interface potential energy which is the driving force behind the occurrence of epitaxy. The discussion is naturally limited to the case of crystalline overlayers (2D lattices) of molecules. Whether a molecular species forms such a lattice depends on several factors that are* not *discussed in this chapter. The mobility of the molecules on the surface, the coverage, and the intermolecular forces are amongst the factors that influence the lattice formation. While an attractive molecule-molecule interaction promotes the ordering process, this may be counterbalanced by the general tendency to increase the entropy in the system. The role of entropy will be discussed briefly in Section 5.4.*

Induced by short range forces between substrate and adsorbate, a *single* adsorbate molecule or atom on a crystalline surface experiences a site depended potential $V_{single}(\mathbf{r})$ that naturally exhibits the periodicity of the surface lattice. The potential can consequently be represented as a sum over harmonic standing waves with multiples of the lattice periodicity in analogy to the Fourier series in Eq. 3.5. The coefficients i and j define the reciprocal lattice vectors $\mathbf{G}_{i,j}$ and $\phi_{\mathbf{G}}$ holds the phase information.[1]

$$V_{single}(\mathbf{r}) = \sum_{i,j} E_{i,j} e^{\mathrm{i}(\mathbf{G}_{i,j}\mathbf{r}+\phi_{\mathbf{G}})} = \sum_{\mathbf{G}} E_{\mathbf{G}} e^{\mathrm{i}(\mathbf{G}\mathbf{r}+\phi_{\mathbf{G}})} \tag{4.1}$$

For the discussion of epitaxy it is convinient to separate the site independent contribution $E_0 := E_{0,0}$ from the sum. E_0 represents the *incommensurate* energy, while the rest of Eq. 4.1 which depends on $\mathbf{r}$ will be denoted $V'_{single}(\mathbf{r})$:

$$\begin{aligned} V_{single}(\mathbf{r}) &= E_0 + V'_{single}(\mathbf{r}) \\ V'_{single}(\mathbf{r}) &= \sum_{\mathbf{G}\neq\mathbf{0}} E_{\mathbf{G}} e^{\mathrm{i}(\mathbf{G}\mathbf{r}+\phi_{\mathbf{G}})} \end{aligned} \tag{4.2}$$

---

[1] In the following, the notations $E_{i,j}$ and $E_{\mathbf{G}}$ have identical meanings as $\mathbf{G}$ is only an abbreviation for $i\mathbf{a}_1^* + j\mathbf{a}_2^*$.

If the adsorbate exists in a crystalline phase as well, the question of the epitaxial relation can be raised. Epitaxy means that there is a certain relation between substrate and adsorbate lattice. The description of this relation by a matrix $\mathbf{C}$ was proposed by Park and Madden [75]. The *epitaxial matrix* $\mathbf{C}$ yields the transformation between primitive substrate and adsorbate lattice vectors:

$$\begin{pmatrix}\mathbf{b}_1\\ \mathbf{b}_2\end{pmatrix} = \mathbf{C}\begin{pmatrix}\mathbf{a}_1\\ \mathbf{a}_2\end{pmatrix} \tag{4.3}$$

The energy of the whole adsorbate layer V_{inter} means, in principle, the sum over all adsorbed molecules with positions $\mathbf{r}$ in the layer or domain. To eliminate the dependency on the number of molecules n right from the beginning, V_{inter} is defined as the interface potential energy *per molecule* of a domain.

$$\begin{aligned} V_{inter} &= \frac{1}{n}\sum_{\mathbf{r}} V_{single}(\mathbf{r}) && (4.4)\\ V_{inter} &= E_0 + \frac{1}{n}\sum_{\mathbf{G}\neq\mathbf{0}}\sum_{\mathbf{r}} E_{\mathbf{G}} e^{\mathrm{i}(\mathbf{G}\mathbf{r}+\phi_{\mathbf{G}})} = E_0 + V'_{inter} && (4.5)\\ V'_{inter} &= \frac{1}{n}\sum_{\mathbf{G}\neq\mathbf{0}}\sum_{\mathbf{r}} E_{\mathbf{G}} e^{\mathrm{i}(\mathbf{G}\mathbf{r}+\phi_{\mathbf{G}})} && (4.6)\end{aligned}$$

The definition of V'_{inter} is similar to that of $V'_{single}(\mathbf{r})$. The driving force behind the epitaxial growth is the minimization of the interface potential V_{inter}. As E_0 is a constant, it is sufficient to examine V'_{inter} for this purpose.

With a periodic, position dependent potential energy of a *single* adsorbate, the question of epitaxy is basically a question of coherence between the substrate and adsorbate lattice. If the adsorbate lattice is coherent with at least only *one* of the addends in Eq. 4.2, i.e., one of the standing "potential energy plane waves", each adsorbed molecule can occupy a position in one of the minima of this standing wave. A coherence between substrate and adsorbate lattice is characterized by a coincidence of an arbitrary reciprocal substrate lattice vector and an arbitrary reciprocal adsorbate lattice vector $\mathbf{G}_{sub} = \mathbf{G}_{ads} = \mathbf{G}_c$, and consequently

$$e^{\mathrm{i}\mathbf{G}_c\mathbf{r}} = 1 \;\;\forall\, \mathbf{r} \longrightarrow V'_{inter} = \frac{1}{n}\sum_{\mathbf{r}} E_{\mathbf{G}_c} e^{\mathrm{i}\phi_{\mathbf{G}_c}} = E_{\mathbf{G}_c} e^{\mathrm{i}\phi_{\mathbf{G}_c}} \tag{4.7}$$

This analysis is still too short-handed as a coincidence of $\mathbf{G}_{sub}$ and $\mathbf{G}_{ads}$ implies also a coincidence of all multiples of the respective reciprocal lattice vectors.

$$m\mathbf{G}_{sub} = m\mathbf{G}_{ads} = m\mathbf{G}_c \;\;\forall\, m \in \mathbb{N} \tag{4.8}$$

Consequently, the minimum of V'_{inter} depends on the amplitude $E_{\mathbf{G}}$ as well as the phase $\phi_{\mathbf{G}}$ of each plane wave which contributes.

$$V'_{inter} = \sum_{\mathbf{G}_c} E_{\mathbf{G}} e^{\mathrm{i}\phi_{\mathbf{G}}} \tag{4.9}$$

This equation constitutes the most general description of the energetic gain related to epitaxial growth. It thus represents the basis for the discussion of the different types of epitaxy that can be classified hierarchically into a "grammar of epitaxy" [39, 76]. The term "energetic gain" for V'_{inter} is justified by Eq. 4.5. If there is no coincidence between any vectors $\mathbf{G}_{sub}$ and $\mathbf{G}_{ads}$, the interface potential equals the incommensurate energy $V_{inter} = E_0$ as $V'_{inter} = 0$ in an infinitely extended domain (no proof given here).

The discussion of epitaxial relations can most favorably be conducted simultaneously in the real and reciprocal space as shown in Figure 4.1. In the reciprocal space, much better than in real space, the coherences are visible as a coincidence of reciprocal lattice points. As the amplitude values $E_{i,j}$ should be considered as well, the discussion of real and reciprocal space is not done in a merely geometric fashion but by using potential energy maps. While the (real-space) maps of $V_{single}(\mathbf{r})$ are created by moving a single adsorbate atom/molecule over the surface and calculating its potential energy (PE) according to Section 3.2.3, the reciprocal space can be obtained as the Fourier transform of the potential, i.e., the FFT of the potential map.

The question where the respective types of epitaxy should be observable experimentally emerges naturally from the line of argumentation given here. The first, and rather trivial, type of epitaxy is homo-epitaxy, where the lattices of substrate and adsorbate are identical. This case, which is not shown in Fig. 4.1, is characterized by a coincidence of *all* reciprocal lattice points of adsorbate and substrate and consequently a coherence of all standing waves. Naturally, this represents the highest energetic gain achievable as all adsorbates are located in the deepest minima of $V_{single}(\mathbf{r})$. A similar gain in energy results from the commensurate epitaxy, where all adsorbates occupy *identical* substrate lattice sites. In this case of epitaxy, for every (primitive or nonprimitive) substrate lattice line (each equal to a potential energy plane wave) there is a coherent adsorbate lattice line. Thus, the adsorbate realizes the same energetic gain in case of commensurate epitaxy as in the case of homoepitaxy discussed above.[2] An example for commensurate epitaxy is shown in Fig. 4.1(a). A commensurate growth is given by an epitaxial matrix $\mathbf{C}$ containing integers only. The potential map in Fig. 4.1(a) is that of an atom adsorbed on a single element crystal's (111) surface, where each potential maximum equals the position of a substrate atom. As can be seen from the Fourier transform, such a potential is almost harmonic, i.e., the expansion in Eq. 4.2 is dominated by the first order terms $E_{1,0}$ and $E_{0,1}$, and consequently the major part of the intensity in the FFT belongs to the first order spots.

The same potential map is used in Fig. 4.1(b) to illustrate the point-on-line (POL) type of epitaxy. The term POL epitaxy was first introduced by

---

[2] This is obviously only valid if the adsorbed atoms/molecules are of identical chemical nature in both cases.

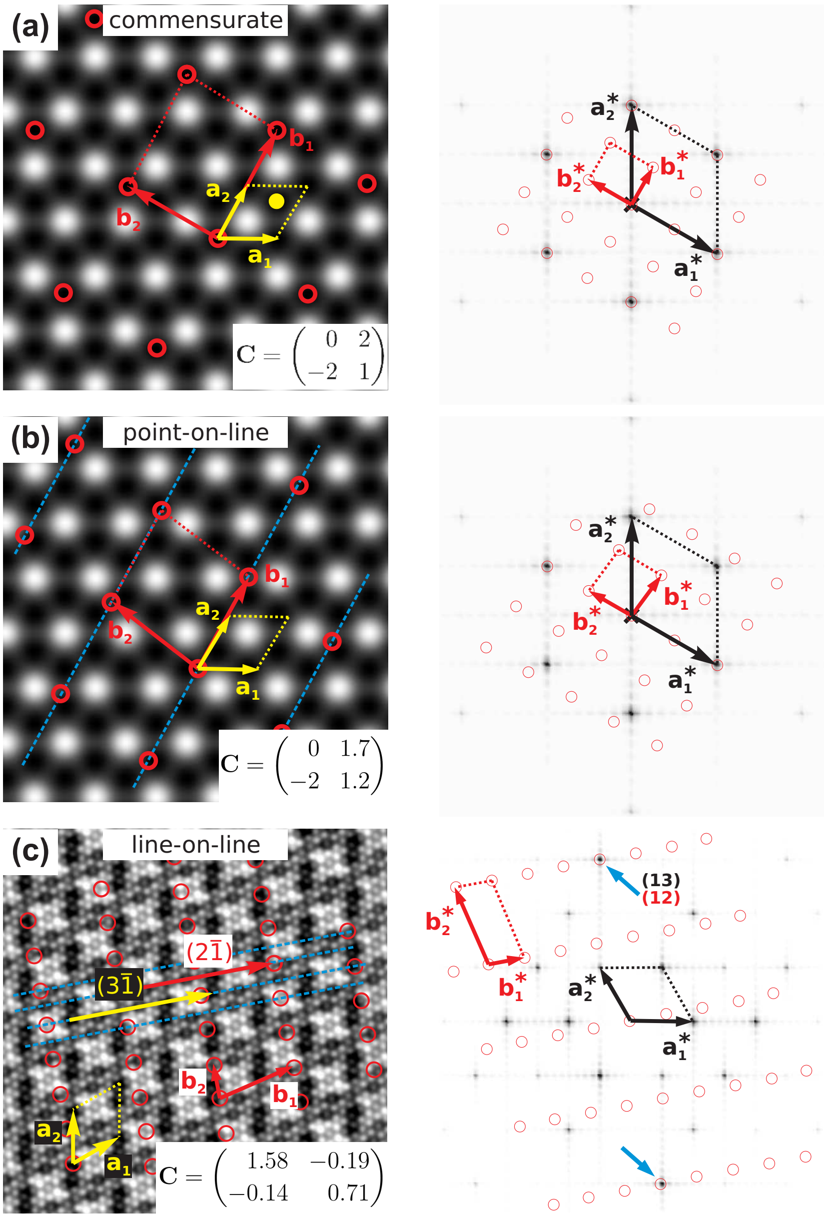

Figure 4.1: **(a)** and **(b)** Potential energy (PE) map for a single atom moved over an Au(111) surface. The Au(111) unit cell is shown in yellow. Two non-equivalent PE minima exist, corresponding to the hollow sites between the Au atoms. An exemplary commensurate lattice with adsorption sites at positions of minimal PE is indicated in (a), while a POL coincident lattice with adsorption along a primitive Au(111) lattice line of minimal PE (blue dashed) is shown in (b). The epitaxial matrix **C** defines the relation between Au and adsorbate lattice. The right hand side of (a) and (b) shows the FFT of the PE map with indicated reciprocal lattices. The commensurate lattice in (a) means a coincidence of *all* (reciprocal) adsorbate lattice points and first-order substrate lattice points. In case of a POL coincidence only *one* first-order spot coincides. **(c)** PE map for a QT molecule scanned over a HBC layer (unit cell in yellow). Red circles mark a LOL coincident lattice characterized by a coincidence between $(31)_{HBC}$ and $(21)_{QT}$ lattice lines (blue dashed). In the FFT of the PE map, the respective (13) and (12) lattice points coincide (blue arrow).

Hoshino et al. to describe the growth of PTCDA on HOPG [77]. The same growth principle has, however, already been observed before for the adsorption of gaseous particles and named "uniaxial incommensurate" (UIC) growth [78]. Here, the requirements for the adsorbate lattice are not as strict as in the commensurate case, i.e., the POL type requires less adjustment of the adsorbate lattice in order to be realized. POL epitaxy is characterized by the coincidence of only *one* of the first order reciprocal lattice vectors of the substrate with a reciprocal lattice vector of the adsorbate, and hence a coherence in one direction only. As a result, only one first order coefficient $E_{1,0}$ contributes to the energetic gain. In the case of a hexagonal, almost harmonic interface potential (Fig. 4.1(b)), this means an energetic gain of $2/3E_{comm}$ only, as two of the three first order plane waves do not contribute.[3] The question whether there are coherences of higher-order spots (besides $E_{2,0}$, $E_{3,0}$, ect.) is not discussed here in detail. The result would be a so-called commensurate supercell, but as was stated before, there is almost no intensity in the higher-order spots and consequently coherence in higher order does not lead to a significant gain in energy for the substrate discussed. If $V_{single}(\mathbf{r})$ is *not* harmonic or close to harmonic, the higher order terms $E_{2,0}$, $E_{3,0}$, ect. in Eq. 4.9 contribute significantly to the value for V'_{inter}. This aspect will be discussed in Section 8.2. POL epitaxy is characterized by a *column* of integers in the epitaxial matrix **C**. On substrates with a hexagonal symmetry, POL matrices may also feature integer sums or differences in each row instead of an integer column.

The last type of epitaxy discussed here is characterized by coherence between higher-order lattice lines of substrate and adsorbate, i.e., line-on-line (LOL) epitaxy. Although this cannot mean a significant energetic gain for the single atom substrates discussed so far, it has been observed for the specific system of xenon adsorbed on different metal surfaces [79]. Here, the focus shall be on epitaxial systems where one organic species is grown onto another [39, 42]. Such a substrate-adsorbate system leads to a much more complex PE map, as depicted in Fig. 4.1(c) for a QT molecule on a HBC layer. Now, the intensity in higher-order spots in the FFT is significant, which is obviously the case for the (13) and also the (20) spot in Fig. 4.1(c). Here, there is no basic rule defining how large the gain in potential energy of a certain LOL structure is, as this is related to the respective value of $E_{i,j}$. The present case shows, however, that the intensity in the higher-order spots can be of the same order of magnitude than the intensity in the first order spots. It is also visible from the FFT in Fig. 4.1(c) that the intensities are not distributed equally to all spots that are equivalent in terms of rotational symmetry of the substrate anymore. This is caused by the fact that the adsorbate molecule is not of the

---

[3] The factor is *not* 1/3 as one would assume at first, due to the phase ϕ of the three first order plane waves. The minima in Fig. 4.1(a) and (b) are *not* the minima of the first order pane waves.

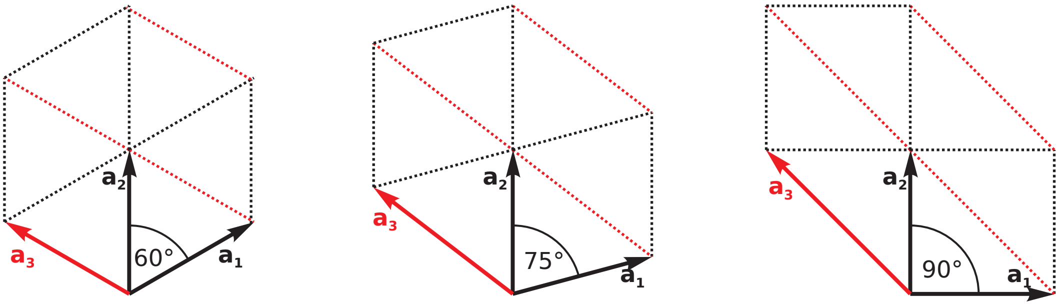

Figure 4.2: In the transition from a hexagonal to a square lattice, the vector $\mathbf{a}_3$ turns from a primitive into a non-primitive lattice vector. Growth on the respective lattice lines (red) is thus a mix of POL and LOL epitaxy for the transitional lattices.

same symmetry as the substrate lattice, but has a twofold symmetry only. In the case of LOL growth, the higher order terms in Eq. 4.9 play only a minor role as the respective amplitudes $E_{mi,mj}$ decrease rapidly with increasing m (Section 8.2).

As a matter of fact, the knowledge of all LOL coefficients, i.e., coincidence of (ij) substrate lattice lines with (kl) adsorbate lattice lines alone, is *not* sufficient to derive the adsorbate lattice from a given substrate lattice. This is immediately evident as the density of the molecules along the coincident lattice line is not determined by the LOL epitaxy.

One should note a special property of the hexagonal substrate lattice: The description of the respective potential $V_{single}(\mathbf{r})$ by the two primitive substrate lattice vectors $\mathbf{a}_1^*$ and $\mathbf{a}_2^*$ as well as the coefficients $E_{i,j}$

$$V_{single}(\mathbf{r}) = \sum_{i,j} E_{i,j} e^{\mathrm{i}[(i\mathbf{a}_1^* + j\mathbf{a}_2^*)\mathbf{r} + \phi_{i,j}]}, \qquad (4.10)$$

leads to an ambiguity in the *order* of these coefficients. Due to the six-fold symmetry, all “first-order” coefficients are

$$E_{1,0},\ E_{-1,0},\ E_{0,1},\ E_{0,-1},\ E_{1,1} \text{ and } E_{-1,-1},$$

while all “(1,1)” coefficients are

$$E_{1,-1},\ E_{-1,1},\ E_{2,1},\ E_{1,2},\ E_{-2,-1} \text{ and } E_{-1,-2}.$$

Although a notation including three indices (i, j, k) would solve this issue, the result would be a redundancy where only a few triples (i, j, k) would be allowed. Such an option is therefore less favorable.

It is not always possible to distinguish between POL and LOL epitaxy. While on lattices of high symmetry, like hexagonal and square lattices, the assignment is unambiguous there are also lattices which do not allow a meaningful identification of the order of reciprocal lattice points. This can be illustrated by a continuous transition from a hexagonal to a square lattice, i.e., an increase of the unit cell angle α from 60° to 90° (Fig. 4.2). In this transition, the vector $\mathbf{a}_3$ turns from a primitive into a non-primitive lattice vector. Consequently, it is not possible to label the growth along $\mathbf{a}_3$ either POL or LOL for a set of lattices in between both cases. This consideration bears relevance for epitaxy on organic layers which are not restricted to 2D unit cells of high symmetry.

Concluding, the attempt to minimize the interface potential energy V_{inter} leads to a coherence between one (LOL and POL epitaxy), two (commensurate supercell) or all (commensurate epitaxy) lattice lines of substrate and adsorbate (incl. higher orders). Which of these epitaxial growth modes is actually realized in a specific system depends on the interface potential $V_{single}(\mathbf{r})$ and also on the potential *in* the adsorbate layer V_{intra}. The final adsorbate structure will be characterized by a minimum in $V_{total} = V_{inter} + V_{intra}$, but not necessarily by a minimum in one of the two addends.

A short notice is necessary to clarify the term *potential energy gain* or *energetic gain*. It is commonly used to describe the fact that a system reached a state of lower potential energy, e.g., a potential energy minimum. Such a process is, however, accompanied by a *loss* of potential energy and not by a *gain*. Nevertheless, both phrases will be used synonymously and in the above mentioned sense to avoid confusions.

5 Interaction of QT and HBC at Sub-ML and ML Coverage

As mentioned in the introduction, there is large interest in understanding and tuning the structure of organic thin films. One important aspect of the growth of ordered, crystalline films is the influence of the first layer. The delicate balance between intermolecular interaction and molecule-substrate interaction often results in a growth mode that differs significantly from the bulk phase of the respective organic crystal. The structure of the first layer, in turn, has an impact on subsequently grown layers of the same or of a different organic compound. In this chapter, the ordering principles in sub-ML and ML films of the hydrocarbons QT and HBC are analyzed by LEED and STM. A quantitative model for the intermolecular interaction in HBC films is introduced and its implications are discussed. Insight is gained in direct and substrate-induced effects that govern this interaction. The mentioned impact of the structure of the first ML on subsequently grown layers gives additional relevance to this study. In Chapter 7 an organic-organic heterosystem is described that employs a ML of HBC on Au(111) as a substrate for the subsequent growth of a PTCDA layer.

5.1 Experimental results

While previous publications found a ML growth of HBC on Au(111) describable by a set of *fixed* lattice parameters [35, 40, 80], the growth mechanism is reinvestigated here focusing especially on sub-ML coverage. The complementary investigation of QT sub-MLs allows a comparison of two large hydrocarbons exhibiting different shapes and different electronic properties. Likewise, the system HBC on Ag(111) is studied to identify possible substrate induced effects. For sake of clarity, this section will start with a rather short report of QT on Au(111) results, while the case of HBC is discussed in more detail later on. The investigation of sub-MLs of QT and HBC presented here is mainly performed by means of LEED, particularly due to the failure of attempts to obtain STM images of such films. Here, the problems arise mainly from the high mobility of the molecules at room temperature. There is a delay time of $>$ 15 min between subsequent LEED patterns in all LEED series in this chapter.

Both sample preparation and characterization were completely conducted under UHV conditions at room temperature. Thin QT and HBC films of variable thickness up to 1 ML were prepared by OMBE at an evaporation temperature of $\gtrsim 350\,^{\circ}\mathrm{C}$ and $\gtrsim 430\,^{\circ}\mathrm{C}$ (Ref. 33), respectively. The deposition rate was as low as 0.06 ML/min. The molecular flux was initially monitored with a quartz crystal microbalance (QCM) and subsequently refined from LEED and STM data of *closed* MLs. Alternatively, evaporation rate data acquired by Roman Forker has been used. His approach is based on the observation of distinct changes in the differential reflectance spectrum (DRS) of thin films as soon as a second ML starts to grow [41, 56].

QT on Au(111)

Figure 5.1 shows a series of LEED patterns taken at a QT coverage between 0.45 ML and 1.02 ML on Au(111). With increasing coverage, a previously diffuse halo (Fig. 5.1(a)) turns into a halo with sharper borders (b), and into a diffuse ring (c) at approximately 0.9 ML. Such diffraction patterns are characteristic for an isotropic distribution of scatterers. The halos indicate that there is no preferential separation s between individual QT molecules on the samples in Fig. 5.1(a) and (b). From the size of the halo a smallest separation can be determined as $s_{min} = (12 \pm 1)$ Å in case (b). The ring in pattern (c) is a sign of a distinct separation $s = (12 \pm 1)$ Å between neighboring QT molecules, while still no preferential domain orientation δ exists. Finally, at ML coverage, a complex pattern of sharp spots is found that resembles the patterns previously observed for QT MLs on Au(111) [55] (Fig. 5.1). The pattern can be understood by considering the six-fold substrate symmetry and an off-axis domain orientation of QT resulting in the occurrence of mirror domains.

To illustrate the growth of QT at ML coverage, Figures 5.1 (e) and (f) show a structural model as well as a STM image. The unit cell parameters extracted from Fig. 5.1(d) are larger by two percent if compared to the results from Ref. 55. While this deviation is still within the experimental error interval, it might still indicate that there is *no* single set of lattice constants a_1 and a_2 describing the ordered phase of QT on Au(111). The diffuse patterns in Figs. 5.1(a)-(c) on the other hand prove that molecular islands with a distinct orientation do not form at a coverage below 0.9 ML. Thus, one has to conclude that the intermolecular attraction due to van der Waals forces is obviously inhibited.

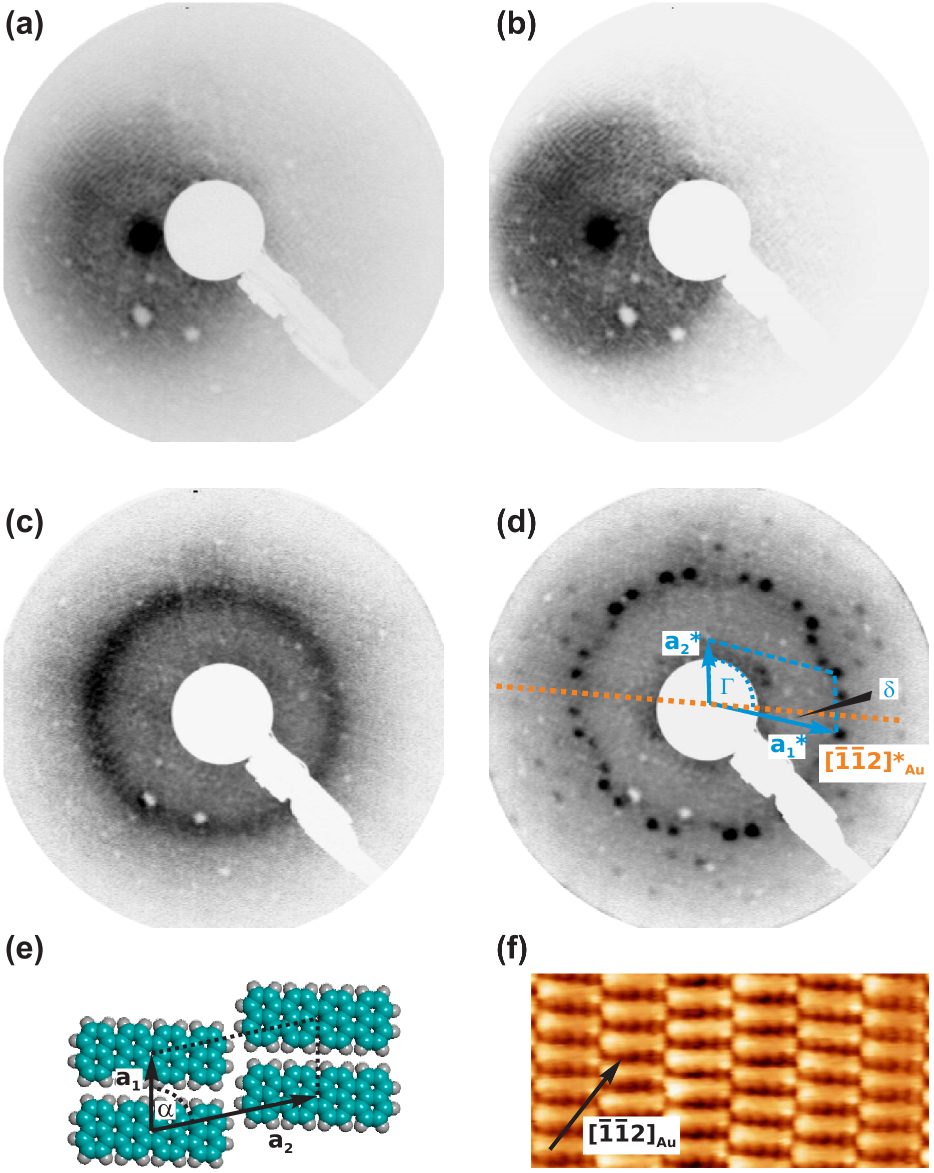

Figure 5.1: LEED patterns for varying QT coverage on Au(111). All images have been recorded at $E_0 = 10.4\,\mathrm{eV}$. **(a)** $(0.45 \pm 0.05)\,\mathrm{ML}$ of QT, off-center, extracted intermolecular distance above $(12 \pm 2)\,\text{Å}$. **(b)** $(0.68 \pm 0.05)\,\mathrm{ML}$ of QT, off-center, extracted intermolecular distance above $(12 \pm 1)\,\text{Å}$. **(c)** $(0.88 \pm 0.05)\,\mathrm{ML}$ of QT, extracted intermolecular distance $(12 \pm 1)\,\text{Å}$. **(d)** $(1.02 \pm 0.05)\,\mathrm{ML}$ of QT, extracted lattice constants $a_1 = (9.1 \pm 0.2)\,\text{Å}$ and $a_2 = (20.0 \pm 0.2)\,\text{Å}$. The reciprocal unit cell ($\Gamma = (102.6 \pm 1)^\circ$) is shown in blue. The domain orientation is $\delta = (5 \pm 1)^\circ$ vs. the $[\bar{1}\bar{1}2]_{\mathrm{Au}}$ direction. **(e)** Model of the ML unit cell of QT on Au(111) [55]. **(f)** STM image ($9 \times 20\,\mathrm{nm}^2$, V = -0.6 V, I = 200 pA) of a QT ML on Au(111) with indicated $[\bar{1}\bar{1}2]_{\mathrm{Au}}$ direction (from Ref. 81).

HBC on Ag(111)

The next system investigated is HBC on Ag(111). In a fashion similar to the previous experiments on QT, several LEED pattern have been acquired at different coverages of HBC on Ag(111). Figure 5.2 shows four exemplary patterns taken between 0.45 ML and 1.02 ML. Here, a diffuse ring can already be observed at the lowest coverage in pattern (a). The ring expands and sharpens upon further deposition of molecular material (Fig. 5.2(b)). In the interval between ≈ 0.75 ML and ≈ 0.9 ML coverage, a pattern of spots emerges that exhibits a twelve-fold symmetry. It is tempting to explain this pattern by combining the substrate symmetry and a single hexagonal HBC lattice (including mirror domains). However, an analysis of the domain angle $\delta = \angle(\mathbf{a}_1^*, [\bar{1}\bar{1}2]_{Ag})$ yields two unequal phases with $\delta = (0 \pm 1)^\circ$ and $\delta = (30 \pm 1)^\circ$. As it is the most prominent difference between both, the domain angle δ will be used to *name* the phases. The inequality between both is evidenced best by the alternating smaller and larger separations between neighboring (0,2) and (1,2) spots of the 0° and 30° phase, respectively. In Fig. 5.2(d) the LEED pattern of a full HBC ML is shown. Here, only the 30° phase is observed anymore, however, with a significantly decreased lattice constant.[1]

A detailed discussion of both phases of HBC on Ag(111) in terms of epitaxy can be found in Chapter 6. Here, the fact shall be mentioned that the occurrence of both can probably be explained by commensurate or POL growth. The values of the lattice constants and intermolecular separations extracted from the presented LEED patterns are summarized in Figure 5.2(e) together with the error intervals and the theoretical values for relevant commensurate phases. In a first conclusion, the LEED patterns for MLs and sub-MLs of HBC on Ag(111) indicate a transition from a 2D gas phase of HBC into a highly ordered phase with distinct domain orientations, a behavior similar to that of QT on Au(111).

HBC on Au(111)

The third system under investigation is HBC on Au(111). Four exemplary LEED patterns obtained for varying coverage of HBC on Au(111) are compared in Figure 5.3. One observes only diffuse rings for a coverage below ≈ 0.7 ML (Fig. 5.3(a) and (b)) and finds separations of (21^{+2}_{-1}) Å and (20 ± 1) Å for (a) and (b), respectively. At a coverage between 0.7 ML and 0.8 ML ordering sets in. In Figure 5.3(c) diffuse rings coexist with rather broad spots indicating molecular islands in a hexagonal arrangement at a fixed domain angle δ. Here, the lattice constant is $a_1 = (15.87 \pm 0.25)$ Å while Fig. 5.3(d) shows sharp LEED spots with $a_1 = (14.56 \pm 0.2)$ Å at a coverage of 0.96 ML.

---

[1] Please note that the error intervals for a *comparison* of lattice constants are smaller than those for the *absolute* values (Section 2.3)

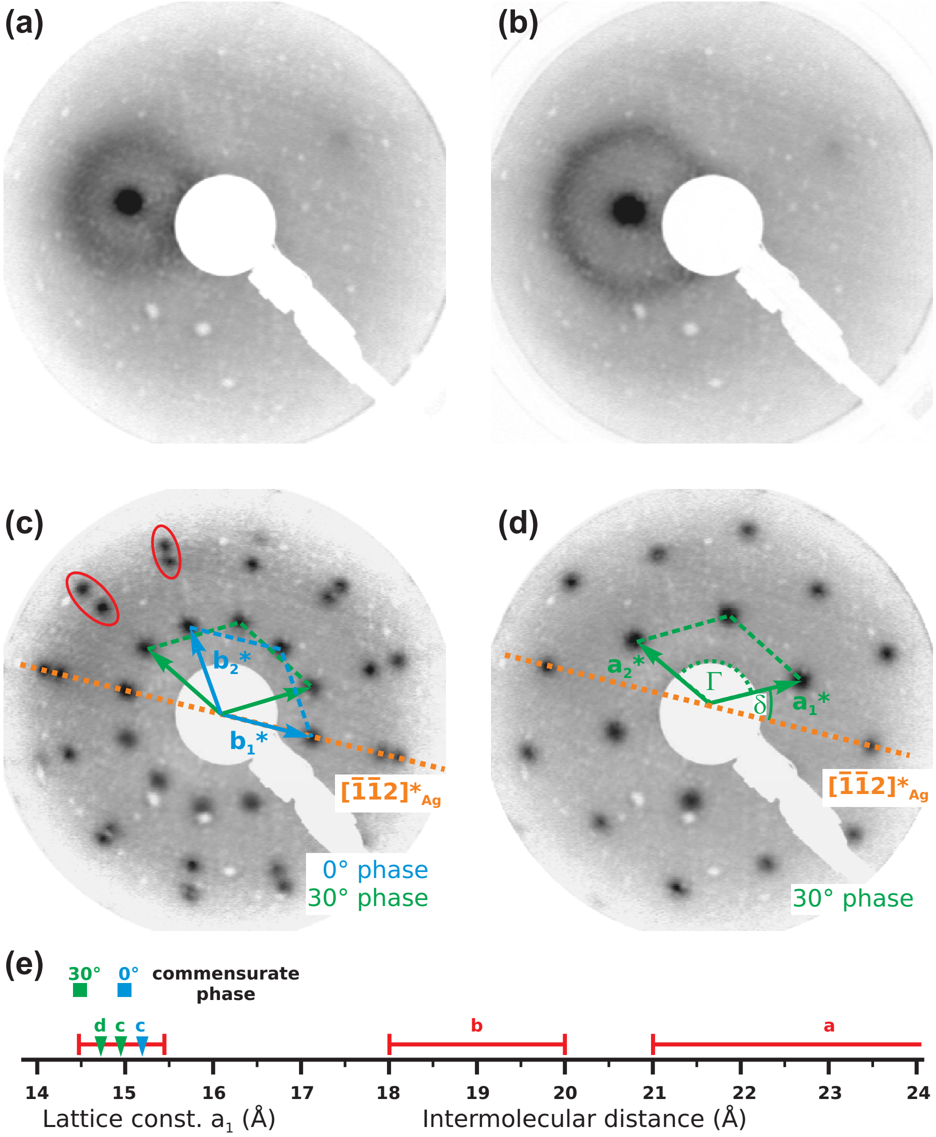

Figure 5.2: LEED patterns for varying HBC coverage on Ag(111). All images have been recorded at $E_0 = 10.4\,\mathrm{eV}$. **(a)** $(0.45 \pm 0.05)\,\mathrm{ML}$ of HBC, off-center, extracted intermolecular distance (23 ± 2) Å. **(b)** $(0.68 \pm 0.05)\,\mathrm{ML}$ of HBC, off-center, extracted intermolecular distance (19 ± 1) Å. **(c)** $(0.88 \pm 0.05)\,\mathrm{ML}$ of HBC, extracted lattice constants $a_{0^\circ} = (15.18 \pm 0.25)$ Å and $a_{30^\circ} = (14.94 \pm 0.25)$ Å. The domain orientation is $\delta = (0 \pm 1)^\circ$ and $\delta = (30 \pm 1)^\circ$ vs. the $[\bar{1}\bar{1}2]_{\mathrm{Ag}}$ direction. The red ellipses highlight the $(0,2)_{0^\circ}$ and $(1,2)_{30^\circ}$ spots, and vice versa. These pairs of LEED spots show different spacings, thus indicating different lattice constants for the 0° and 30° phase. **(d)** $(1.02 \pm 0.05)\,\mathrm{ML}$ of HBC, extracted lattice constant $a_{30^\circ} = (14.70 \pm 0.25)$ Å. The reciprocal unit cell ($\Gamma = (120 \pm 1)^\circ$) is shown in green. **(e)** Summary of the lattice constants (error bars in red). The theoretical lattice constants of the commensurate 0° and 30° phase are indicated.

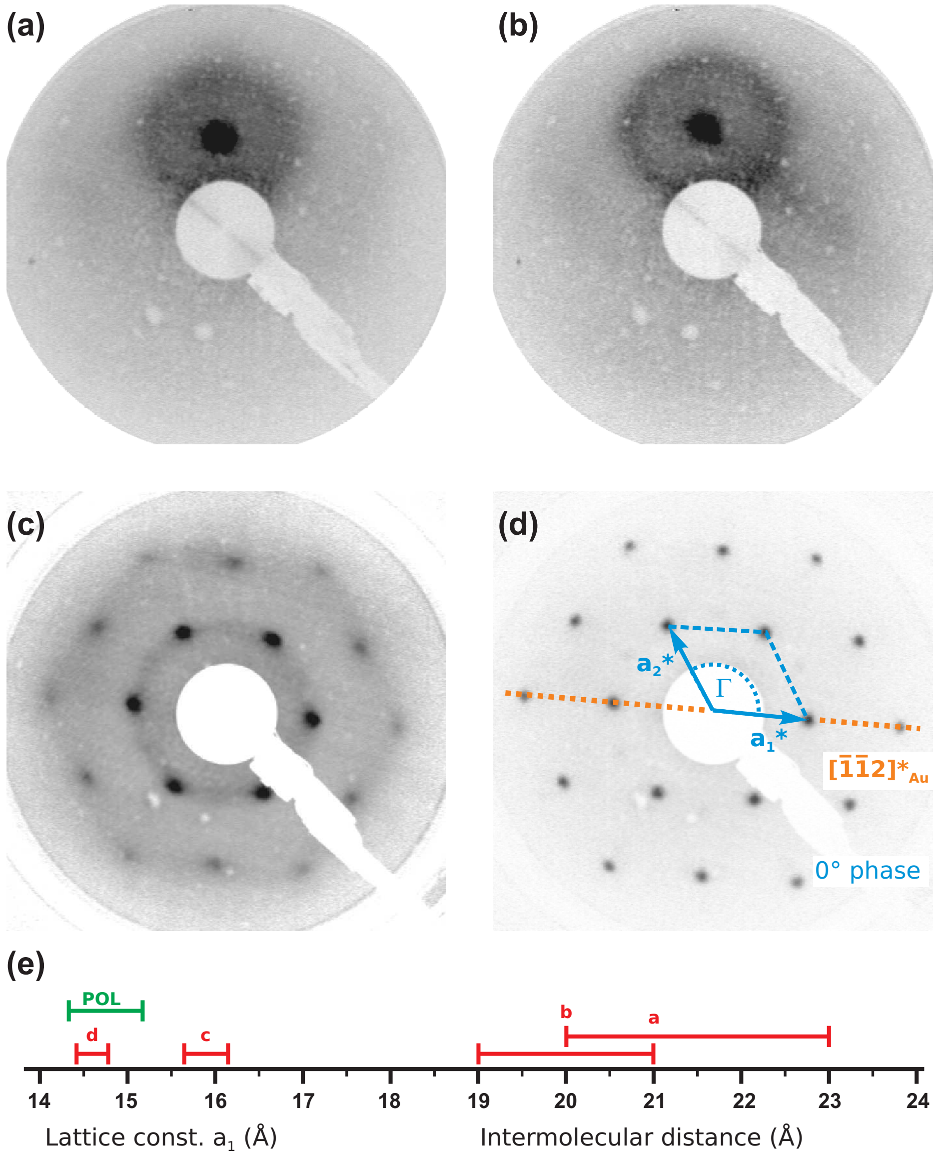

Figure 5.3: LEED patterns for varying HBC coverage on Au(111). All images have been recorded at $E_0 = 10.4\,\mathrm{eV}$. **(a)** $(0.48 \pm 0.05)\,\mathrm{ML}$ of HBC, off-center, extracted intermolecular distance (21^{+2}_{-1}) Å. **(b)** $(0.63 \pm 0.05)\,\mathrm{ML}$ of HBC, off-center, extracted intermolecular distance (20 ± 1) Å. **(c)** $(0.82 \pm 0.05)\,\mathrm{ML}$ of HBC, extracted lattice constant $a_1 = (15.87 \pm 0.25)$ Å. **(d)** $(0.96 \pm 0.05)\,\mathrm{ML}$ of HBC, extracted lattice constant $a_1 = (14.56 \pm 0.2)$ Å. The reciprocal unit cell ($\Gamma = (120 \pm 1)°$) is shown in blue. The domain orientation is $\delta = (0 \pm 1)°$ vs. the $[\bar{1}\bar{1}2]_{\mathrm{Au}}$ direction. **(e)** Summary of the lattice constants (error bars in red). The region where, in principle, point-on-line growth could occur is indicated.

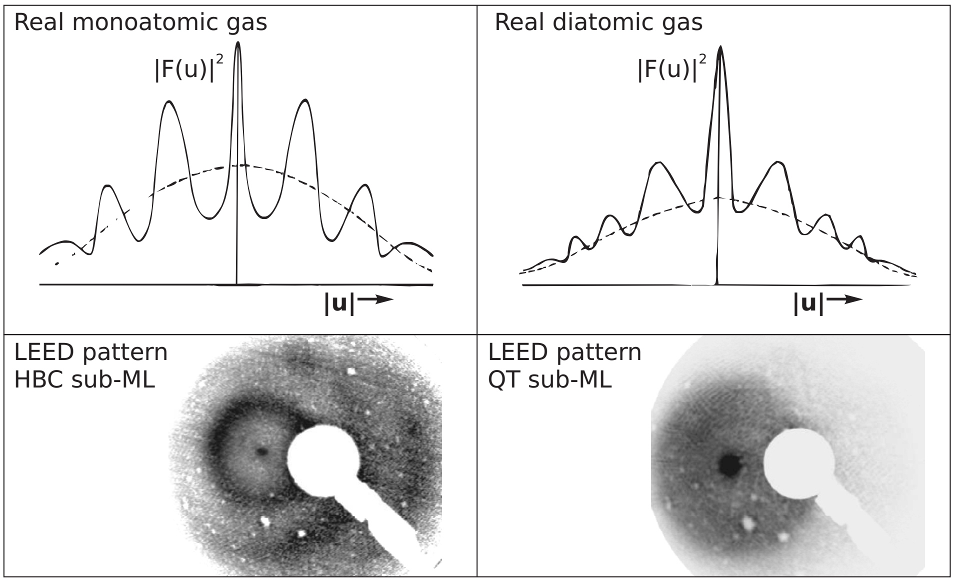

Figure 5.4: LEED patterns of $(0.7 \pm 0.05)\,\mathrm{ML}$ of HBC or QT on Au(111) exhibiting properties similar to that of theoretical scattering power distributions of a monoatomic or diatomic gas (from Ref. 62), respectively. **Left hand side:** Pronounced maxima in the theoretical curve correspond to visible rings in the LEED pattern of HBC. **Right hand side:** The theoretical curve for a diatomic gas is rather dominated by a background, diminishing for large values of $|\mathbf{u}|$, which corresponds to the observation of a halo in the LEED pattern of QT.

The definition of a ML coverage of HBC on Au(111) used throughout this work refers to the *highest* density of HBC molecules observed in a closed layer which equals 0.57 molecules per nm^2 at a lattice constant of $14.2\,\text{Å}$. A detailed investigation of the growth of HBC from 0.8 ML up to 1.0 ML shows systematic variations of the lattice constant a_1: With increasing coverage, a_1 decreases from $\approx 16\,\text{Å}$ (where the ordered phase still coexists with disordered molecules) to a minimum of $(14.2 \pm 0.2)\,\text{Å}$.

Prior to a discussion of the observed persistency of the 2D gas phases in all three systems, a short analysis and comparison of the respective *diffuse* LEED patterns shall be made. The major difference between the patterns belonging to HBC and QT samples is the occurrence of a ring, in contrast to a halo, even at low coverage. A reason for this effect can be found in the different shapes of both molecular species. While HBC is approximately disc-like, QT is a rather rod-like molecule. Thus, the minimum distance between two HBC molecules only weakly depends on their azimuthal orientations $\zeta_{1,2}$ while for QT a strong dependency on ζ can be assumed. In that sense, the observed diffuse LEED patterns for HBC and QT can be understood as examples for the theoretical diffraction patterns of a real[2] *monoatomic* gas (HBC), or a real *diatomic* gas (QT). The respective comparison is made in Figure 5.4. For

---

[2] “Real” in contrast to “ideal”.

HBC, a diffraction pattern is chosen which nicely reflects the occurrence of *several* diffuse rings in analogy to the theoretical result. The oscillations in the theoretical curves (from Ref. 62) result from an excess of atoms at the "nearest neighbor" distance, as well as at the second nearest neighbor distance and so on. The respective distances are given by the density and the size of the atoms or molecules. The averaging over all angular orientations in case of a diatomic gas (or layer of QT molecules, respectively) leads to a dominant smooth background.

A behavior similar to the disordered phase and coverage dependent lattice constants found for QT and HBC, was observed before for other molecule-metal combinations. It was ascribed to a lack of intermolecular interactions [82, 83], or even a repulsive interaction [84–86], without further explanation. Remarkably, most of the molecules for which repulsion was discussed are aromatic hydrocarbons without heteroatoms, for example perylene, coronene, naphthalene, *para*-hexaphenyl, and *para*-quaterphenyl. Recently, a repulsive interaction was reported for the donor molecule tetrathiafulvalene (TTF) on Au(111), and the charge transferred to the substrate was calculated by DFT [87]. Similarly, the intermolecular repulsion in sub-ML films of the phthalocyanine (Pc) molecules SnPc and CuPc on Ag(111) could be linked to a charge donation/backdonation effect [88]. One aspect of this chapter is to demonstrate that the observed repulsion in sub-ML HBC films on Au(111) can finally explain the discrepancies in the published data on the lattice constants and the epitaxial relation in this system [35, 40, 80].

For an attractive intermolecular interaction, small islands are evidently formed already at low coverage. In contrast, under the influence of a repulsive interaction, no molecular lattice is formed up to a relatively high coverage. The coverage at which nucleation occurs is probably characterized by an intermolecular distance that sterically hinders free molecular rotation (Fig. 5.5(d)). According to the experimental results, there is a transitional range for the lattice formation of HBC at lattice constants in between $15\,\text{Å} < a_1 < 17\,\text{Å}$, with a coexistence of ordered and disordered regions at $a_1 \approx 16\,\text{Å}$. At this coverage a "pre-lattice" is formed within which the molecules are still quite mobile. Upon ongoing deposition, the intermolecular distances are further reduced, finally forcing the molecules into a regular lattice.

In order to model this behavior quantitatively, detailed information on the structure of the HBC film is necessary. While the unit cell parameters a_1 and $\alpha = (60 \pm 1)^\circ$ are derived from LEED, the angle ζ between the short symmetry axis of HBC and a primitive lattice vector is deduced by analyzing the STM image in Figure 5.5(c). It shows a contrast-enhanced version of Fig. 5.5(b) and exhibits an intramolecular structure corresponding to the HOMO of HBC. The analysis yields $\zeta = (5.0 \pm 1.5)^\circ$, a value that allows adjacent H atoms to interlock as illustrated by two model molecules.

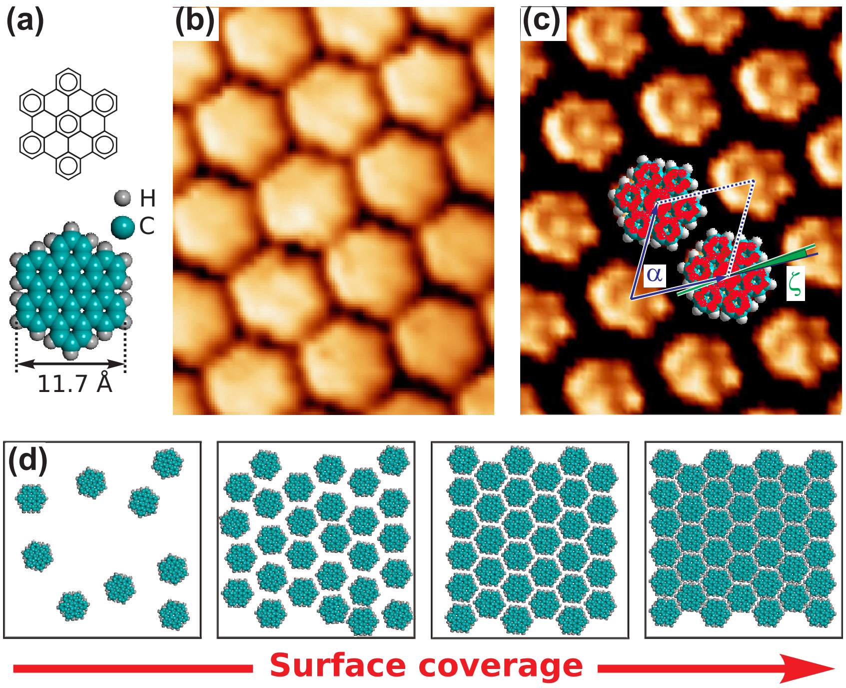

Figure 5.5: **(a)** Skeletal formula and a space-filling model of HBC. **(b)** STM image ($4.5 \times 6.0\,\mathrm{nm}^2$, V = -1.4 V, I = 75 pA) of a HBC ML on Au(111). **(c)** Contrast-enhanced version of (b). Orientation and size of two HBC molecules (HOMO shown in red) are adjusted to match the STM contrast. The deduced angle between the short axis of HBC and a primitive lattice vector is $\zeta = (5 \pm 1.5)°$. **(d)** Schematic model of the molecular growth under a repulsive potential.

In several publications reporting a repulsive interaction between adsorbed molecules, this behavior is attributed to Coulomb forces originating from localized charge redistributions, i.e., interface dipoles [85, 87, 88]. In the absence of another charge transfer mechanism such dipoles result mainly from the *push-back* or *cushion* effect. In the following, an analysis shall be made that clarifies whether the observed repulsion with a continuous change of the HBC lattice constant can be understood as the result of such “push-back dipoles”. The central question is whether the Coulomb repulsion actually dominates the attractive van der Waals forces. The main reason why HBC and not QT has been chosen for this deeper theoretical analysis is found in the simple hexagonal unit cell of this molecule, allowing a description by one lattice constant only. Furthermore, HBC on Au(111) bears a more general relevance for this work as it functions as a substrate for organic-organic heterosystems as well.

5.2 Modeling technique

The model used to describe the intermolecular forces in a HBC layer consists basically of two parts. Firstly, the Coulomb interaction due to partial charges on the molecules and due to localized dipoles resulting from the push-back effect, and secondly, the van der Waals forces consisting of attractive London and repulsive Pauli forces. In the following, these contributions will be discussed separately:

The charge distribution in the HBC molecule (relevant for the intermolecular Coulomb potential) is calculated for a free HBC molecule by the semiempirical PM3 method (using a commercial software [89]) assigning a *partial* charge to each atom. The Coulomb potential between two molecules is then calculated as the sum over all atom-atom pair potentials as described in Section 3.2.2. As UPS measurements reveal a low density of states (DOS) at the Fermi level of a HBC ML on Au(111) [80], on can conclude a mainly physisorptive binding of HBC to the Au(111) surface. In turn, this leads to the assumption that the electronic structures of both, the adsorbate and the substrate, are only weakly perturbed. Consequently, the use of charge distributions calculated for an isolated HBC molecule in vacuum should be sufficiently correct. The presence of the metal is accounted for by the introduction of mirror charges. According to Ref. 90, the effective location of the metal surface in the presence of an external charge is 1.94 Å above the terminal lattice plane of Au(111). As no data for the precise adsorption height of HBC on Au(111) is available, the value measured for the well studied system of PTCDA on Au(111) is chosen instead. PTCDA is physisorbed on Au(111) at a height of 3.27 Å above the Au(111) surface atoms [27]. The total distance between charge and image charge amounts thus to 2.66 Å. The accuracy of this value is hard to estimate, which is, nevertheless, acceptable as the influence of the mirror charges is rather weak for the intermolecular separations found in an ordered HBC film ($14.2\,\text{Å} < a_1 < 16\,\text{Å}$).

The push-back effect occurs upon adsorption of planar molecules on metals when the electron density spilling out of the bare surface is pushed back. According to several corresponding theoretical calculations [87, 91], a dipole perpendicular to the surface is formed that is localized below the molecule. This effect is modeled by a circular plate capacitor using the following parameters that are in accordance with the DFT calculations in Ref. 91: The plate separation is $l = 2\,\text{Å}$ and the charge density on each plate is $\rho = 0.3\,\text{e/nm}^2$. One should note that the value for l is not identical to the value that the authors themselves give for a plate capacitor model in Ref. 91. This discrepancy is due to the fact that Rusu et al. construct a capacitor to simulate the interface dipole, while here the actual charge distribution is relevant. The diameter of the capacitor is given by the size of the molecule. An upper limit of $d = 12\,\text{Å}$ is chosen in accordance to the dimensions given in Fig. 5.5(a). In doing so, the influence of this push-back dipole is probably overestimated, as calculations in Ref. 91 show that the push-back effect manifests itself especially in the region of the aromatic system. Although the above assumptions constitute a rather basic model, the results do not depend on a high accuracy of this particular component as will be shown in the next section.

The calculation of the van der Waals potential in the film V_{intra}, and between two individual molecules, $V_{mol-mol}$, is conducted as described in Section 3.2.2 by using a force-field method with OPLS parameters.

Complete negligence of the molecule-surface potential V_{inter} as done in this chapter cannot be justified in general, but only for the present lattice/molecule orientation of HBC on Au(111) ($\delta = (0 \pm 1)°$). Usually, one would have to consider minima in V_{inter}, i.e., epitaxial structures like commensurate or POL epitaxy. For the observed HBC lattice, however, such epitaxial growth is possible only in a small lattice constant region (green bar in Fig. 5.3(e)), and even there, the energetic gain V'_{inter} related to the epitaxial structures is almost negligible. The according potential energy calculations will be discussed in Chapter 6.

5.3 Results of the model calculation

The intermolecular Coulomb potential calculated as a function of the molecule-molecule distance is shown in Figure 5.6. The PowerGrid calculation is performed for two HBC molecules oriented at the observed angle $\zeta = 5°$ and for the respective push-back dipoles. To illustrate a key issue, a similar calculation is also performed for a different molecular species with a dissimilar behavior: Two PTCDA molecules in a geometry resembling the unit cell of PTCDA on

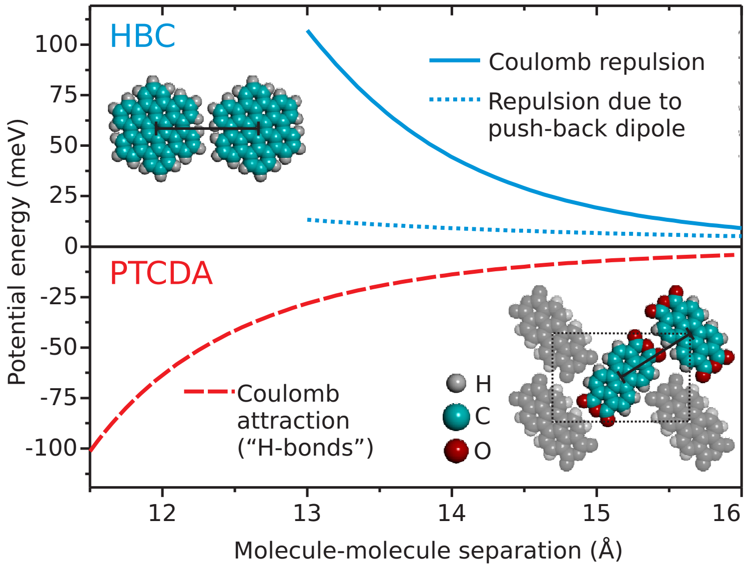

Figure 5.6: Separation-dependent Coulomb potential between a pair of two HBC molecules (solid blue), of two PTCDA molecules in the herringbone geometry (dashed red), and of two circular push-back dipole plate capacitors (d = 12 Å, $\rho = 0.3\,\mathrm{e/nm^2}$) (dotted blue).

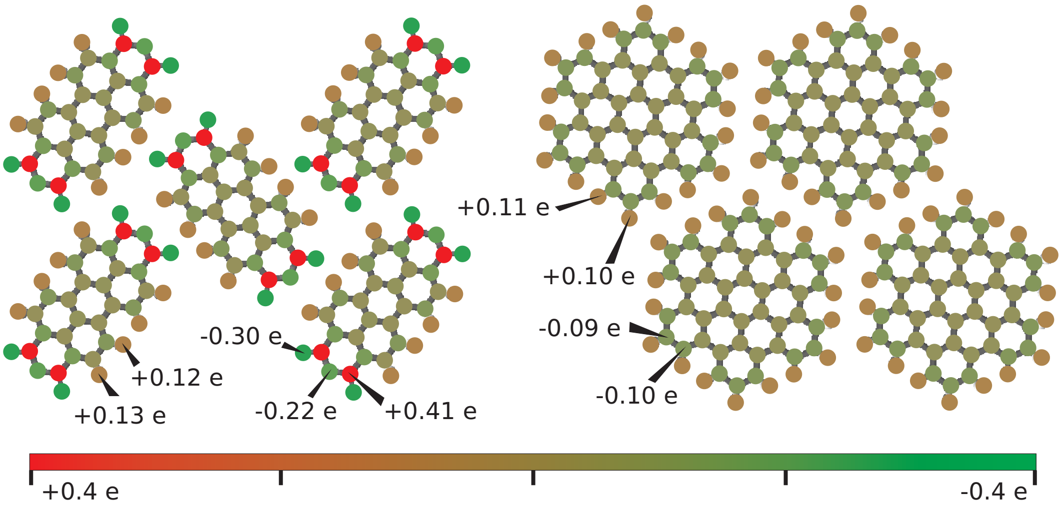

Figure 5.7: A comparison of the partial charges in free PTCDA and HBC molecules as calculated by PM3. The molecules are arranged according to the respective ML phase on Au(111), in order to illustrate the influence of partial charges on the structure of the film. In the herringbone motif, typical for PTCDA, negatively charged oxygen and positively charged hydrogen atoms face each other ("hydrogen bonds"), while no such favorable structure is possible for HBC.

Au(111) [29, 92]. While a variation of the molecular separation a_1 is meaningful for HBC (observed in the experiment), this is only done for PTCDA to illustrate the behavior of the attractive Coulomb potential. Primarily relevant is only the potential at 11.5 Å, resembling the distance of the two molecules in the PTCDA unit cell.

One immediately realizes that the intermolecular Coulomb potential is dominated by the repulsion or attraction between adjacent atoms in both molecules, i.e., repulsion between positively charged H atoms in the case of HBC and attraction between H atoms and negatively charged oxygen atoms ("hydrogen bond") in the case of PTCDA. This explanation is visualized in Fig. 5.7 by plotting the partial charges of HBC and PTCDA, respectively. The influence of the push-back dipole that is calculated for HBC only, is comparably weak. This result coincides well with the fact that a repulsive interaction in a sub-ML has been observed for molecules without heteroatoms in the outer rim only, while, for example, PTCDA grows in islands at sub-ML coverage [93]. The case of TTF on Au(111) [87] is slightly different, as there the charge density (in a plate capacitor model) would be much higher due to the donor character[3] and the small size of this molecule.

The question whether the total Coulomb repulsion between the HBC molecules can account for the observed behavior on Au(111) is addressed in Fig. 5.8.

---

[3] If the molecule donates electron density to the metal substrate, this charge transfer adds to the push-back dipole, while a charge transfer in opposite direction would cancel the effect partially [94, 95].

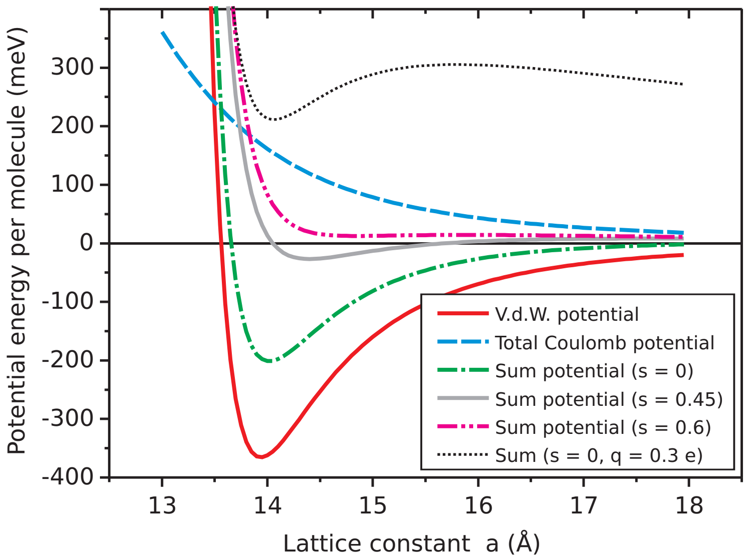

Figure 5.8: Different intermolecular potentials (per molecule) calculated in a closed HBC layer. The potential curves labeled "Sum" arise when adding the total Coulomb potential and the van der Waals potential. If s is below 1, the van der Waals potential is modified according to Eq. 5.1. The dotted black curve is calculated with an additional net charge q on each HBC molecule.

Here, the calculation is performed for a HBC ML with a hexagonal unit cell and as a function of the lattice constant a_1. Consequently, the energies (per molecule) are larger by a factor of ≈ 3 compared to the values in Fig. 5.6, due to the six next neighbor molecules. In Fig. 5.8, the total Coulomb potential (dashed blue curve) is compared to the van der Waals potential (solid red curve) and to the sum of both, i.e., the total intermolecular potential according to the model discussed above (dashed-dotted green curve). Clearly, the observed repulsive behavior is not reflected by the total potential energy curve which is attractive over the whole lattice constant range between 14 Å and 18 Å. Possible origins of this discrepancy will now be discussed one by one, starting with issues directly related to the model used.

5.4 Discussion of results

It is unlikely that the influence of the push-back dipole is largely underestimated by the method used. Although the plate capacitor model is of very basic nature, the overall repulsion could be explained only if the model underestimated the repulsive effect by a factor of 20. Despite this huge deviation, such a strong influence would render the difference between, for example, PTCDA and HBC almost irrelevant which is by no means reflected in the experimental results.

The repulsion between the partial charges on neighboring HBC molecules should be reproduced rather accurately by the model. Here, a factor of 3 would be necessary to explain the repulsion. This would, in turn, mean a strong modification of the intramolecular charge distribution upon physisorption, which is completely implausible.

The existence of a hypothetical net charge on each molecule in the layer is, in principle, a way to explain the repulsion. While such a charge could emerge from a charge transfer from/to the substrate, only a very small partial charge, if any, is expected to be on the molecules due to this mechanism. The lowest unoccupied molecular orbital (LUMO) of the adsorbed HBC is not below the Fermi level E_F, and the DOS at E_F is very small [80]. Consequently, no (partial) filling of molecular orbitals is expected for HBC on Au(111), pointing toward a physisorptive binding. A *small* net charge on the molecules would, even if present, not be sufficient to explain the repulsion as shown for the case of a charge of $q = +0.3\,\mathrm{e}$. The respective dotted black curve in Fig. 5.8 implies, although at positive energies, still an attractive force in the region between 14.0 Å and 15.8 Å.

As mentioned in Section 3.2.2, the force-field method with OPLS parameters correctly reproduces the intermolecular potential in thick HBC films and can thus not be the source of the huge discrepancy. In the case of molecules adsorbed directly and planar on a metal surface, however, the results obtained by this method might indeed differ significantly from the actual situation as the *influence of a substrate* is not included in the OPLS parameters. As the London forces responsible for the attractive part of the LJ potential result from polarization fluctuations on the molecules, they are subject to screening by the metal electrons which "compensate" the temporary dipoles (Fig. 5.9).

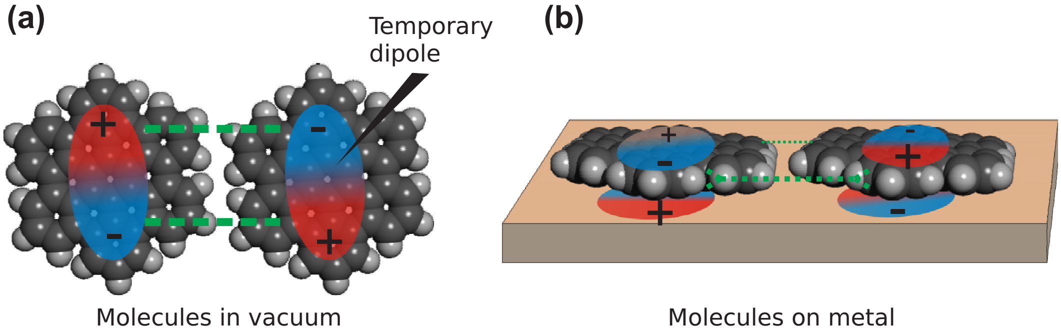

Figure 5.9: **(a)** Illustration of the (London-) attraction caused by fluctuating dipoles in the delocalized aromatic system of two HBC molecules. Here, one single polarization mode, with a dipole parallel to the long symmetry axis of HBC, and the respective dipole induced in a neighboring molecule is shown at a certain point in time. **(b)** On a metal surface, a dipole is induced in the free electron gas below each molecule as well, thus partially screening the dipoles in the molecules. As a results, the intermolecular London force is considerably reduced [96].

Several publications deal with the phenomenon of such a screening in case of adsorbed rare gas atoms [96–98] or macroscopic particles [99, 100]. As the considerations made in these papers are of universal character, the main ideas can most likely be transferred to molecular adsorbates as well. While in Refs. 97 and 98 the remaining attraction is $\geq 2/3$ of the value in vacuum, Mahanty shows that an even stronger screening may occur if the molecules are partially "embedded" in the electron density spilling out of the metal surface [96]. Then, the screening-strength depends on the surface plasmon frequency of the metal substrate, and a higher plasmon frequency leads to a stronger screening effect. As the lowest absorption frequency of HBC (about 2.8 eV) [101] is in the range of the plasmon frequency of Au (2.5 eV) [102], a considerable weakening of the molecule-molecule attraction should be expected. Although no precise value for the screening strength of the London forces can be given (the model in Ref. 96 is too simple to be fully transferable), the screening can be accounted for by a parameter s in the Lennard-Jones potential (Eq. 3.16) such that $s = 0$ means no screening while $s = 1$ would be a full screening of the London attraction.

$$V_{aa} = 4\epsilon \left\{ \left(\frac{\sigma}{r}\right)^{12} - (1-s)\left(\frac{\sigma}{r}\right)^{6} \right\}. \tag{5.1}$$

In Figure 5.8 a comparison of the total potential for $s = 0$, $s = 0.45$ and $s = 0.6$ is made, revealing that only in the case of the strongest screening considered ($s = 0.6$), a potential curve is obtained that is repulsive in the whole lattice constant range.

A direct evidence for the influence of the metal substrate is given by the observation of an immediate ordering process in HBC sub-ML *on PTCDA on Au(111)* (see Chapter 7). Here, even at low coverage, close-packed islands are formed, indicating an attraction between individual HBC molecules if the direct vicinity to the metal is lifted.

As mentioned, the effect of a significantly reduced attraction between atoms or molecules adsorbed on a surface was subject to several theoretical investigations [97]. These calculations predict no repulsion but only a reduction of the attractive r^{-6} term. This is, however, no contradiction to the results discussed here as there are no partial charges in the spherical "molecules" in those models. In contrast, the non-uniform charge distribution and the resulting repulsive Coulomb interaction accounts for the observed repulsion between QT or HBC molecules.

Here, a remark on the influence of the entropy on the observed repulsion is necessary: It is practically impossible to include the free energy $F = U - T \cdot S$, rather than the internal energy U, into the theoretical considerations as the investigated system is far too complex to obtain an accurate value ΔS for the observed phase transition. It is nevertheless possible to estimate whether thermal excitation alone is sufficient to explain the observed repulsion. Under the assumption of an unscreened London attraction ($s = 0$), the potential energy

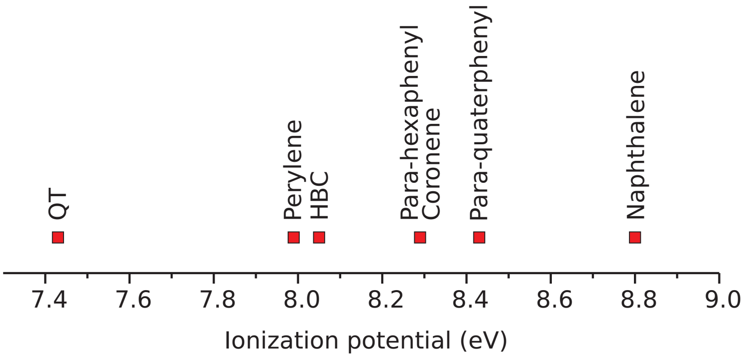

Figure 5.10: Ionization potentials of several hydrocarbon molecules for which a repulsive interaction was observed at sub-ML coverage. The values are the result of a PM3 calculation for a free molecule.

minimum shown in Fig. 5.8 (dashed-dotted green) has a depth of 200 meV which has to be compared to $kT = 25\,\mathrm{meV}$. A "bound state", i.e., a stable molecular island is hence expected if no screening would occur. This is in contradiction to the experimental results. Whether the *real* potential energy curve is entirely repulsive for HBC ($s = 0.6$) or whether it is weakly attractive with a shallow minimum of depth $\approx kT$ in a certain lattice constant range ($s = 0.45$) cannot be completely answered.

The ionization potentials of hydrocarbon molecules for which a repulsive interaction on Au(111) or Ag(111) has been reported are compared in Fig. 5.10. Due to the significant spread in the values, it is unlikely that specific electronic properties play a role in the observed repulsion. Furthermore, an influence of a distinct feature of the molecular structure is out of the question as, with HBC on the one hand and *para*-hexaphenyl on the other hand, a very compact disk-like hydrocarbon and a very elongated rod-like one are both members of this group. The conclusion that such a repulsive behavior is a property of most hydrocarbon molecules seems justified in the light of the discussion in this chapter. A final proof can, however, only be obtained experimentally.

5.5 Conclusion

A phase transition from a disordered isotropic distribution of QT and HBC molecules on noble metal surfaces to a highly ordered phase is found at a coverage in the range of 0.9 ML and 0.7 ML, respectively. A detailed investigation of the system HBC on Au(111) revealed a coverage-dependent and thus tunable lattice constant once a lattice was formed. The intermolecular potential in this system has been modeled, including intermolecular Coulomb and van der Waals forces. The results show that the (push-back) interface dipole accounts only for a small part of the Coulomb interaction and is outweighed by the (in the case of HBC: repulsive) Coulomb forces between partial charges on neighboring molecules. It could be shown as well that the repulsive nature of the total intermolecular potential can only be obtained by assuming a partial screening ($s \approx 0.6$) of the attractive London forces due to the presence of the metal substrate. Although the accuracy of this estimation is naturally limited by the simplicity of the model used, the occurrence of a considerable screening together with the lack of attractive Coulomb forces provides a plausible explanation not only for the case of HBC discussed here but also for the repulsion observed for other molecular species at sub-ML coverage. It turns out that HBC on Au(111) is very interesting as a starting point for the fabrication of organic-organic heterosystems as mentioned in the Introduction. The repulsive potential allows the growth of HBC ML domains with a substantially reduced density of defects, holes, grain boundaries, or molecules in the second ML and, in addition, with a freely tunable lattice constant (between 14.2 Å and $\approx$ 16 Å). However, before the focus shall be moved to such heterostructures based on a ML of HBC on Au(111), an attempt will be made to further clarify the growth of HBC on Ag(111) and Au(111). Only comprehensive knowledge of the substrate allows to fully understand the respective heterosystems. Therefore, the next chapter deals with the influence of the substrates' crystalline structure on the HBC overlayer, i.e., the role of epitaxy in these systems.

6 The Ordered Phases of HBC on Ag(111) and Au(111)

The epitaxial relation of many organic-on-inorganic systems that form islands at sub-ML coverage has been studied intensively. In contrast, little is known about the ordering principles under the presence of a repulsive intermolecular potential as reported in the last chapter. While epitaxy plays no role in the disordered phase at all, its influence on the ordered structures has to be questioned as well. After all, the coverage dependent lattice constants imply a continuous change in the epitaxial relation during the growth of a ML film. The balance between the different phases observed on Ag(111) and Au(111) may consequently be influenced by thermal effects (molecular mobility) and the deposition rate (equilibrium vs. non-equilibrium growth). Furthermore, the question arises whether the "continuous" change of the HBC lattice constant is only a simplified model assumption. While usually the experimental results are presented first, followed by an analysis an interpretation of their meaning, this chapter is organized differently. For sake of a self-contained presentation, all epitaxial structures that feature an almost hexagonal unit cell with $14\,\AA < a_1 < 16\,\AA$ *and hence could be relevant for the growth of HBC are discussed first.*

A comparison of HBC on Au(111) and Ag(111) is rewarding as, on the one hand, the bulk lattice constants of Au and Ag are almost identical, while, on the other hand, different electronic and chemical properties as well as the reconstruction of the Au(111) surface allow to identify the origin of the structural ordering of HBC on the respective substrates. While in the last chapter the genesis of molecular domains has been discussed in terms of a compression of the molecular film with increasing coverage, no explanation was presented yet for the occurrence of distinct domain angles δ.

In this chapter the numerous epitaxial relations in the observed HBC lattice constant range are introduced. Subsequently, the energetic gain V'_{inter} associated to these phases is calculated by a force-field approach. The results allow assessing whether a certain epitaxial phase should come in consideration for a local minimum in the total potential $V_{total} = V_{inter} + V_{intra}$. An analysis of experimental lattice constant data for HBC on Ag(111) and Au(111) is made including a comparison to the potential energy calculations. Finally, the influence of the Au(111) surface reconstruction on the growth of HBC will be assessed.

6.1 Geometrical analysis of epitaxy

The overwhelming majority of all experimental results published on the growth of organics on metal substrates indicates that highly ordered layers occurring under a reproducible, fixed domain angle (and symmetry equivalents thereof) can be ascribed to an epitaxial growth. In those cases, only a finite number of different commensurate structures can exist in a given geometry. Here, limited by the observed hexagonal lattice of HBC and the relevant lattice constant range $14\,\text{Å} < a_1 < 16\,\text{Å}$, (Chapter 5), only four commensurate lattices exist on Au(111) and Ag(111), irrespective of the domain angle δ. They are summarized graphically in Figure 6.1, and the respective epitaxial matrices are listed in Table 6.1. While the commensurate overlayer lattices are perfectly hexagonal on Ag(111), the uniaxial compression of the topmost Au(111) surface layer (see Section 2.4.4) is reflected in an equally large compression of epitaxial adsorbate lattices. Consequently, none of the commensurate structures on Au(111) is a true hexagon, and the deviations of the lattice constants are in the range of 0.5 Å (Fig. 6.1(b)). This fact is of relevance as the "native" HBC unit cell *is*, based on symmetry arguments, a perfect hexagon.

It is obvious that the coverage dependent lattice of HBC cannot be described by the commensurate matrices alone. Still, point-on-line epitaxy, common for many organic-on-inorganic epitaxial systems [39, 76], can principally also explain a *continuous* change in the adsorbate lattice by adjusting the two matrix elements not required to be integers. The (infinite) number of POL

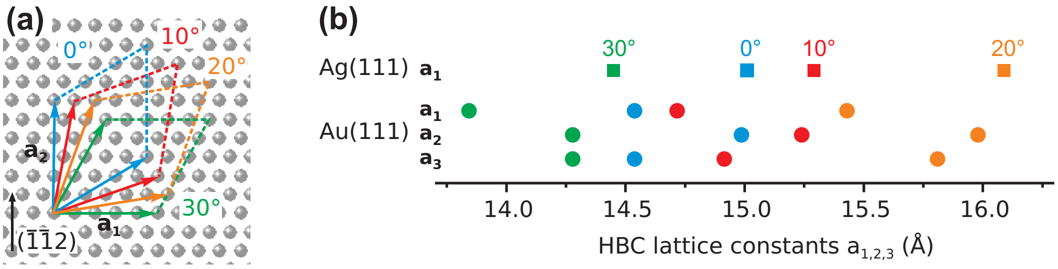

Figure 6.1: **(a)** Sketch of all hexagonal lattices commensurate with respect to the Au(111) or Ag(111) surface for lattice constants $14\,\text{Å} < a_1 < 16\,\text{Å}$. The phases are labeled according to their domain angle $\delta = \angle(\mathbf{a}_2, (\bar{1}\bar{1}2)_{Au,Ag})$. **(b)** Lattice constants $a_{1,2,3}$ of the commensurate phases from (a). While $a_1 = a_2 = a_3$ on Ag, the hexagonal symmetry of the overlayer lattice on Au(111) is lifted by the surface reconstruction.

Table 6.1: Epitaxial matrices $\mathbf{C}$ of all commensurate lattices relevant for the growth of HBC on Au(111) and Ag(111). The matrices are given with respect to the Au(111) unit cell vectors as defined in Fig. 2.8. The Ag(111) unit cell is defined similarly.

Phase	0°	10°	20°	30°
$\mathbf{C}$	$\begin{pmatrix} 6 & -3 \\ 3 & 3 \end{pmatrix}$	$\begin{pmatrix} 6 & -4 \\ 4 & 2 \end{pmatrix}$	$\begin{pmatrix} 6 & -5 \\ 5 & 1 \end{pmatrix}$	$\begin{pmatrix} 5 & -5 \\ 5 & 0 \end{pmatrix}$

lattices in agreement with the constraints discussed above is visualized in Figure 6.2 for Ag(111) and Au(111). The fact that each commensurate phase is "accompanied" by a group of related POL coincident structures with a similar geometry (domain angle δ and average lattice constant $\bar{a}$) is nicely revealed in Fig. 6.2(a). As a result of the Au(111) surface reconstruction, the diagram for HBC on Au(111) is not structured as clearly (Fig. 6.2(b)). In a first conclusion, one can state that there are indeed POL coincident lattices in the whole lattice constant range between 14 Å and 16 Å, which *could* be adopted by HBC, if the HBC lattice undergoes a certain distortion lifting the hexagonal symmetry. Whether such a distortion is favorable or not can be estimated from a potential energy calculation of a HBC layer including the molecule-molecule as well as the molecule-substrate interaction. The results of such a calculation will be analyzed in the next section.

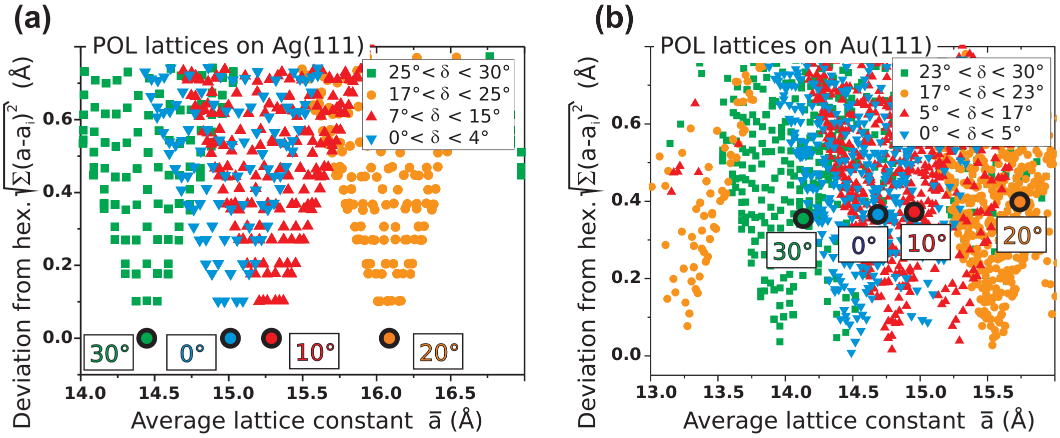

Figure 6.2: Overview over (almost) hexagonal POL coincident lattices with potential relevance for the growth of HBC. Three characteristic quantities are used to sort the numerous lattices: The average lattice constant $\bar{a} = (a_1 + a_2 + a_3)/3$, the deviation from a perfect hexagonal lattice $\sqrt{\sum (\bar{a} - a_i)^2}$, and the domain angle δ which is color-coded. The four commensurate phases are marked by filled circles. Due to the surface reconstruction, the resulting pattern on Au(111) is not as clear as the one on Ag(111).

6.2 Energetic gain of epitaxial structures

To further elucidate the relevance of the different epitaxial structures discussed, the energetic gain related to a respective lattice of HBC molecules is calculated by the force-field methods discussed in Section 3.2.2. It is not purposeful to consider the total potential $V_{total} = V_{inter} + V_{intra}$ here. On one side, the interaction within the layer is not known precisely due to the uncertainties discussed in the last chapter. On the other side, a comparison between V_{intra} values for different lattice constants is not reasonable as the coverage imposes a certain boundary condition. Instead, only the energetic gain V'_{inter} related to an epitaxial structure is discussed. The intermolecular interaction is implicitly included in the results as it influences the search for an optimal molecular orientation ζ in a given lattice geometry. Here, minimizing V_{intra} and V_{inter} are usually competing processes as there is typically no *common* minimum for one value of ζ. The calculation of V_{intra} is conducated using the standard force-field approach without any screening as in Eq. 5.1. Although this appears to be inconsistent, there are two reasons for this procedure. The calculations made should all be traceable to the maximum extent possible which is undermined by making assumptions too specific. Otherwise, a very arbitrary component would be introduced as no precise value for the screening parameter s is known. Furthermore, the interaction that is relevant for the orientation of the molecules in the layer is mainly the Pauli repulsion. This repulsion, responsible for a rotational barrier (steric hindrence), is completely independent of the screening discussed.

The energy V'_{inter} that an epitaxial HBC film gains relative to the energy E_0 of any incommensurate structure is summarized in Figure 6.3. It has been

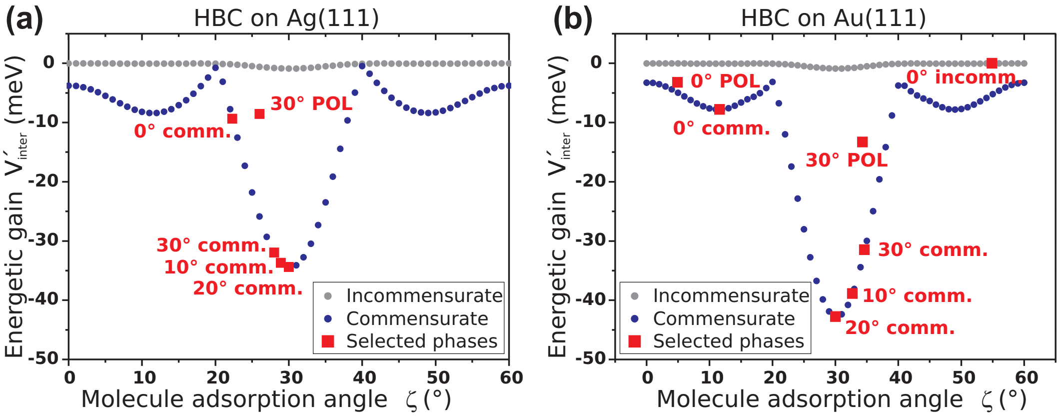

Figure 6.3: **(a)** Potential energy gain V'_{inter} (Eq. 4.6) calculated for commensurate and incommensurate growth of HBC plotted as a function of the molecular orientation ζ (circles). A variety of different specific epitaxial structures on Ag and Au is marked by squares. The parameters for the POL phases are: 30° POL on Ag: $\bar{a} = 14.7\,\text{Å}$, 30° POL on Au: $\bar{a} = 14.0\,\text{Å}$, 0° POL on Au: $\bar{a} = 14.3\,\text{Å}$

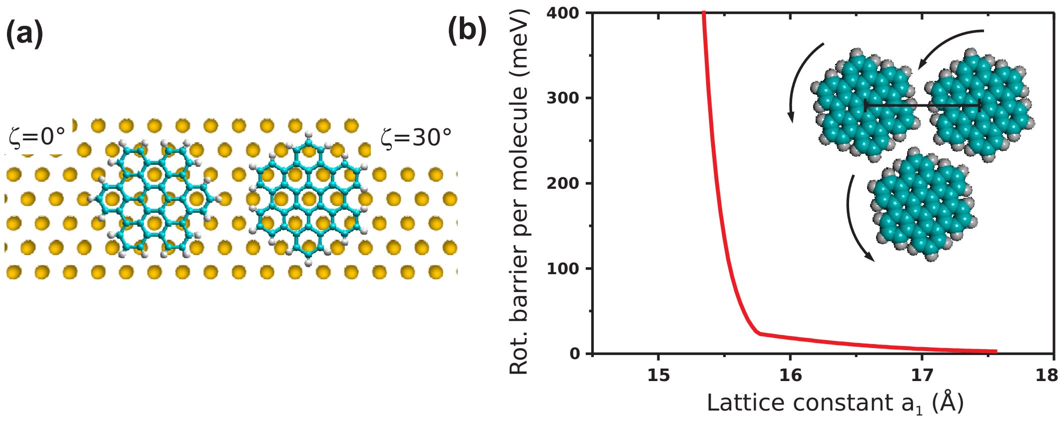

Figure 6.4: **(a)** Preferred adsorption position for a HBC molecules with $\zeta = 0°$ or $\zeta = 30°$ according to PE calculation. **(b)** Difference $V_{intra}^{worst} - V_{intra}^{best}$ between the mol-mol potential for the worst and the best molecular orientation. This quantity thus represents the energetic barrier that has to be overcome for a free rotation of the molecules (if $V'_{inter} = 0$, i.e., for incommensurate growth).

calculated for HBC domains on Ag(111) and Au(111), each containing 1000 molecules. In these calculations the unit cell geometry and the domain angle δ remained fixed, while the position of the domain on the surface as well as the azimuthal orientation ζ of the individual molecules were subject to optimization. The energetic gain and the value of ζ related to specific commensurate or POL coincident lattices are compared in Fig. 6.3 (red squares). In addition, the gain in *any* commensurate or incommensurate phase is plotted as a function of ζ (blue and gray circles). This gain is *independent* of the lattice geometry and consequently all specific commensurate structures (with red label) are located on this curve as well. The energetic gain in any POL structure is lower than that of a commensurate phase (see Chapter 4) if the molecular orientations ζ are identical. Thus, the POL coincident phases in Fig. 6.3 are situated between commensurate and incommensurate energy.

Several aspects in Figure 6.3 are noteworthy:

- There are strong variations in V'_{inter} in the commensurate case: $V'_{inter}\,(\zeta = 30°)$ is 9 or even 13 times larger than $V'_{inter}\,(\zeta = 0°)$ on Ag and Au, respectively. $V'_{inter}\,(\zeta = 20°)$ is virtually zero on Ag(111). This strong dependency results from the similar hexagonal structures of the (111) metal surface and the graphitic carbon body of HBC. The preferred adsorption positions, according to the potential energy calculations, are shown in Fig. 6.4(a) for the two exemplary orientations $\zeta = 0°$ and $\zeta = 30°$ (not to be mixed up with the domain orientation δ which is used to name the different phases of HBC).

- As a consequence, also the four commensurate phases discussed before (0°, 10°, 20°, 30°) are very dissimilar in terms of energetic gain. This effect is stronger on Au(111) where, due to the distorted lattices, the sterical hindrance is higher. On Ag, the intermolecular separation in the 10°, 20°, and 30° phase is comparably large and the sterical hindrance is accordingly low. Consequently, the molecules can grow in an orientation close to the optimal angle $\zeta = 30°$, independent of the actual domain angle δ. The rotational barrier in a hexagonal HBC layer is shown in Fig. 6.4(b). In accordance with the results in Fig. 6.3, the barrier falls below $V'_{inter}\,(\zeta = 30°)$ at approximately $a_1 = 15.75\,\text{Å}$. This value lies between the commensurate 10° and 20° phases on Ag(111) (Fig. 6.1).

- While the dependence of the energetic gain on ζ is similar for HBC on Ag and Au, the maximal energetic gain on Au is approximately 20 % higher. This is mainly a property of the UFF force-field parameters for Au and Ag used in the calculation. The question, whether this difference is significant, is dealt with in Section 6.5.

Now, having accomplished an overview over the geometric and energetic properties of epitaxial structures with relevance for the growth of HBC, a comparison to the experimental results is performed.

6.3 Comparison to experiment

HBC on Ag(111)

Figure 6.5 shows a comparison of three LEED patterns of the ordered phases of HBC on Ag(111). The nominal coverages of the respective samples are 0.76 ML, 0.85 ML and 1.02 ML. Similar to the procedure in the last chapter, the lattice constants a_1 and the domain angles δ can be derived from the patterns. The extracted lattice constants of the 0° and the 30° phase are plotted vs. the coverage in Fig. 6.5(d). The plot contains data from the LEED patterns in (a)-(c), marked in red, as well as from images that are not shown. All data points, i.e., LEED patterns have been acquired on one and the same sample by alternating steps of deposition of molecules and LEED measurements. Each cycle took approximately 20 minutes.

While previously only the mere occurrence of the values $\delta = (30 \pm 1)°$ and $\delta = (0 \pm 1)°$ was noted, they can now be related to the influence of epitaxy. The two relevant commensurate structures are indicated in the plot of lattice constants vs. coverage. The most intriguing effect observable is the complete disappearance of the $\delta = (0 \pm 1)°$ domains at a coverage between 0.85 ML and 0.9 ML. While previously inexplicable, it can now be clearly related to the different lattice constants of the commensurate 0° and 30° phases: When, with increasing coverage, the HBC lattice constant is forced below 15 Å, the 0° domains loose their commensurate registry to the substrate and the related gain in potential energy V'_{inter}. Even in ≈ 0.9 ML of HBC, the mobility on the surface is obviously high enough to allow the entire 0° domains to turn into domains with the 30° orientation. This process occurs most probably at the borders of the respective domains. As suggested by the experimental results, the transformation of 0° into 30° domains occurs at a lattice constant significantly above that of the commensurate 30° phase. Still, the 30° POL phases which exist in the region $14.5\,\text{Å} < a_1 < 15\,\text{Å}$ also provide a sufficient energetic gain (see the example in Fig. 6.3(a)).

The experimental result for the growth of HBC on Ag(111) which is *not* in accordance to the analysis made so far, is the occurrence of 0° and 30° domains also at a lattice constant of $\approx 16.0\,\text{Å}$ (Fig. 6.5(a)). Here, a domain angle of $\delta = 20°$ would be expected from geometrical as well as energetic arguments (Figs. 6.2(a) and 6.3(a) respectively). A reason for this discrepancy can only be given in form of an educated guess: The very broad LEED spots in Fig. 6.5(a)

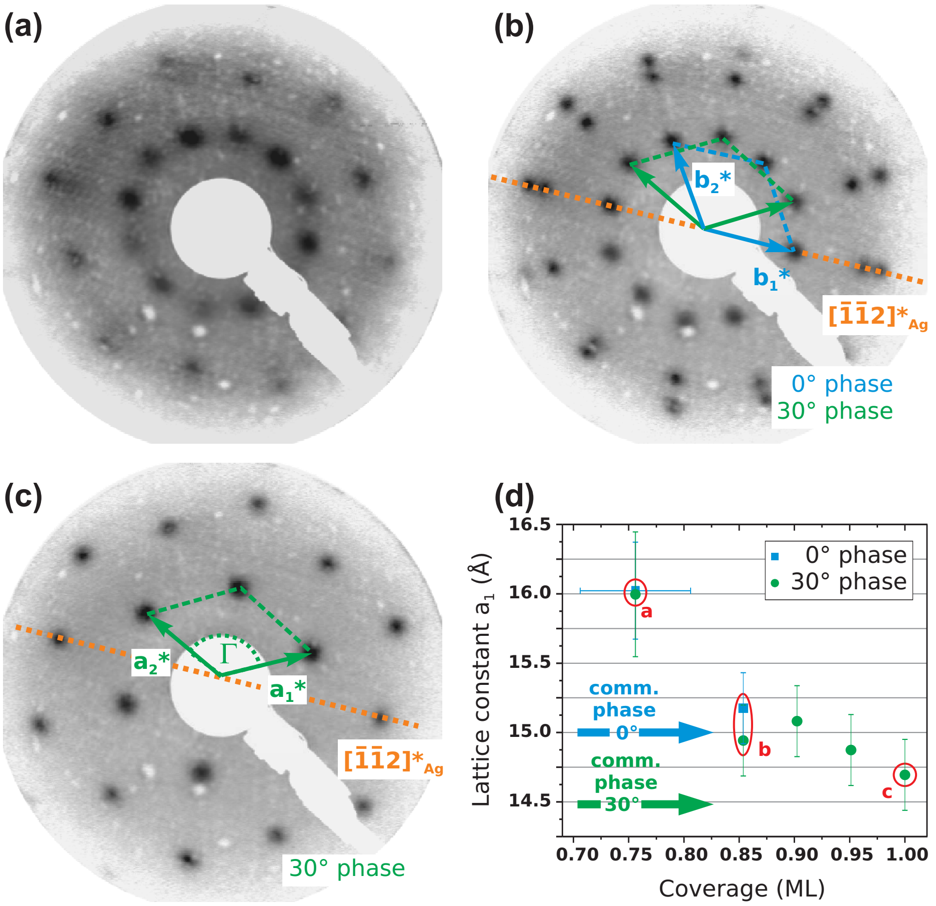

Figure 6.5: **(a)-(c)** LEED patterns for varying HBC coverage on Ag(111). All images have been recorded at $E_0 = 10.4\,\text{eV}$. **(d)** Observed HBC lattice constants in the 0° and 30° phase as a function of sample coverage. The data points belonging to the LEED patterns (a)-(c) are indicated as well as the lattice constants of the respective *commensurate* phases. The error bars for "coverage" are all identical.

indicate the absence of a sharp lattice constant which, in correspondence with the comparably large intermolecular distances, means a high mobility of all molecules on the surface. The situation probably corresponds well with the second panel of Fig. 5.5(d) and represents a case where lattice epitaxy has only little meaning at all. Then, with the strong orienting force of epitaxy eliminated, the observed orientations can be the product of very subtle effects that can neither be classified nor quantified here.

HBC on Au(111)

Four LEED patterns of highly ordered layers of HBC on Au(111) are shown in Figure 6.6. As for HBC on Ag, the patterns show different HBC coverages obtained stepwise on one and the same sample. The lattice constant data of all acquired data points are summarized in Fig. 6.6(e). The only apparent similarity between the LEED patterns of HBC on Ag and on Au is the exclusive occurrence of domain angles $\delta = (30 \pm 1)^\circ$ and $\delta = (0 \pm 1)^\circ$. On Ag, both phases appeared to be rather equal in terms of LEED spot intensity, i.e., relative surface coverage until the 0° phase vanished at $\approx 0.9\,\mathrm{ML}$. In contrast, the 0° orientation is dominant on Au(111) over the whole lattice constant range observed. As known from literature [35, 40, 80] and experimentally reproduced (not shown), one can even prepare samples completely without 30° domains. The key issue is whether the ML sample is prepared rather fast with a high deposition rate, rather slow with a low rate, or even with interrupts of several minutes as done here. Only in the latter cases, a coexistence between 0° and 30° domains can evolve.

When comparing the LEED patterns in Fig. 6.6(b) and (c), an interesting, yet barely visible effect is found. While the coverage increases by only 0.05 ML and the lattice constant of the 0° domains simultaneously decreases by $\approx 0.4\,\text{Å}$, a decrease of more than 1 Å is found for the 30° domains. This ratchet-like behavior can nicely be explained by the locking into the commensurate 30° phase which has an average lattice constant of 14.13 Å (Fig. 6.6(e)).

Here, an interesting aspect is given by the fact that no such ratchet effect is observed for the 0° domains which pass right through the respective lattice constant region of the commensurate 0° phase, keeping the dependency of a_1 on the coverage perfectly straight until a ML is reached. This fact can be explained only by the different energetic gains related to both commensurate phases (Fig. 6.3(b)). Any deviation from the "equilibrium" lattice constant (which is a function of the coverage) costs a certain amount of energy. Therefore, a non-equilibrium lattice constant or a distorted non-hexagonal lattice[1] will occur only if the gain V'_{inter} related to the new phase outweighs this penalty. This is obviously the case for the 30°, but not for the 0° orientation, which

---

[1] The commensurate structures on Au(111) are slightly distorted (Figs. 6.1(b) and 6.2(b)).

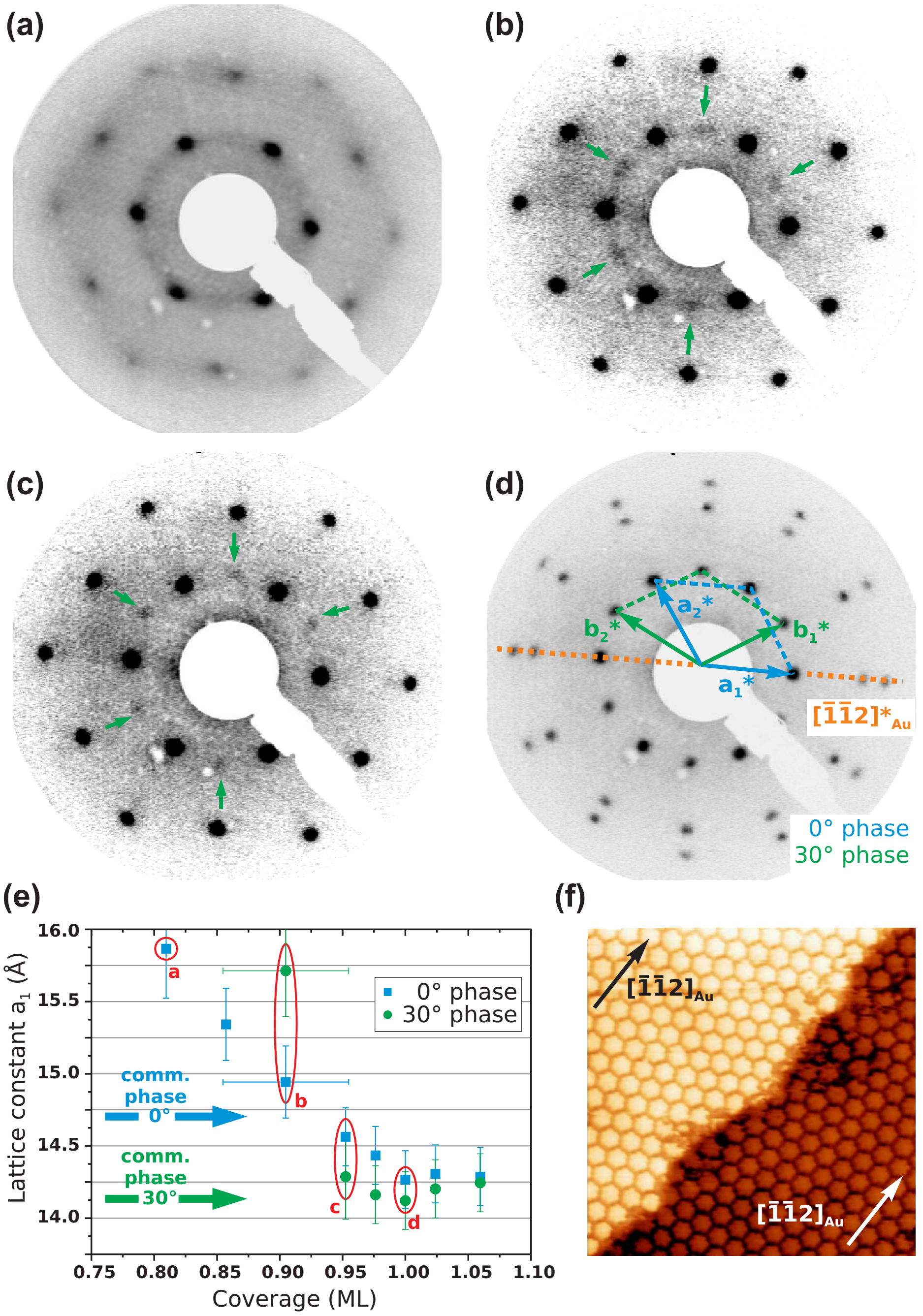

Figure 6.6: **(a)-(d)** LEED patterns for varying HBC coverage on Au(111). All images have been recorded at $E_0 = 10.4\,\mathrm{eV}$. The patterns in (b) and (c) are contrast-enhanced. Weak spots belonging to the 30° phase are marked by arrows. **(e)** Observed HBC lattice constants in the 0° and 30° phase as a function of sample coverage. The lattice constant of the 0° phase in (b) and (c) has *not* been derived from the contrast-enhanced images, but from low contrast versions showing much sharper spots. The data points belonging to the LEED patterns (a)-(d) are indicated in red. The thick blue and green arrows mark the lattice constants of the respective *commensurate* phases. The error bars for "coverage" are all identical. **(f)** STM image ($22 \times 22\,\mathrm{nm}^2$, $V = 0.8\,\mathrm{V}$, $I = 45\,\mathrm{pA}$) of a HBC ML on Au(111) exhibiting both, the 0° phase (upper Au terrace) and the 30° phase (lower Au terrace). Image by courtesy of Daniel Kasemann [103].

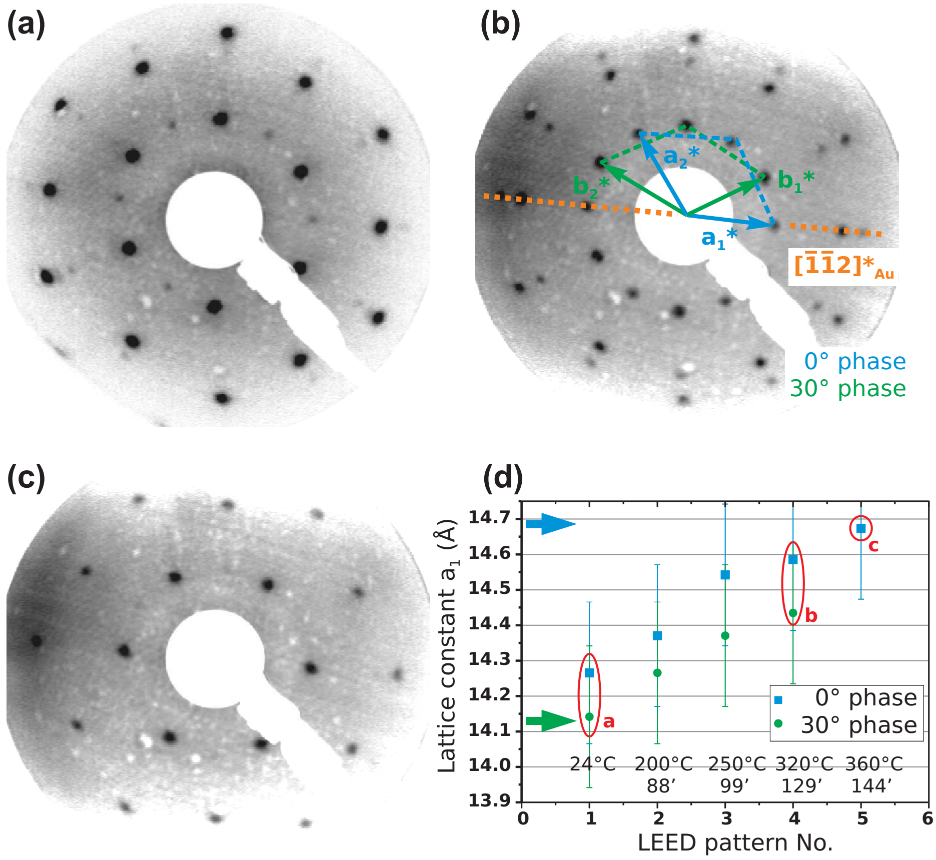

Figure 6.7: **(a)-(c)** LEED patterns obtained while annealing a ML HBC on Au(111) sample. All images have been recorded at $E_0 = 10.4\,\mathrm{eV}$. An overall increase of the lattice constants of $0°$ and $30°$ phase with increasing temperature and time is observed. The relative surface coverage of the phases shifts towards the $0°$ phase with increasing value for a_1. **(d)** Observed HBC lattice constants in the $0°$ and $30°$ phase. The data points belonging to the LEED patterns (a)-(c) are indicated in red. The total annealing time in minutes and the sample temperature reached are indicated at the bottom of the plot. The thick blue and green arrows mark the lattice constants of the respective commensurate phases.

is in complete accordance to the results of the potential energy calculation summarized in Fig. 6.3(b).

Another way to tune the HBC coverage and thus the equilibrium HBC lattice constant is a thermal desorption process performed by heating a ML sample while continuously monitoring the sample by LEED. An experiment complementary to the previously described evaporation experiments can be conducted that way. By maintaining a very low desorption rate, a precise tracking of the phase changes can be achieved. The outcome of the respective experiment shows a strong shift in the relative surface coverage from the initially dominant 30° phase to the 0° phase at larger lattice constants (Fig. 6.7) Again, this is completely consistent with the conclusions on the role of epitaxy drawn so far. It has to be pointed out that the increase in the lattice constant upon annealing is an irreversible process and not the expression of an increase in entropy. If the sample is cooled again, the initial lattice constant is *not* restored.

While the behavior of HBC on Au(111) discussed so far bears a good resemblance to the theoretical expectations, there is an observation which is at odds with theory: Only 0° domains exist on Au at low coverage and they still dominate the ML sample while the respective 0° domains vanish on Ag (which has successfully been explained by epitaxy). For the low coverage sample in Fig. 6.6(a) one can, again, safely assume the absence of lattice epitaxy. While no further explanation for the specific domain angles at low coverage could be given for HBC on Ag(111), the situation on Au(111) is substantially different. In the last part of this chapter, the role of the surface reconstruction of Au(111) will be investigated.

6.4 Influence of the Au(111) surface reconstruction

STM images of 0° HBC domains on Au(111) at two different coverages are compared in Figure 6.8. *Sample 1* is obtained by an evaporation time of 16 minutes (coverage 0.93 ± 0.05), while for *Sample 2* HBC was evaporated for another 2 minutes onto *Sample 1* (coverage 1.05 ± 0.05). Furthermore, *Sample 2* was subject to annealing at 120° C for 15 h. Both images are scaled to match the periodicity of the Au(111) surface reconstruction stripes. Remarkably,

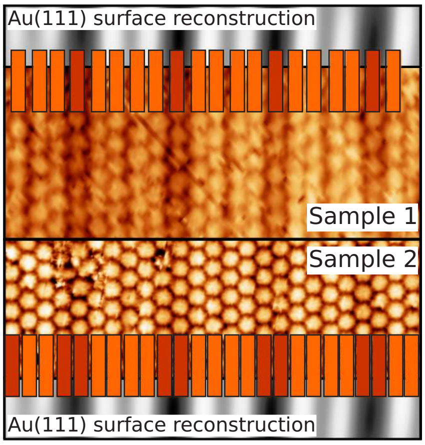

Figure 6.8: STM images exhibiting different ratios of surface reconstruction periodicity to HBC lattice constant after the evaporation of approx. 12.5 % more HBC molecules. Both images are scaled with respect to the surface reconstruction. *Sample 1*: coverage $(0.93 \pm 0.03)\,\mathrm{ML}$, *Sample 2*: coverage $(1.05 \pm 0.05)\,\mathrm{ML}$ plus annealing at $120°\,\mathrm{C}$. The orange and brown bars equal the HBC rows and provide a guide to the eye. In both images one finds an integer number of HBC lattice lines in one period of the surface reconstruction.

there is an *integer* number of HBC lattice lines in one period of the surface reconstruction in both images. At lower coverage (*Sample 1*), the five HBC lattice lines within one period are not equally spaced, meaning that there is no primitive HBC lattice at all. From *Sample 1* to *Sample 2* the coverage increases by ≈ 12.5 %, meaning a decrease of the lattice constant by ≈ 7 % from density arguments. One finds, however, exactly six HBC lattice lines per reconstruction period on *Sample 2*, corresponding to a lattice constant decrease of 17 %. This discrepancy indicates that the surface reconstruction is *no* appropriate scale here, as it obviously changes with coverage. Indeed, it has been observed before that the spacing of the Au-reconstruction can change upon deposition of organic molecules [104]. In the case of HBC on Au(111), the spacing between the reconstruction stripes increases with coverage, presumably adjusting to a multiple of the HBC lattice line spacing. A comparison to STM images of *Sample 2* taken prior to the annealing which show no such registry between HBC lattice and reconstruction stripes (not shown) indicates that the coherence of substrate and adsorbate periodicities indeed represents an energetic optimum. The annealing provides the thermal energy necessary for a rearrangement of the Au atoms.

It is proposed that the distinct orientation the 0° domains is exclusively caused by the interaction with the Au(111) surface reconstruction stripes. Thus, it can be seen as directly related to the observation of an *electronic superlattice* on reconstructed Au(111) [105]. The influence of the superlattice, however, only leads to visible results if other, stronger ordering mechanisms like commensurate lattice epitaxy are ruled out as it is the case here. This behavior is *not* in contradiction to the discussion of epitaxy in Chapter 4. It basically means a line-on-line growth of HBC on (05) or (06) lines of the large unit cell of the reconstructed Au(111) surface.[2] Concluding, the reconstruction represents a mechanism of orientation that is *independent of the lattice constant* and thus optimal for the growth under a repulsive potential as observed for HBC on Au(111). This explains the observed dominance of the $\delta = 0°$ domains.

6.5 Conclusion

By a detailed investigation of the ordered phases of HBC on Ag(111) and Au(111), it was possible to shed some light on the role of the molecule-substrate interaction in both systems. It turned out that on both surfaces a transition between ordered phases of HBC can be observed. On Ag(111), all 0° phase domains turn into 30° domains above a coverage of 0.85 ML. On Au, in contrast, only 0° phase domains exist below 0.85 ML, while a coexistence of 0° and 30° phases is observed at higher coverage. These findings can be explained

---

[2] For an unchanged reconstruction this would be a $22 \times \sqrt{3}$ supercell.

by the influence of commensurate and POL epitaxy. During the layer growth, the HBC lattice constant passes through regions where epitaxy is favorable, as well as through regions without good registry to the substrate lattice. As long as the surface mobility is high enough and / or there is enough time, the films will thus adopt the most preferential orientation. An important aspect is the finding that a purely geometric discussion is not sufficient to explain the experimental results. The energetic gain V'_{inter} of a commensurate or POL phase depends strongly on the orientation ζ of the molecules. The two phases of HBC, 0° and 30°, are by no means equal in energy, with the 0° phase on the short end. Hence, it is even more surprising that HBC films on Au(111) are dominated by 0° domains. In the last part of the chapter, an explanation for this fact was given that involved the surface reconstruction. Although no potential energy calculations can be performed on such a large scale, there is experimental evidence that a registry between molecular rows and the reconstruction stripes is energetically favorable.

To get the right perspective, it is important to mention a specific shortcoming of the molecule-substrate force-field calculations performed. The values for the energetic gain V'_{inter} reported here are certainly not wrong *in comparison to each other*, in fact there is a good agreement with the experiments, but they might not be fully on scale. This should mainly be attributed to the fact that the energetic gain is calculated at an equilibrium molecule-substrate distance. This separation corresponds to a minimum in the interface potential V_{inter}, i.e., an equilibrium between London and Pauli forces. Compared to thermal desorption spectroscopy results, the UFF force field substantially underestimates the attractive potential (1.5 eV to 3.5 eV, compare Section 3.2.2). Hence, the calculated equilibrium distance is probably too large and the corrugation of the substrate's surface consequently too small. Thus, the values V'_{inter} for different epitaxial phases are all too small by a *common* factor. Knowing either the magnitude of the total binding energy *or* the equilibrium distance, the calculations of the site dependent energetic gain would probably yield more accurate absolute results. For reasons of consistency of the force-field method used, such a route was, however, not taken. After all, the precise absolute scaling of the energy values in Fig. 6.3 plays almost no role for the argumentation in this chapter.

7 Organic Heterosystems of PTCDA and HBC on Au(111)

The importance of controlling molecular growth on the Å-scale has already been motivated in the Introduction. The growth of highly ordered organic-organic heterosystems is a crucial step towards devices that either benefit from the superior charge transport properties in single crystalline systems or even employ characteristics properties of single molecules in molecular electronics. The relevance of systems including several organic compounds is immediately clear when considering state-of-the-art organic devices like OLEDs which easily contain more than five different organic species [106]. One important aspect of planar stacks is the good charge transport in the direction of the stack [107]. The front orbitals of aromatic molecules are usually π *orbitals, and the geometry in a stack means an optimal overlap between* π *orbitals of molecules that face each other. In this chapter, the structural properties of the model system PTCDA on HBC on Au(111) are investigated, while the aim of the next chapter is to generalize the findings made.*

A first in-depth study of the ordering in organic heterolayers has been presented by Mannsfeld et al. [39] who identified a phase of PTCDA on HBC on graphite to be governed by the general ordering principle of LOL epitaxy. Since then, several other organic-on-organic systems were found to exhibit LOL epitaxial growth [42, 108, 109]. However, the potential energy of the interface, i.e., the driving force behind the ordering was either not discussed at all [108, 109], or only the mere existence of an energetic gain was reported [39] (which is a direct consequence of Eq. 4.9). While the nature of epitaxial growth is covered by the considerations in Chapter 4, only the comparison to the experiment can show its practical relevance. Only then the ideas can be transferred to other systems and predictive power can be gained. The model system investigated for this purpose is PTCDA on HBC on Au(111). A purely descriptive report about the existence of an ordered phase of this system was given by Sellam et al. [40]. In this chapter, especially the tunable HBC lattice shall be exploited to study its influence on the heterosystem. It will show that none of the techniques LEED, STM, and potential energy calculation alone is sufficient to understand the properties of such organic-organic heterolayers. Only a combination of all three techniques can lead to a correct picture of the system investigated.

7.1 PTCDA on Au(111) revisited

As a matter of fact, the growth of PTCDA has been studied on almost any inorganic surface imaginable, including Au(111) [29, 92]. There is, nevertheless, a strong motivation to reinvestigate the system PTCDA on Au(111) in the context of this work. Compared to the case of PTCDA on Ag(111), where PTCDA is chemisorbed and a single, commensurate phase is observed, the situation is more delicate on Au. Up to five inequivalent orientations of the PTCDA lattice have been observed on Au and for three of them, POL growth was concluded [92]. The relative coverage of each phase is found to depend on the preparation procedure. As the analysis of the growth of PTCDA on HBC in this chapter is partially conducted by LEED, it is not always possible to verify whether an observed lattice belongs indeed to PTCDA *on HBC* or

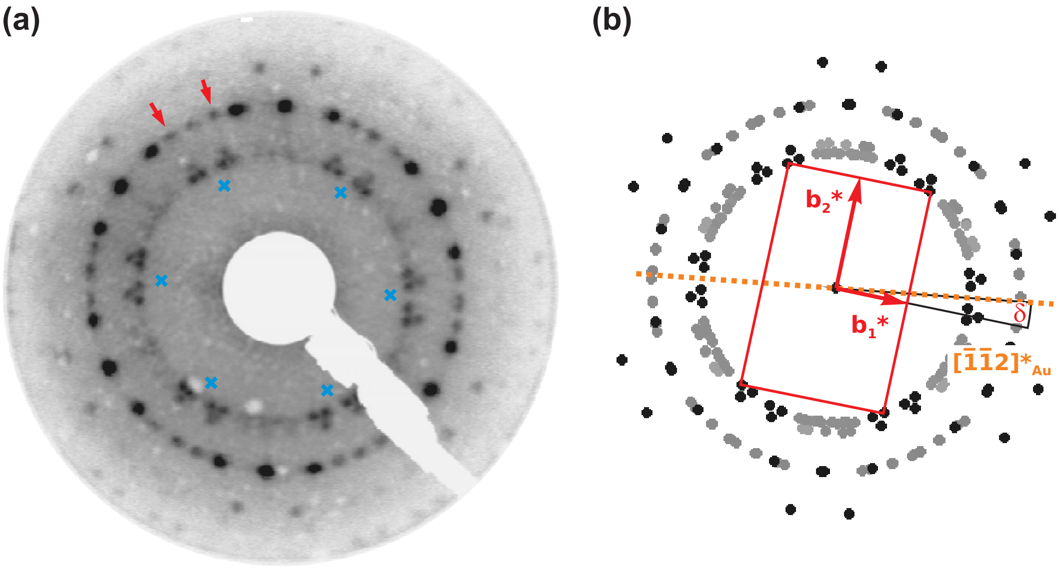

Figure 7.1: **(a)** LEED pattern of a PTCDA ML on Au(111) ($E_0 = 10.4\,\mathrm{eV}$). The dominant spots belong to Phase **A** PTCDA, while also Phase **B1** and **B2** spots can be assigned [92]. In contrast to Ref. 92, a fourth PTCDA phase ("**C**") contributes significantly (red arrows). To guide the eye in a comparison with LEED patterns of PTCDA on HBC, the theoretical positions of all first-order spots of HBC are marked by blue crosses. **(b)** LEED simulation of the pattern in (a). Phase **A** spots are black while **B**$_1$, **B**$_2$ and **C** spots are grey in accordance to the intensities in the actual LEED pattern. All spots with a low kinematic intensity have been omitted (see text). The reciprocal Phase **A** unit cell is indicated in red ($b_1 = 19.2\,\text{Å}$, $b_2 = 12.3\,\text{Å}$, $\delta = 7.5°$).

whether it belongs to PTCDA directly *on Au(111)*. Thus, an overview over the growth of PTCDA on Au(111) is not only beneficial for the reader, but a key element in the interpretation of the structures found in the heterosystem.

The LEED pattern of a ML of PTCDA on Au(111) is shown in Fig. 7.1(a) and the respective kinematic LEED simulation in Fig. 7.1(b). As it is the more comprehensive study, Ref. 92 will be used instead of Ref. 29 to identify and name the different phases of PTCDA that contribute to the LEED pattern. It is intentionally avoided to present a full-fledged revision of all phases of PTCDA on Au(111) here. A summary of the lattice constants and domain orientations is given in Table 7.1.

The dominant spots in Fig. 7.1(a) stem from the non-equilibrium phase **A**, while the contribution of the equilibrium domains $\mathbf{B}_1$ and $\mathbf{B}_2$ is comparably weak. A surprising result, in the context of Ref. 92, is the considerable intensity in the LEED spots marked by red arrows. They are (21) spots belonging to a PTCDA phase which will be called **C** here, as it is labeled "weak" in the respective publication only. There, it appeared at the detection limit of the SPA-LEED-apparatus used. The fact that it is still visible here indicates that under certain conditions, the growth of **C**-domains of PTCDA on Au(111) is quite probable. In order to determine the lattice constants as accurate as possible, the raw data in Ref. 92 was analyzed insted of Fig. 7.1(a). The values are $a_1 = (19.3 \pm 0.1)\,\text{Å}$ and $a_2 = (12.2 \pm 0.1)\,\text{Å}$. Please note the additional 5% scaling error mentioned in Ref. 92. Phase **C** turns out to be a phase close to POL coincidence, which grows under a domain angle $\delta = 30°$ between $\mathbf{b}_2$ and the $(\bar{1}\bar{1}2)_{Au}$ direction. The epitaxial matrix was determined to

$$\mathbf{C}_\mathbf{C} = \begin{pmatrix} 7.99 & -4.11 \\ -0.11 & 4.33 \end{pmatrix} \tag{7.1}$$

relative to the Au(111) lattice as described in Fig. 2.8 of Section 2.4.4.

In Fig. 7.1(b), the dominant Phase **A** spots are indicated in black, while all spots from the Phases $\mathbf{B}_1$, $\mathbf{B}_2$ and **C** are plotted in gray, mimicking the actual intensity distribution in Fig. 7.1(a). Spots of all phases which are weak in a

Table 7.1: Lattice data for PTCDA on Au(111) from Ref. 92. The phases named **C** and **D** are reported but not discussed in the original paper. All values in square brackets are thus derived from the raw data of Ref. 92 with an error of ±0.1 Å.

Structure	δ(°)	b_1(Å)	b_2(Å)
A	7.5(3)	19.2(2)	12.3(1)
$\mathbf{B}_1$	39.5(5)	19.2(2)	12.1(1)
$\mathbf{B}_1$	37.0(5)	19.2(2)	12.1(1)
C	[30]	[19.3]	[12.2]
D	[14.3]	[19.3]	[12.4]

kinematic LEED simulation[1] are omitted from the Figure for clarity. It is thus a mixture of a kinematic and a geometric LEED simulation which represents a convenient way to present simulated LEED patterns containing phases of different intensity. Only the reciprocal unit cell belonging to the Phase **A** domains is indicated.

7.2 LEED and STM on PTCDA|HBC|Au(111) samples

One aspect of this chapter is to study the influence of the HBC lattice on the growth of a PTCDA ML on top. Hence, three similar experiments have been performed, differing in the configuration of the initial HBC layer. In two cases, HBC samples were used that exhibited 0° domains only, thus simplifying the expected LEED patterns. In addition, the growth of PTCDA on a mixed domain sample with 0° and 30° domains was investigated.

The quantitative analysis of the LEED patterns was performed as described in Section 2.3. In the following discussion of the heterosystem PTCDA on HBC on Au(111), a perfect hexagonal symmetry of the HBC lattice as well as a rectangular PTCDA unit cell is assumed. There is, at first hand, no reason to assume such a perfect symmetry. However, discussing deviations from these assumptions would mean to argue within the error bars of the LEED measurements, thus adding too much complexity to the problem without getting reliable results. The whole system is now describable by a set of four numbers: The lattice constant a_1 of HBC, the PTCDA lattice constants b_1 and b_2, and the domain angle δ. The definition of δ in real and reciprocal space is given by

$$\delta = \angle(\mathbf{a}_2, \mathbf{b}_2) = \angle(\mathbf{a}_1^*, \mathbf{b}_1^*).$$

7.2.1 A “compact” HBC layer substrate

Two of the three experiments mentioned have been summarized in Fig. 7.2. The LEED pattern of PTCDA on a HBC ML with $a_1 = 14.5\,\text{Å}$ (Fig. 7.2(a)) shows a remarkable *decrease* in complexity if compared to the growth of PTCDA directly on Au (Fig. 7.1). This indicates a clear effect of the HBC layer. The LEED pattern is describable by the HBC spots and a single PTCDA phase with $b_1 = (19.2 \pm 0.2)\,\text{Å}$, $b_2 = (12.45 \pm 0.2)\,\text{Å}$ and $\delta = (0 \pm 1)^\circ$ that evidently corresponds to the growth of PTCDA on HBC as described in Ref. 40. It will be referred to as PTCDA Phase **I** from now on. Figure 7.2(b) shows a corresponding kinematic LEED simulation including the reciprocal lattices of PTCDA (red) and HBC (blue).

---

[1] For example the (10) and (01) spots which are suppressed due to the p2gg symmetry of the PTCDA lattice [29].

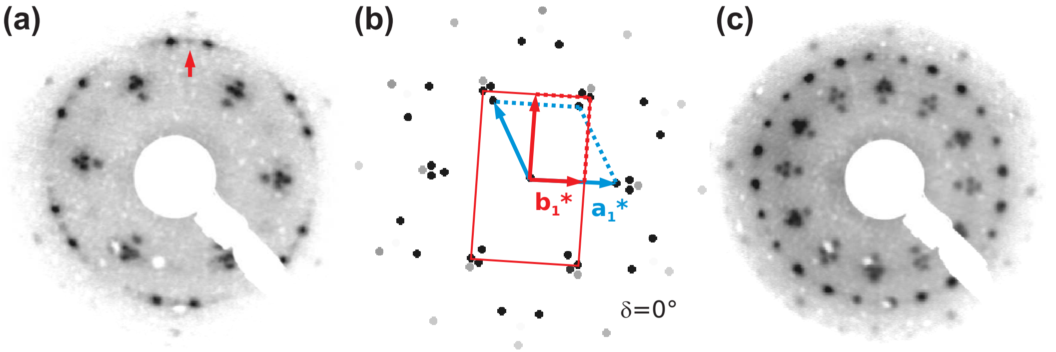

Figure 7.2: **(a)** LEED pattern of PTCDA|HBC|Au(111) ($E_0 = 10.4\,\text{eV}$). The red arrow marks a spot that can be associated with the PTCDA Phase **A** directly on Au(111). Apart from that, all spots belong either to HBC or to Phase **I** PTCDA. **(b)** Kinematic LEED simulation of Phase **I** PTCDA on HBC. The reciprocal unit cells are indicated in red (PTCDA) and blue (HBC). **(c)** LEED pattern of a ML PTCDA on a HBC|Au(111) substrate containing 0° and 30° HBC domains ($E_0 = 10.4\,\text{eV}$). The whole pattern is explicable by Phase **I** PTCDA growing on both types of HBC domains.

A remarkable effect is found when comparing the HBC lattice constant a_1 prior and after the deposition of PTCDA. The value of a_1 decreases from initially 14.5 Å to 14.0 Å. This compression of the HBC lattice beyond the smallest value of a_1 observed in a pure HBC layer (14.2 Å) can be attributed to a small amount of PTCDA diffusing into the first layer directly on Au(111). An evidence for this scenario is given by the faint LEED spot marked by a red arrow in Fig. 7.2(a) (and its symmetry equivalents). While this spot cannot be explained by the simulation presented in (b), its position perfectly coincides with that of the intense (21) spot of the Phase **A** directly on Au(111) (Fig. 7.1). If this assignment is correct, the occurrence of Phase **A** PTCDA on a PTCDA|HBC|Au(111) sample indicates the growth of small PTCDA *domains* in the first layer directly on gold, i.e., the diffusion process does not result in a random distribution of PTCDA molecules. The low intensity of the (21) spots coincides with the PTCDA coverage of 0.07 ML directly on Au(111) as derived from the compression of the HBC lattice.

This interpretation is also supported by the LEED pattern of a PTCDA ML on a mixed-HBC-domain sample (0° and 30° domains, Fig. 7.2(c)). Here, the initial lattice constants of both HBC phases were much closer to the value of the compressed layer. As expected, no hint of the Phase **A** of PTCDA is visible in the LEED pattern which is characterized by the HBC first order spots and the PTCDA Phase **I** spots. As a first conclusion, PTCDA grows on 0° and 30° domains in a similar fashion. Although this is not too surprising, it has to be seen in contrast to the growth of QT on HBC, which occurs on 0° domains only [42].

7.2.2 A “loosely packed” HBC layer substrate

The growth of PTCDA on rather compact HBC layers will now be complemented by a study of PTCDA on rather *loosely* packed HBC. A nominal ML of PTCDA is deposited on a HBC layer consisting of 0° domains with a lattice constant of $a_1 = 14.75\,\text{Å}$. The respective LEED pattern in Figure 7.3(a) is more complex than its equivalent in Fig. 7.2(a), although the spots of highest intensity are similar. The LEED simulation in Fig. 7.3(b) is again depicted as a mix of kinematic and geometric LEED information. The Phase **I** spots that dominate the LEED pattern appear in black while spots belonging to other phases are grey. The three different reciprocal PTCDA lattices used in the simulation are displayed separately in Figs. 7.3(c)-(e).

In the light of the previous results, a significant amount of PTCDA is expected to diffuse in the loosely packed HBC layer. The LEED spots associable with Phase **A** PTCDA domains directly on Au(111) (Fig. 7.3(d)) are indeed of considerable intensity. The decrease of the HBC lattice constant to $a_1 = (13.95 \pm 0.1)\,\text{Å}$ upon deposition of PTCDA suggests a coverage of $\approx 0.11\,\text{ML}$ of PTCDA in the first layer on Au. In addition to the Phase **A** spot marked red in Fig. 7.2(a), two further spots belonging to this phase appear in Fig. 7.3(a) (red arrows). The third phase of PTCDA found in Fig. 7.3(a) was not present on the previously discussed PTCDA|HBC|Au(111) samples at all. It is characterized by spots is a triangular arrangement in the inner ring (green square) and two additional spots in the outer ring (green arrows). The lattice parameters of this Phase are determined to $b_1 = (19.5 \pm 0.3)\,\text{Å}$, $b_2 = (12.2 \pm 0.2)\,\text{Å}$ and $\delta = (30 \pm 1)°$.

At present, it is not possible to clearly identify this third phase. On one hand it may result from PTCDA molecules that grow directly on Au(111). Its lattice constants and domain angle correspond, within the error interval, to the values of Phase **C** PTCDA on Au(111) as described in Section 7.1. Under this assumption, there is, however, no obvious reason for the comparably strong intensity of the respective LEED spots in Fig. 7.3(a). The “triangle” of spots in the green box even dwarfs the respective Phase **C** spots for a pure PTCDA ML in Fig. 7.1(a), although the PTCDA coverage directly on Au(111) is only $\approx 0.11\,\text{ML}$ in Fig. 7.3. On the other hand, the spots could be related to a second phase of PTCDA growing on HBC. This assumption could explain the spot intensity and would imply that there *is* an influence of the initial HBC lattice constant on the growth of PTCDA. An argument in favor of this second interpretation will be provided in Section 7.3. Notwithstanding the lack of final clarification and its similarity to Phase **C**, the respective Phase of PTCDA will be denoted as PTCDA Phase **II**, assuming that it indeed grows on HBC.

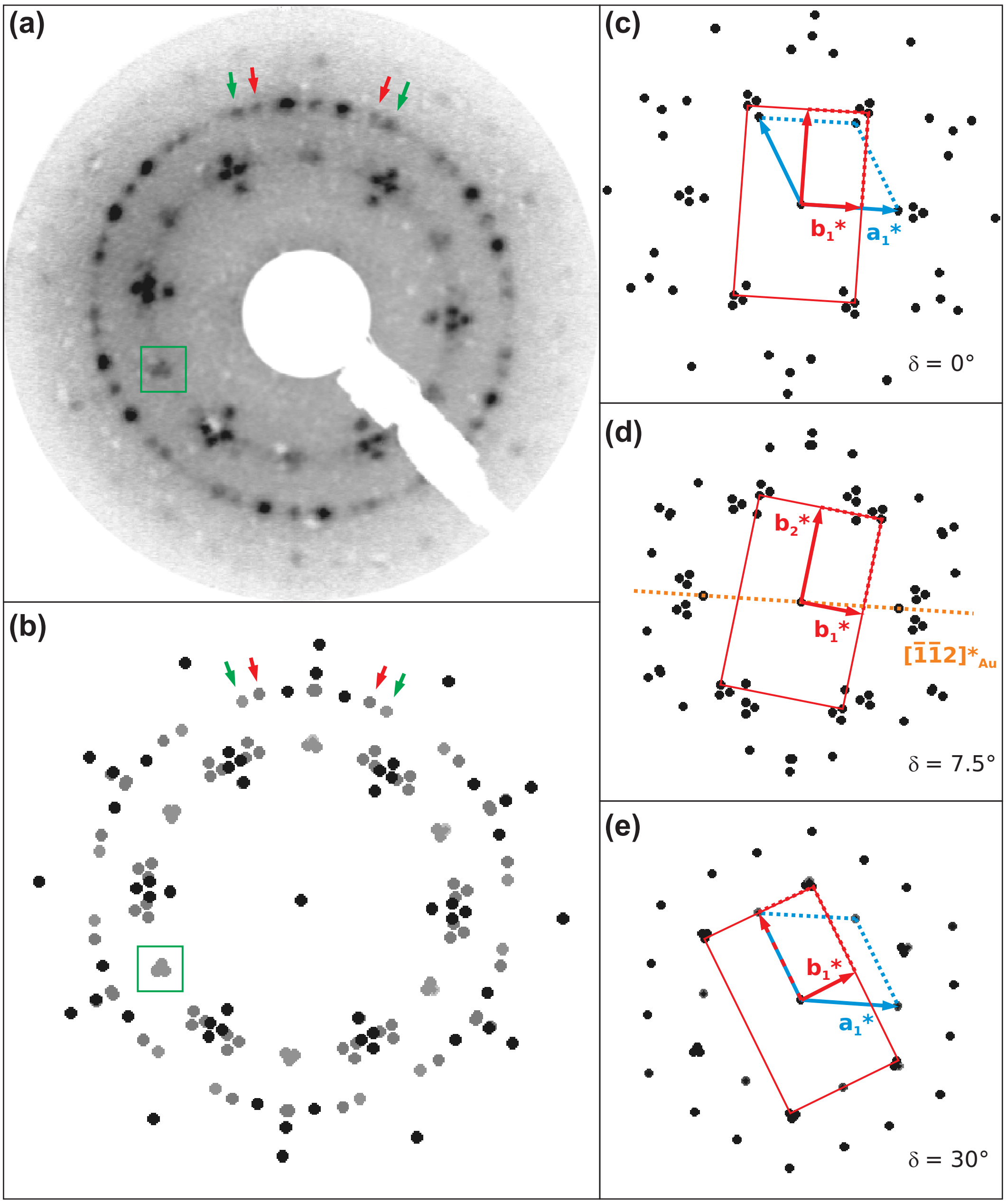

Figure 7.3: **(a)** LEED pattern of PTCDA|HBC|Au(111) ($E_0 = 10.4\,\mathrm{eV}$). The pattern is dominated by Phase **I** PTCDA spots. Two other phases have been found to contribute: Spots belonging to Phase **A** are marked by red arrows, while green marks indicate Phase **II** spots. **(b)** LEED simulation of the pattern in (a). Phase **I** spots are black while Phase **A** and **II** spots are grey in accordance to the intensities in the actual LEED pattern. All spots with a low kinematic intensity have been omitted (see text). **(c)-(e)** LEED simulations of all phases contributing to the observed contrast. (c): Phase **I**, (d): Phase **A**, (e): Phase **II**.

7.2.3 Summary of LEED results

Summarizing the results of all LEED investigations discussed so far, several facts are evident:

- Independent of the initial HBC lattice constant which has been selected by adjusting the coverage, the HBC lattice constant decreases to a value of $a_1 \approx 14.0\,\text{Å}$ upon deposition of PTCDA.
- The Au(111) surface freed in this process is occupied by PTCDA Phase **A** domains. The further occurrence of Phase **C** is very unlikely but cannot be completely excluded at present.
- The major part of all PTCDA molecules deposited grows on HBC in a phase called Phase **I**. This phase corresponds to the growth of PTCDA on HBC described in Ref. 40.
- An additional phase of PTCDA is observed in case of a loosely packed initial HBC sample. Although its lattice constant and domain angle are similar to Phase **C** of PTCDA on Au(111), it very likely grows on HBC and is therefore called Phase **II**.
- Despite the compression of the HBC layer to a lattice constant of $a_1 \approx 14.0\,\text{Å}$, the initial configuration of the pure HBC layer still influences the growth of PTCDA. This effect can probably be attributed to the higher mobility of HBC in the loosely packed layer.

The results of a quantitative LEED analysis are summarized in Table 7.2. Independent of the initial coverage, the resulting heterosystems are quite similar

Table 7.2: Lattice constants found for the system PTCDA|HBC|Au(111). Listed are the Figure containing the respective LEED pattern, values of the HBC lattice constant a_1 prior and after the deposition of PTCDA, the fraction of the Au(111) surface directly covered with PTCDA molecules (see text), and the lattice constants of the Phase **I** PTCDA domains on HBC. All lattice constants have an error of $\pm 0.2\,\text{Å}$ and are rounded to 0.05 Å. The $30°$ phase values of HBC are marked by an asterisk.

Figure	a_1 (Å) (initial)	a_1 (Å) (after depos.)	1^{st} layer cov. PTCDA (ML)	b_1 (Å)	b_2 (Å)
7.2(a)	14.5	14.0	0.07	19.2	12.45
7.2(c)	14.3	14.0	0.02	19.5	12.5
	14.05 *	14.1 *	0.02	19.55	12.55
7.3(a)	14.75	13.95	0.11	19.4	12.6

in terms of the HBC and the PTCDA Phase **I** lattice constants. An epitaxial growth is quite probable and will be discussed in detail in Section 7.3. The STM investigations described in the next part will now compensate a general shortcoming of a LEED analysis: In a LEED pattern there is little, if any, information whether the observed lattices form a vertical heterosystem, or whether they belong to independent domains on different lateral positions. In the STM contrast, different layers can be distinguished even if they are on top of each other (Section 2.2).

7.2.4 STM results

STM images represent iso-conductance surfaces of the scanned area. As the (local) conductance path *through* an organic multilayer system is mainly coupled to overlapping π-systems, it is only consequential that the conductance holds information about both participating layers.

A STM image of a Phase **I** PTCDA domain on a 0° HBC domain on Au(111) is shown in Figure 7.4(a). Although the contrast resulting from both layers is not clear at all, an identification is immediately possible in the FFT of the respective image (Fig. 7.4(b)). As discussed in Section 3.1, the FFT is a representation of reciprocal space and thus similar to a LEED pattern. Here, the key difference is that each LEED pattern discussed in this chapter simultaneously shows the reciprocal space information for *all* possible rotational domains of the system PTCDA|HBC|Au(111). Hence, the six-fold symmetry of the HBC substrate is reflected in the LEED patterns while the FFT represents the reciprocal space of *one* orientation only. By a comparison to the

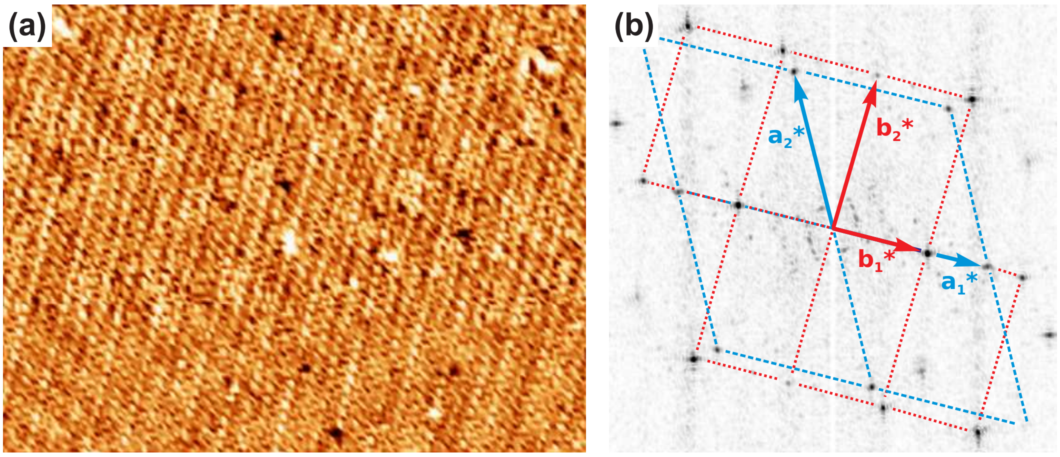

Figure 7.4: **(a)** STM image ($75 \times 55\,\mathrm{nm}^2$, V = 0.4 V, I = 95 pA) of a PTCDA Phase **I** ML domain on a HBC 0° ML domain on Au(111). The Au(111) surface reconstruction is faintly visible. **(b)** FFT of the image in (a) exhibiting clear spots that can be assigned to either the PTCDA or the HBC lattice. The reciprocal lattice vectors are indicated in red (PTCDA) and blue (HBC).

LEED simulation in Fig. 7.2, one can clearly identify the reciprocal lattices of PTCDA and HBC in Figure 7.4(b). In contrast to the LEED pattern, the $(10)_{PTCDA}$ and $(01)_{PTCDA}$ spots are visible in the FFT.

Precise information about the *absolute* scaling of both lattices cannot be obtained from the STM due to image distortions and drift. A comparison of the *relative* sizes of both lattices can, however, be drawn. Here, especially the *parallel* reciprocal vectors $\mathbf{a}_1^*$ and $\mathbf{b}_1^*$ are suitable as both are affected in an identical fashion by any image distortion. The ratio of b_1/a_1 is determined to be 1.40 ± 0.02 which nicely fits to the values in Tab. 7.2 where b_1/a_1 ranges from 1.37 to 1.39.

While also domains of PTCDA Phase **A** directly on Au(111) have been found in STM images, no evidence of Phase **II** PTCDA could be found. This may mainly be due to the rare occurrence of this phase as concluded from the low intensity of the corresponding LEED spots. It also means that the uncertainty remains whether Phase **II** grows on HBC or directly on Au(111).

A second *type* of PTCDA on HBC on Au(111) samples shall be mentioned here as well. It is not prepared in the straight-forward manner usually used, but its creation is based on a sample of inversed stacking sequence. The properties of such HBC|PTCDA|Au(111) samples will be described in Section 7.4. Under a light annealing, a *reversal* of the stacking sequence is observed for these systems. Surprisingly, the resulting samples are by no means disordered but also show highly ordered domains in vertical heterosystems.

Figure 7.5(a) shows a STM image of such an inverted system exhibiting a PTCDA domain on top of a 0° HBC domain. In addition to the FFT analysis of both lattices, a FFT filtering has been applied to the STM image by selecting either the spots belonging to HBC or the spots belonging to PTCDA. The results of an inverse FFT of the filtered patterns are shown in Fig. 7.5(c) for PTCDA and Fig. 7.5(d) for HBC. The Fourier filtering allows an excellent separation of the lattice information contained in the original image, thus revealing the composition of the heterosystem. The analysis of the FFT in Fig. 7.5(b) yields a domain angle $\delta = (7.3 \pm 1)^\circ$ between $\mathbf{a}_1^*$ and $\mathbf{b}_1^*$. This value does neither correspond to Phase **I** ($\delta = 0^\circ$) nor to Phase **II** ($\delta = 30^\circ$) and consequently represents a third Phase of PTCDA on HBC, called Phase **III**.

The question, why the respective phase was not found in the LEED analysis reported above, can be answered: With a domain angle of $\delta = 7.3^\circ$ with respect to a 0° HBC domain, the domain angle of Phase **III** with respect to the Au(111) lattice is $\delta = 7.3^\circ$ as well. Phase **III** and Phase **A** have virtually identical domain orientations and one cannot distinguish both phases at the resolution provided by the LEED instrument used. A certain fraction of the Phase **A** spot intensity in Figs. 7.2 and 7.3 may, in fact, stem from PTCDA Phase **III** domains. Furthermore, it is not unlikely that the different preparation procedures of both types of samples (normal samples vs. layer

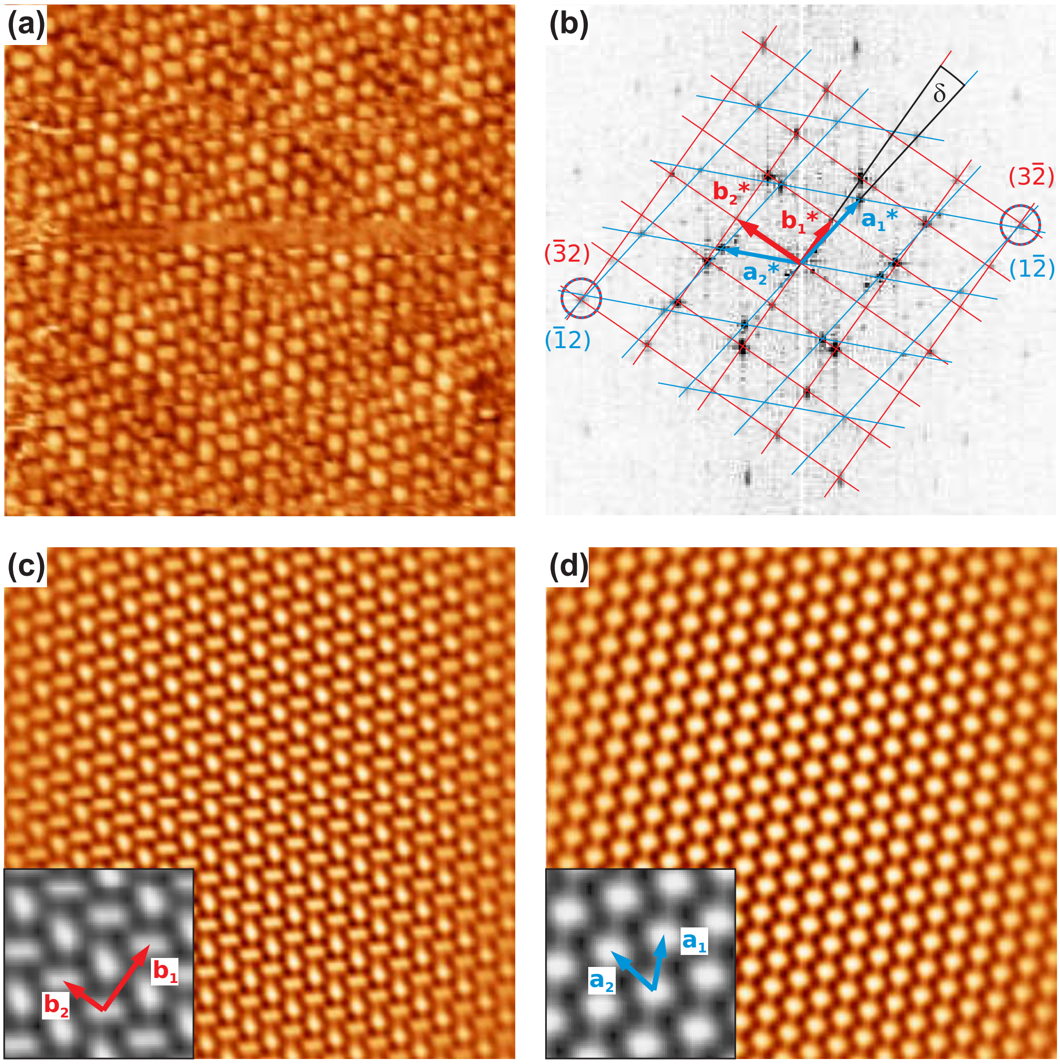

Figure 7.5: **(a)** STM image ($25 \times 25\,\mathrm{nm}^2$, V = 0.42 V, I = 95 pA) of a PTCDA Phase **III** ML domain on a HBC 0° ML domain on Au(111). **(b)** FFT of the image in (a), exhibiting numerous spots that can be assigned to either the PTCDA or the HBC lattice. The reciprocal lattice vectors are indicated in red (PTCDA) and blue (HBC). The domain angle of PTCDA is found to be $\delta = (7.3 \pm 1)^\circ$. There is a coincidence between the $(\bar{1}2)_{HBC}$ and $(3\bar{2})_{PTCDA}$ reciprocal lattice points marked by a circle. **(c)** and **(d)** show the results of an inverse FFT of a filtered version of (b). Either the spots belonging to PTCDA or to HBC have been selected for the inverse transformation. The resulting images show consequently the STM contrast of one molecular species only, thus "decoupling" the complex contrast in (a).

sequence inversion) favor different phases.

A feature of the FFT in Fig. 7.5(b) that demands attention is the coincidence between the reciprocal $(1\bar{2})$ and $(3\bar{2})$ lattice points of HBC and PTCDA marked by a red-blue circle in (b). Recalling the discussion of epitaxy in Chapter 4, such a coincidence of higher-order lattice points is a clear sign for the occurrence of line-on-line epitaxy. The following section is therefore dedicated to an analysis of the epitaxial relations in all phases of PTCDA found on HBC.

7.3 Epitaxial relations in the system PTCDA|HBC|Au(111)

7.3.1 Geometrical analysis of epitaxy

The identification of epitaxial relations is preferably performed in the reciprocal lattices of both layers involved, i.e., PTCDA and HBC. The influence of the Au(111) substrate beneath can safely assumed to be insignificant. This situation is different from the case of PTCDA on HBC on graphite, where LOL epitaxy was found for the first time [39]. While HBC forms a commensurate overlayer on graphite, a HBC lattice with $a_1 \approx 14.0\,\text{Å}$ and $\delta = 0°$ grows incommensurate on Au(111) (Fig. 6.2 in Chapter 6). Hence, there is no fixed relation between the lattice of Au(111) and the lattices of PTCDA and HBC in any direction. The epitaxial relations of all phases of PTCDA on HBC will now be discussed one by one.

- **Phase I**: The domain angle $\delta = (0 \pm 1)°$ of Phase **I** is almost identical to the value of 1.1° found by Mannsfeld et al. for the system PTCDA on HBC on graphite [39]. There, a coincidence of the $(61)_{HBC}$ and $(91)_{PTCDA}$ reciprocal lattice points was found and related to the graphitic structure of HBC. It was further assumed that this result could be generalized for other systems. It thus appears to be reasonable to expect an identical LOL relation here. The ratio b_1/a_1 between PTCDA and HBC lattice would be ≈ 1.42 in case of a (61)(91) LOL epitaxy,[2] while values from 1.37 to 1.39 have been found in the LEED analysis. Additionally, the clear splitting of the eye-catching triangle of PTCDA-spots in Figure 7.2 is in contradiction to the assumption of a (61)(91) LOL relation. Nevertheless, there are LOL coefficients that fit the results within the accuracy needed. A coincidence between $(50)_{HBC}$ and $(80)_{PTCDA}$ points is characterized by a perfect alignment between a HBC lattice vector $\mathbf{a}_2$ and the PTCDA lattice vector $\mathbf{b}_2$ and by a ration $b_1/a_1 = 1.385$. Both values are in agreement with the LEED results.

---

[2] This compact notation of LOL epitaxial phases will be used from now on.

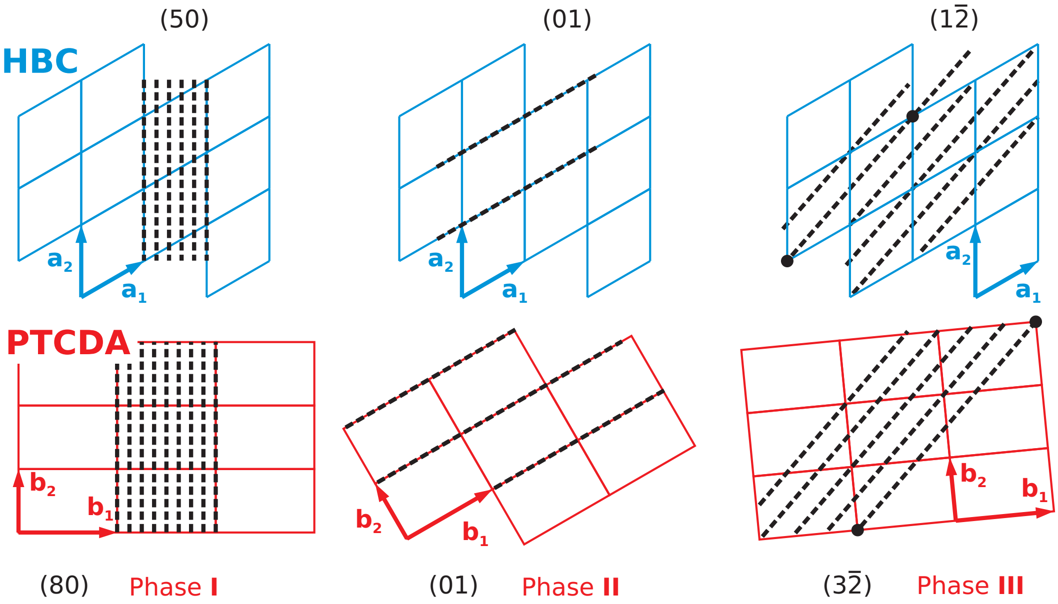

Figure 7.6: Scheme of the coincident lattice lines of HBC and PTCDA for the three phases of PTCDA found in the system PTCDA|HBC|Au(111). The spacing between the lines as well as their orientation have to be identical for HBC and PTCDA to fulfill the requirements of LOL epitaxy. Consequently, the PTCDA lattice adopts different domain angles in the three phases.

- **Phase II**: It was reasoned that the LEED spots belonging to a PTCDA unit cell with $\delta = 30°$ stem from domains on HBC and not from Phase **C** PTCDA on Au(111). A clear argument in favor of this assumption is the fact that Phase **II** has a point-on-line relation to the HBC lattice. This is evidenced in Fig. 7.3(e) by the coincidence between the $(01)_{HBC}$ and $(01)_{PTCDA}$ spots. It is a remarkable result as it means a coexistence of POL and LOL phases of PTCDA on HBC, with the LOL phase actually being the dominant one. One should, in contrast, conclude that a POL growth is always related to a higher gain in potential energy (Chapter 4). This seeming discrepancy is dealt with in the next chapter.

- **Phase III**: The epitaxial relation between PTCDA Phase **III** and the HBC substrate has been clarified in the discussion of the FFT in Fig. 7.5(d). An interesting aspect is given by the fact that the epitaxial growth of QT on HBC on Au(111) is, as well, characterized by a coincidence of the (1$\bar{2}$) lattice line of HBC with an adsorbate lattice line [42]. Whether this correspondence between PTCDA and QT on HBC is only accidental or whether it is an evidence for a special property of the (1$\bar{2}$) lattice lines of HBC will be discussed in the next chapter as well.

A summary of the three epitaxial phases found for PTCDA on HBC is given in Figure 7.6. The coincident lattice lines in the real-space lattices of each molecular species are dashed. In order to complete the discussion of the

Table 7.3: List of (hypothetical) HBC lattice constants that would allow the growth of PTCDA in POL/LOL fashion with unit cell parameters resembling the (102) plane of either the α or the β modification of PTCDA. The (61)(91) LOL coincidence for PTCDA on HBC on graphite is included for comparison.

PTCDA modific.	a_{HBC} (01)(01) POL	a_{HBC} $(1\bar{2})(3\bar{2})$ LOL	a_{HBC} (50)(80) LOL	a_{HBC} (61)(91) LOL
α	13.81 Å	13.57 Å	14.37 Å	13.99 Å
β	14.38 Å	13.67 Å	13.93 Å	13.59 Å

geometric aspects, an attempt is made to condense all findings into a single table and to check for plausibility. POL and LOL epitaxy require, different from commensurate epitaxy, no specific epitaxial matrix, but only put certain constraints on individual elements of **C** (POL). Consequently, it is impossible to deduce a specific PTCDA unit cell geometry from the knowledge of a hexagonal HBC lattice with lattice constant a_1 and a certain LOL relation, e.g. (50)(80) LOL. Such an analysis *is*, however, possible in the inverse direction: Starting from a PTCDA unit cell and a LOL relation, the respective HBC lattice constant can be determined. Fortunately, there are values for a "native" 2D unit cell of PTCDA as found in its α and β bulk modification. Assuming that PTCDA likes to adopt one of these two geometries, one can ask which *hypothetical* HBC lattice constant would allow the growth of PTCDA under a specific LOL relation. The results of this consideration are summarized in Table 7.3. One should keep in mind that the *observed* lattice constant of the compressed HBC layer is $a_1 = (14 \pm 0.2)$ Å, and that the Phase **I** geometry, i.e., the (50)(80) LOL, is much closer to the β modification. Three conclusions can be drawn from this compilation of data:

- PTCDA prefers to adopt the β modification unit cell over the α modification unit cell. If the α parameters were favored, one would observe a (61)(91) LOL relation between PTCDA and HBC on Au(111) and not the (50)(80) LOL phase.

- The preference for the β geometry is also indicated by the occurrence of the (01)(01) POL phase of PTCDA on the HBC sample with the large initial lattice constant ($a_1 = 14.75$ Å, Fig. 7.3). For the growth in the α geometry, a HBC lattice constant below 14 Å is required, while for the β geometry a value $a_1 > 14$ Å is necessary.

- The occurrence of the Phase **III** of PTCDA observed in the "inverted" layer necessarily means a deformation of the HBC, the PTCDA, or both lattices, perhaps fostered by the annealing process. The STM image in Fig. 7.5 allows no precise analysis of this issue.

7.3.2 Energetic gain of epitaxial structures

It emerged from the discussion of epitaxy in terms of potential energy in Chapter 4 that any LOL coincidence is related to an energetic gain V'_{inter} in the substrate-adsorbate potential. While the more general discussion of this gain is subject to the following chapter, here, the three epitaxial structures of PTCDA on HBC will be compared to each other and to the structure found by Mannsfeld et al. on HBC on graphite [39]. The question, which energetic gain results from the model calculations will be addressed.

The calculations are performed for fixed PTCDA and HBC lattices. The HBC parameters are $a_1 = 14.0\,\text{Å}$, $\alpha = 60°$ and $\zeta = 5°$. The PTCDA unit cell was individually adjusted to achieve LOL coincidence. For all PTCDA phases the molecular orientations $\zeta_{1,2}$ of the β bulk phase were used (Fig. 2.5). The potential energy per molecule V_{inter} of a large PTCDA domain consisting of ≈ 8000 molecules is calculated repeatedly, while moving the entire domain over the HBC substrate. Figure 7.7 shows grayscale maps of V_{inter} which include skeletal HBC molecules. All grayscale maps show a 1D potential with stripes parallel to the respective coincident substrate lattice lines (compare Fig. 7.6). This behavior of V_{inter} results from the fact that no registry between substrate and adsorbate lattice exists in the direction of the stripes, while the LOL or POL epitaxy defines the registry in the direction normal to the stripes. Hence, the maps visualize the sum of all coherent potential energy plane waves that contribute to V'_{inter} (Eq. 4.9). Imagining a new coordinate system with the x-axis parallel to the coincident lattice line and the y-axis normal to it, all adsorbate molecules have an arbitrary x-position (also with respect to the substrate lattice), while only distinct y values are allowed. Shifting the entire domain in x-direction does not change this situation, while a shift along the y-axis does, thus creating the 1D periodic potential.

It is worth mentioning that the variation in V_{inter} (and thus the energetic gain V'_{inter}) of each phase of PTCDA is quite similar. The reference value for V'_{inter} is the incommensurate energy $E_0 = -1.417\,\text{eV}$ per molecule calculated for PTCDA on a HBC layer with $a_1 = 14\,\text{Å}$.[3] The values for V'_{inter} in all four LOL relations are given in Tab. 7.4. Surprisingly, the energetic gain in the (01)(01) POL relation exceeds the gain found for the LOL coincident phases only by a factor between 1.7 and 2.5. This clearly indicates that no simple quantitative picture of the energetic gain in organic-organic heteroepitaxial structures exists, and serves as a motivation for a more detailed analysis of this matter in Chapter 8. It also provides a first explanation why the POL coincident Phase **II** of PTCDA is not the dominant one as should be expected from the qualitative argument POL vs. LOL.

Another important aspect is the chirality of the HBC layer due to the

---

[3] The substrate-adsorbate potential depends on the overall density of atoms in each layer and thus on the HBC lattice constant.

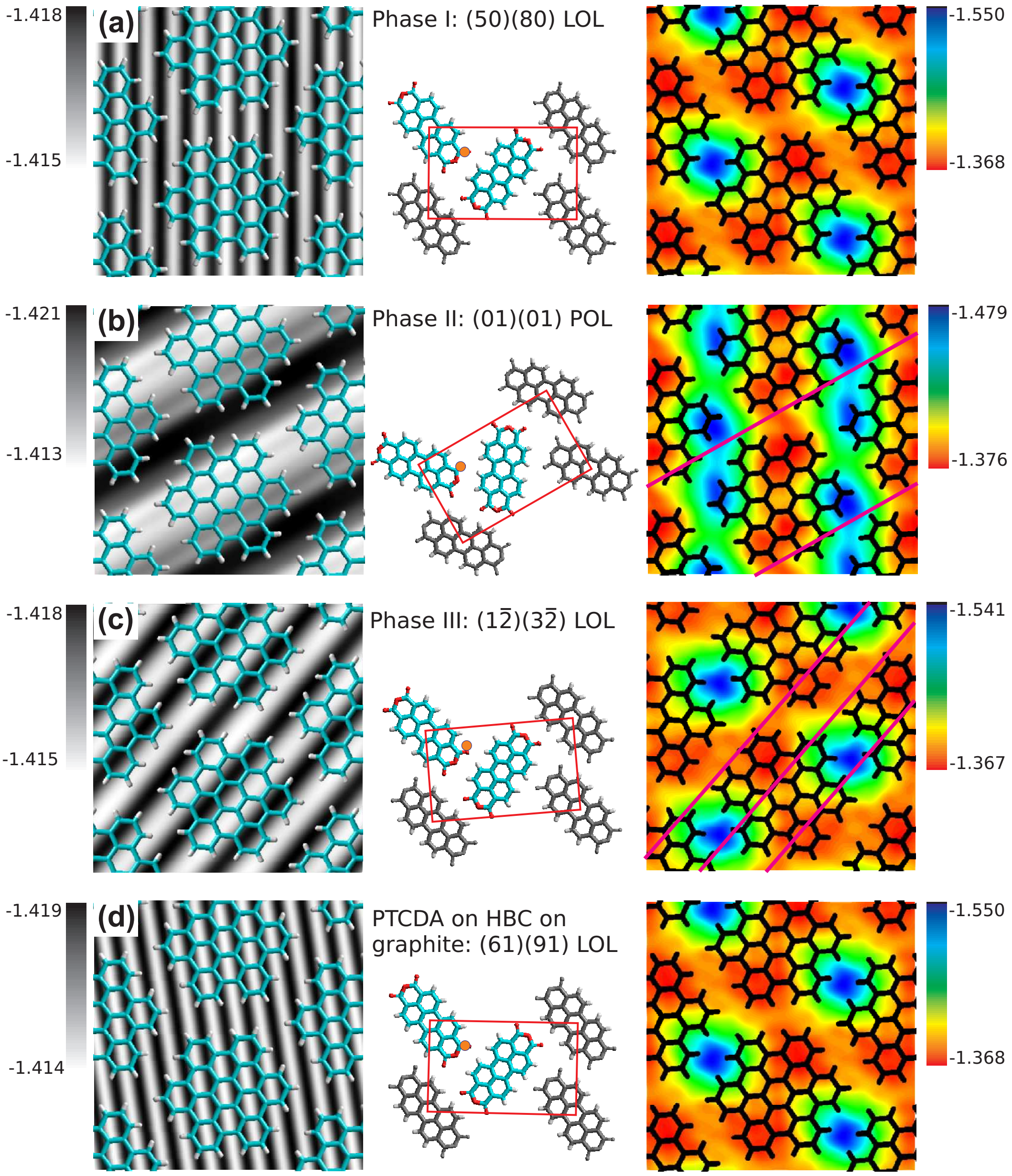

Figure 7.7: Potential energy maps of all epitaxial phases of PTCDA on HBC found on either Au(111) or on graphite. The energy values are given in eV per PTCDA molecule. The grayscale maps show the dependency of V_{inter} on the *position* of a PTCDA domain containing ≈ 8000 molecules. The resulting potential is quasi 1D as its variation in the direction of the coincident lattice lines is negligible. The middle row shows the respective PTCDA unit cell. The full-color maps on the right hand side represent V_{single} for only two PTCDA molecules in an arrangement resembling the basis of the PTCDA lattice (colored molecules). Positions in all maps are related to the orange dot in the unit cells that marks the center of gravity of the two PTCDA molecules in the basis. For Phase **II** and **III**, the minima of the grayscale maps are indicated by purple lines in the full-color maps.

Table 7.4: Calculated energetic gain per molecule in the respective LOL phase. If meaningful, the PTCDA lattice was mirrored at a primitive HBC lattice line (indicated by asterisk) to illustrate that this symmetry operation is *not* allowed on the chiral structure of HBC molecules rotated by $\zeta \approx 5^\circ$ and the energetic gain is severely reduced. The *kcal/mol* values allow a direct comparison to Refs. 16 and 39.

Phase	**I**	**II**	**III**	**III***	Ref. 39	[39]*
LOL rel.:	(50)(80)	(01)(01)	$(1\bar{2})(3\bar{2})$	$(32)(\bar{3}2)$	(61)(91)	$(5\bar{1})(9\bar{1})$
V'_{inter} (meV):	-1.65	-3.73	-1.78	-0.61*	-2.17	-0.22*
$V'_{inter}\left(\frac{kcal}{mol}\right)$:	-0.038	-0.086	-0.041	-0.014*	-0.050	-0.005*

orientation of the molecules under $\zeta = 5^\circ$. In Phase **I** and **II** the PTCDA lattice is aligned to one of the primitive HBC lattice vectors and the chirality is not of importance. For Phase **III** PTCDA, however, mirror domains exist which are not equal in terms of energetic gain as the alignment between HBC and PTCDA is not the same for both types of domains. For this reason the azimuthal orientation of the HBC molecules in Fig. 7.7(c) has been set to $-\zeta$ as otherwise the energetic gain would have been too small. This is illustrated in Table 7.4 where the energy for both mirror domains is presented.

A full color map of $V_{single}(\mathbf{r})$ (Eq. 4.1) is calculated by moving a single PTCDA *basis* (consisting of *two* molecules) over the HBC substrate. A comparison between color and grayscale maps gives an insight how the energetic gain is actually created and why it is so low. For the generally lower gain in energy in all POL and LOL phases, compared to the values given in Refs. 16 and 39, a different model setup used in the calculation can be made responsible. While the substrate system in Refs. 16 and 39 consisted of HBC molecules on a slab of graphite, a free HBC layer is used in the present calculations. The additional graphite layers create an attractive potential without any relevant corrugation. Hence, one would expect an influence on E_0 only. Nonetheless, the corrugation in $V_{single}(\mathbf{r})$ (the amplitudes $E_{i,j}$ in Eq. 4.1) and thus the energetic gain in any epitaxial structure is increased due to the attractive potential. This effect can be understood in analogy to the phenomenon of friction where a force normal to the contact plane changes the corrugation of the lateral potential.

The decision to perform model calculations without the Au(111) substrate can be motivated by two facts. While HBC on graphite forms a commensurate overlayer, there exists no such alignment for HBC on Au(111). Consequently, all HBC molecules adopt non-equivalent sites. The grid method used to speed up the calculation of V_{inter}, however, automatically creates a periodic situation by mapping the whole substrate surface on the first unit cell. Using an incommensurate Au(111) substrate would, consequently, lead to discontinuities in the potential at the unit cell boundary. Furthermore, the OPLS force-field preferably used to model the interaction between hydrocarbons contains no parameters for the interaction with Au atoms. The only force-field that does (UFF) is, in turn, less suitable for the calculation of hydrocarbons.

Either way, the results of the potential energy calculation are only of limited accuracy. What is, however, much more important than getting accurate *absolute* values for E_0 is to get a sufficiently correct single molecule potential $V'_{single}(\mathbf{r})$, i.e., reasonable values for $E_{i,j}$ and $\phi_{i,j}$ (Eq. 4.2).

7.3.3 Mutual alignment of lattices

As evidenced in the last section, the potential energy calculations are a key element in comprehending the implications of POL and LOL epitaxy on *real* systems. A *very* important task in this context is to give a proof that the atomic force-field approach used to model the interface potential V_{inter} allows a sufficiently correct description of organic-organic heterosystems. Until now, it was only shown that calculations based on this approach are able to assign an energetic gain V'_{inter} to a specific epitaxial structure, reproducing the result of Eq. 4.9. As an energetic minimum would, in accordance with Eq. 4.9, emerge for basically *any* potential energy function $V_{single}(\mathbf{r})$ that has the substrate lattice periodicity, conclusions about the quality of the calculation cannot be derived. Hence, the question to what extent the interaction between large aromatic molecules possessing a delocalized π-system can be modeled correctly by assuming atom-atom potentials is important for the justification of this method.

The potential energy calculations presented in Figure 7.7 do not only yield a value for the energetic gain V'_{inter} under a specific coherence between substrate and adsorbate lattice lines. Additionally, the phase $\phi_{i,j}$ is provided, i.e., the mutual alignment of both lattices normal to the respective lattice lines (ij) for which V'_{inter} is minimal. If the potential $V_{single}(\mathbf{r})$ is modeled properly, the method should be able to correctly predict the actual alignment found in the experiment. While it is not possible to deduce the respective data from a LEED pattern, it is, in principle, possible to extract the positions of substrate and adsorbate molecules from a STM image. Here, the method of choice is the inverse FFT already used to produce the images in Fig. 7.5. To obtain reliable *and* suitable results, a high resolution STM image of the heterolayer is necessary. Furthermore, the indices $(i,j)(k,l)$ of the respective LOL relation should be rather small. If the latter requirement is not fulfilled, the spacing between equal coincident lattice lines will be below the spatial resolution of the image, rendering any attempt to locate individual molecules on the respective scale void. Therefore, even in a high quality STM image, it is difficult or impossible to check whether the mutual alignment between HBC and PTCDA in Phase **I** corresponds to the predicted results in Fig. 7.7(a).

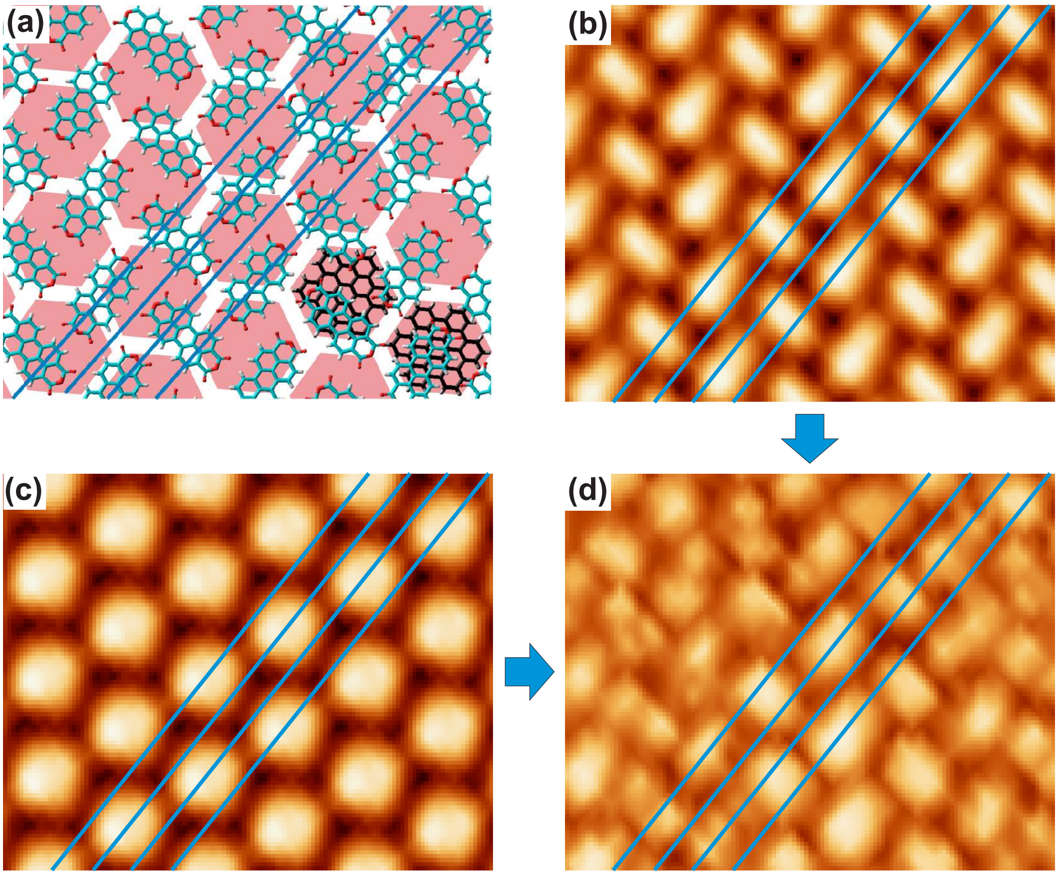

Figure 7.8: **(a)** Model of the mutual alignment in heterosystem PTCDA Phase **III** on HBC. The position of the PTCDA layer in the direction of the coincident lattice lines (blue) is arbitrary, while the alignment normal to this direction corresponds to the energetic minimum found for this phase in Fig. 7.7(c). **(b)** and **(c)** are cutouts of Fig. 7.5 (c) and (d), respectively, taken at exactly the same position. Any lattice information can thus be transferred from one image to the other, enabling a direct comparison of the mutual alignment found in the STM image to the result of the potential energy calculation. A comparison between (a) and (b) shows indeed a full correspondence. **(d)** Original unfiltered STM contrast in the area of (b) and (c).

The situation is different for Phase **III** with the LOL coefficients $(1\bar{2})(3\bar{2})$ and the STM image in Fig. 7.5(a). The respective analysis in Figure 7.8 features a real-space model of the optimal adsorption geometry according to the force-field calculation, as well as two inverse FFT images showing either the HBC or the PTCDA contrast. Here, the important aspect of the inverse FFT is the preservation of the phase information: Figs. 7.8(b) and (c) show the PTCDA and HBC molecules at *exactly* the same sample position. The original, unfiltered image is shown in Fig. 7.8(d) for comparison. In (a) as well as in (c), the centers of the HBC molecules are connected by $(1\bar{2})$ lattice lines which now serve as a template to locate the PTCDA molecules. Therefore, the blue lines from Fig. 7.8(c) have been copied to (b) and (d). A comparison between (a) and (b) shows that the experimentally derived positions of the individual PTCDA molecules relative to the $(1\bar{2})_{HBC}$ lattice lines are indeed identical to the positions belonging to a minimum in V_{inter}. This remarkable result is, though not a proof, nevertheless a strong evidence that $V_{single}(\mathbf{r})$ as calculated by the atomic force-field method bears strong resemblance to the *real* substrate adsorbate potential.

At this point, two important ingredients for a more general study of POL and LOL epitaxy in organic-organic heterosystems have been found: Firstly, four different epitaxial relations between PTCDA and HBC have been identified from the experiment.[4] This allows, for the first time, a comparative analysis of different LOL relations in one and the same system. Secondly, it was possible to show that the tool of choice, the potential energy calculation via force fields, yields at least qualitatively correct results for the interface potential. Prior to the aforementioned study which is contained in the next chapter, some final aspects of organic-organic layers of PTCDA and HBC will be reported here.

7.4 Heterosystems of PTCDA and HBC with inverted stacking sequence

As an important step towards increased complexity, attempts were made to invert the stacking sequence and to create highly ordered samples of HBC on PTCDA on Au(111). If the stability of the inverted system would be confirmed, this would pave the way to more elaborate structures involving several alternating layers of HBC and PTCDA. Here, a single experiment including deposition of HBC on PTCDA and subsequent annealing is analyzed. It reveals several fundamental properties of the HBC|PTCDA|Au(111) system.

The LEED pattern of the initial PTCDA sample is equivalent to the one shown in Fig. 7.1. After a deposition of $\approx 0.6\,\mathrm{ML}$ HBC, a faint ring just inside the inner PTCDA spots appears in the LEED (Fig. 7.9(a)). This ring features dark areas "below" the spot triples that belong to PTCDA Phase **A** domains (blue ellipse in Fig. 7.9(a)). The true nature of these areas is revealed in comparison with the LEED pattern taken at a ML coverage of HBC (Fig. 7.9(b)). Now, several intense spots are visible that can be associated with an ordered HBC layer. Three different orientations of the HBC lattice can be identified. The respective reciprocal unit cell vectors are indicated in Fig. 7.9(b). The orange vectors can be attributed to the 30° phase of HBC on Au(111). This finding already indicates that a considerable part of the HBC molecules diffuses into the PTCDA layer. The two HBC spots marked by blue

---

[4] Three in the system PTCDA on HBC on Au(111) and one in PTCDA on HBC on graphite [39].

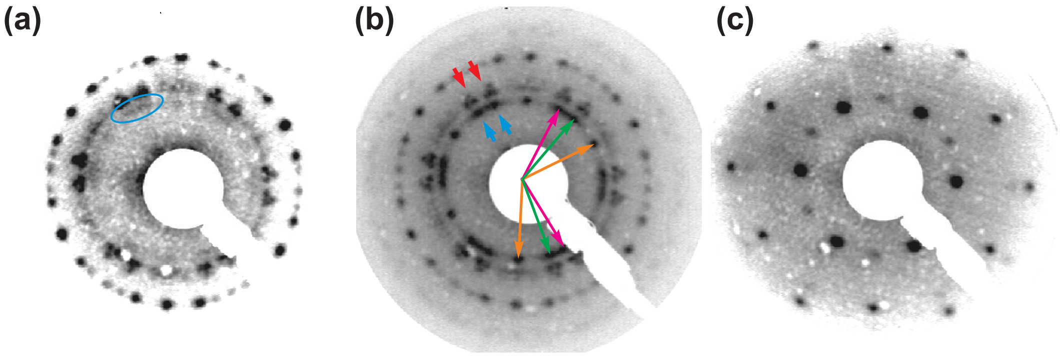

Figure 7.9: All LEED patterns have been recorded at $E_0 = 10.4\,\mathrm{eV}$ **(a)** LEED pattern of 0.6 ML HBC on PTCDA|Au(111). Important, though barely visible, are the dark areas "below" all the intense triangles of PTCDA spots (blue ellipse). These areas are first order HBC spots as becomes clear in a comparison with pattern (b). **(b)** LEED pattern of 1.0 ML HBC on PTCDA|Au(111). The red arrows mark the characteristic PTCDA spots belonging to Phase **A** PTCDA while the blue arrows mark HBC spots. The reciprocal unit cell vectors for all major HBC orientations are indicated. **(c)** If the sample is annealed to 250°C only the HBC (!) spots remain.

arrows can most likely be related to the adjacent triplets of PTCDA spots marked in red. As in the dominant Phase **I** of PTCDA on HBC, each HBC spot is right below a triplet. It is thus only reasonable to assume that the respective HBC domains grow in this very epitaxial relation on PTCDA. As a matter of fact, the *interface* potential V_{inter} is the same, no matter which layer is called substrate and which adsorbate.[5] The respective unit cells of both HBC orientations are marked in green and magenta.

The fact that the *positions* of the HBC spots in Figs. 7.1(a) and (b) remained unchanged, although the coverage was increased by 0.4 ML, indicates that the intermolecular potential in the HBC film is *attractive* if the film grows not directly on the metal substrate. This observation is important as it supports the conclusions drawn for the *repulsive* interaction in Chapter 5. It was proposed that a screening of the attractive London forces by the metal fosters the repulsion. Hence, with a separating PTCDA layer, the attraction between the HBC molecules should be restored as it is indeed observed here.

Upon annealing of a HBC|PTCDA|Au(111) system at 90° C for 30 minutes, the stacking sequence is inverted and highly ordered PTCDA on HBC domains can be found as mentioned in Section 7.2. This constitutes an impressive demonstration of the robustness of the respective ordering process. Unfortunately, it also indicates that HBC|PTCDA|Au(111) is not as stable as its inverted counterpart. One interesting implication of this "exchange reaction" in a physisorbed system is the desorption temperature for PTCDA. Figure 7.1(c) shows the LEED pattern after further annealing to ≈ 250° C.

---

[5] This simplified relation is fully valid only if the Au(111) surface is neglected.

There is no sign of a PTCDA layer anymore. This result fits nicely to the desorption temperature of the second ML of PTCDA in a PTCDA double-layer, which is 265° C [95] and indicates that the PTCDA contact layer is completely replaced by a HBC ML and subsequently desorbed from the HBC. In contrast, a single PTCDA ML on Au(111) was found to desorb at ≈ 450° C.

Summarizing, a reaction is observed in which a PTCDA contact layer is replaced by a HBC layer that was initially on top. This process yields ordered PTCDA on HBC domains as an intermediate step and allows to desorb the PTCDA layer at a substantially reduced temperature. The respective system is an example that illustrates the important role of interface energetics for the creation of stable vertically structured layer systems.

8 General Properties of POL and LOL Epitaxy

In the last chapter it was concluded that POL and LOL epitaxy is indeed the dominant ordering principle in organic-organic heterosystems. In particular, three different epitaxial relations were found in one and the same system, thus illustrating the importance of this concept. In this chapter, the general properties of POL and LOL epitaxy will be investigated using the phases found for PTCDA|HBC|Au(111) as examples. The motivation for this study is to generalize the findings made for one model system and to make them transferable to other systems as well. As a first step to a more universal description of LOL epitaxy, a new coordinate system will be introduced in the following section. Based on this system, a method is described that allows to calculate the energetic gain of an epitaxial adlayer independent of a specific domain size or shape.

8.1 A new coordinate system

In this chapter, not a specific but all LOL relations shall be discussed. Hence, a uniform description applicable to all substrate lattice lines is beneficial and will now be developed. For this purpose a new coordinate system is used, resembling the idea mentioned in the last chapter: While usually the substrate is described by the primitive lattice vectors $\mathbf{a}_1$ and $\mathbf{a}_2$ which define an unit cell of the area A_a, here, an individual coordinate system will be used for the description of each substrate lattice line. Starting from the two indices i and j describing a reciprocal lattice vector $\mathbf{r}^* = i\mathbf{a}_1^* + j\mathbf{a}_2^*$ and the respective lattice lines $(ij) \perp \mathbf{r}^*$, the new, rectangular unit cell is defined by the two vectors $\mathbf{v}_1 \,||\, (ij)$ and $\mathbf{v}_2 \,||\, \mathbf{r}^*$. The vector $\mathbf{v}_1$ connects two neigboring real-space lattice points on the (ij) lines:

$$\mathbf{v}_1 := j\mathbf{a}_1 - i\mathbf{a}_2, \tag{8.1}$$

The norm of $\mathbf{v}_1$ is consequently the distance between two such points, while the norm of $\mathbf{v}_2$ equals the spacing between neighboring (ij) lines:

$$|\mathbf{v}_2| := \frac{A_a}{|\mathbf{r}^*|}. \tag{8.2}$$

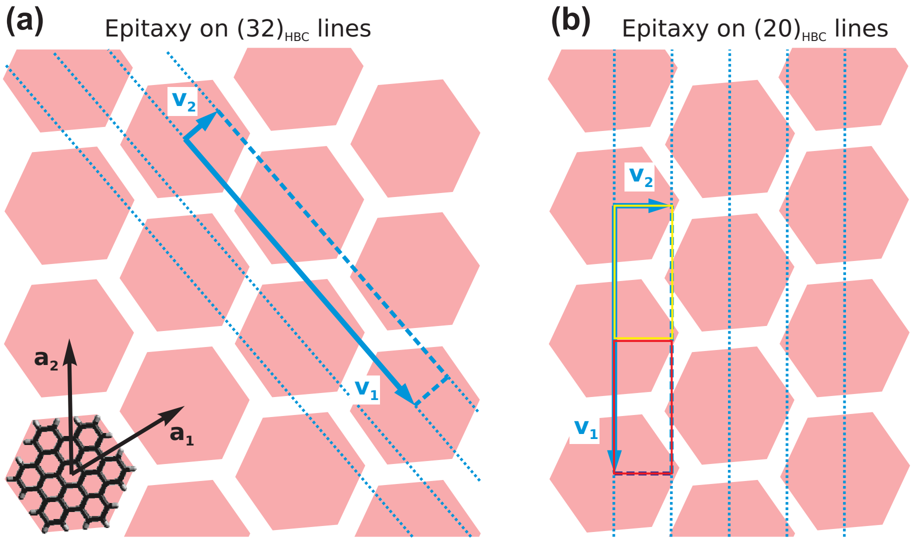

Figure 8.1: Scheme illustrating the construction of a new rectangular lattice based on an arbitrary lattice line of the original primitive lattice. This coordinate system allows a simple, uniform description of LOL epitaxy as a growth on $(01)_n$ lines of the new lattice. The potential energy V_{inter} of an (infinitely) large LOL coincident adsorbate domain can be calculated by averaging the energy of a *single* molecule along $\mathbf{v}_1$. For epitaxy on (ij) lines of the original lattice with $D = GCD(i,j) > 1$, the averaging has to be performed on D subsequent $(01)_n$ lines (see text).

Furthermore, $\mathbf{v}_2$ is parallel to $\mathbf{r}^*$:

$$\mathbf{v}_2 := \frac{\mathbf{r}^*}{|\mathbf{r}^*|}\frac{A_a}{|\mathbf{r}^*|}. \tag{8.3}$$

An interesting aspect is given by the fact that the area A'_a of this new unit cell is identical to the area A_a of the unit cell defined by the primitive lattice vectors. Simply spoken, the higher the indices i and j of a lattice line, the smaller the separation between two such lines. In the following, lattice lines referring to this new coordinate system will be marked by the subscript n.

The discussion of LOL epitaxy can be generalized now by making it independent of specific values i and j and of a specific adsorbate lattice. The coherence requirement expressed in Chapter 4 demands that all adsorbate molecules are located on the $(01)_n$ lattice lines (which are parallel to $\mathbf{v}_1$), while nothing is specified concerning the positions *on* these lines. The case of an additional coherence in the direction of $\mathbf{v}_1$, a superlattice with only a few discrete positions along $\mathbf{v}_1$, shall not be discussed here. Instead, a “perfectly” incoherent distribution along the $(01)_n$ lines is assumed, a situation that can only be achieved in a very large domain. The potential energy V_{inter} per molecule of such a domain then equals the *average* potential energy $\overline{V_{single}}(\mathbf{r})$ of a single molecule moved along $\mathbf{v}_1$. This situation is depicted in Figure 8.1 for two exemplary HBC lattice lines. While the energy V_{inter} in the case of epitaxy on $(32)_{HBC}$ lines can be calculated exactly as mentioned above, a modification is necessary if i and j have a common divisor D larger than one.[1] In this case, illustrated by the example of $(02)_{HBC}$ lines, the potential inside the *new* unit cell exhibits a periodicity: The yellow and red box in Fig. 8.1(b) contain identical areas of the substrate. Here, the potential energy V_{inter} of a LOL coincident domain is not the average along $\mathbf{v}_1$ only, but along D subsequent lattice lines parallel to $\mathbf{v}_1$, with $D = GCD(i, j)$. In Fig. 8.1(b) this would mean to average along both long sides of the red or yellow box.

The domain energy calculation conducted by scanning one single molecule over the surface is beneficial over a calculation via the mapping of a certain domain of finite size into the primitive substrate unit cell as implemented in PowerGrid. In a small domain, the requirement of a "perfectly" uniform distribution along the $(01)_n$ lines, as expressed above, is not valid. Depending on the size and shape of the domain, the molecules occupy certain positions while others are left out. If the energetic gain resulting from the epitaxial relation is very small, very large domains have to be considered to obtain potential energy maps that are independent of the shape and the position of the domain in the direction of $\mathbf{v}_1$. If, however, the calculation is performed by scanning a single molecule along $\mathbf{v}_1$, the averaging can easily be controlled by using a small step width, mimicking an almost perfect distribution of molecules. Although this is an abstraction, a step away from the simulation of "real" domains, it is suitable for a discussion of general properties of LOL epitaxy.

With the method outlined above, the actual interface energy V_{inter} per molecule related to the growth on a certain substrate lattice line can be determined as the minimal energy achievable when moving the line(s) of averaging stepwise in the direction of $\mathbf{v}_2$ until the whole (new) unit cell has been scanned. In principle, this means a search for one minimum of the respective potential energy plane wave. The energetic gain V'_{inter} is then obtained by subtracting the incommensurate energy E_0 (Eq. 4.6). As expressed by Eq. 4.9, the energy V'_{inter} equals the respective Fourier coefficient $E_{i,j}$ *if* the contribution of all higher order coefficients $E_{m \cdot i, m \cdot j}$ is insignificant.

The method for the potential energy calculation outlined in this section has been implemented as a PowerGrid script with the following parameters: The step width for the averaging process along each line was set to 0.1 Å. The averaging was repeated 50 times while shifting the line of averaging in the direction of $\mathbf{v}_2$ in search for the minimum in V_{inter}. The orientation ζ of the adsorbate molecule was varied in 1° steps. If the basis of the unit cell is used (which contains two molecules in case of PTCDA), ζ refers to the orientation of the whole basis. With these parameters, the calculation of all $V'_{inter}(\zeta)$ functions with $|i|, |j| < 12$ took $\approx 3\,\mathrm{h}$ for one substrate-adsorbate system on a desktop PC. The results obtained for the system PTCDA on HBC shall be discussed exemplarily in the following section. The dependency on ζ and the

---

[1] greatest common divisor (GCD)

stripy potential energy maps in Fig. 7.7 are selected to illustrate key issues of the PTCDA-HBC interface potential.

8.2 Specific properties of the substrate-adsorbate potential

The energetic gain per molecule V'_{inter} in a LOL coincident domain is not coupled to a specific adsorbate unit cell. For given indices i and j, the gain is only a function of the azimuthal orientation of the adsorbed molecules located on the respective lines. The molecular orientation ζ was previously shown to have a strong impact on the energetic gain in different commensurate phases of HBC on Ag(111) and Au(111) (Fig. 6.3). An example, illustrating the strength of the ζ-dependency in POL and LOL epitaxy is shown in Fig. 8.2(a) for the growth of PTCDA on the $(50)_{HBC}$ and the $(01)_{HBC}$ lattice lines respectively. The basis of the PTCDA unit cell (Fig. 8.2(b)) which has no rotational symmetry is used in the calculation. Still, the resulting energy curves exhibit a 180° periodicity originating from the point symmetry of each lattice line. The energetic gain $V'_{inter}(\zeta)$ varies from -2.17 meV to -43 meV for the $(01)_{HBC}$ lines and from +0.22 meV to -1.95 meV for the $(50)_{HBC}$ lines.

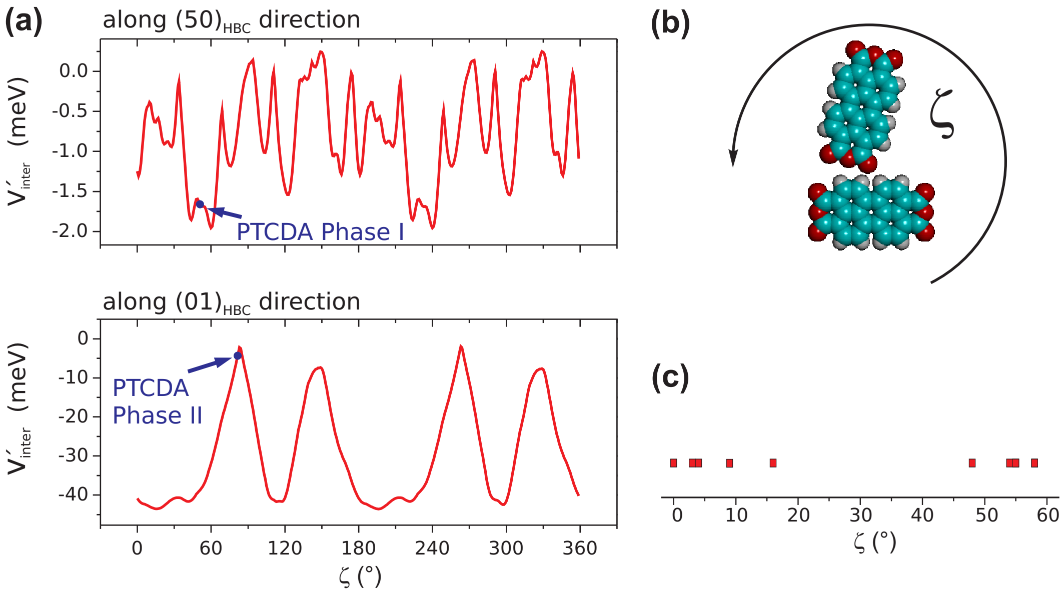

Figure 8.2: **(a)** Dependency of the energetic gain V'_{inter} for a LOL growth of PTCDA on $(50)_{HBC}$ and $(01)_{HBC}$ lattice lines on the azimuthal orientation ζ of the PTCDA molecules. The actual orientations in Phase **I** and **II** of PTCDA are indicated by arrows. **(b)** Basis of the PTCDA lattice consisting of two molecules as used in the calculation. The model shown is oriented under $\zeta = 0°$. **(c)** Values of ζ belonging to the maximal energetic gain from a LOL growth of PTCDA. The ten HBC lattice lines with the highest gain have been selected. Obviously, there is no single optimal orientation of PTCDA.

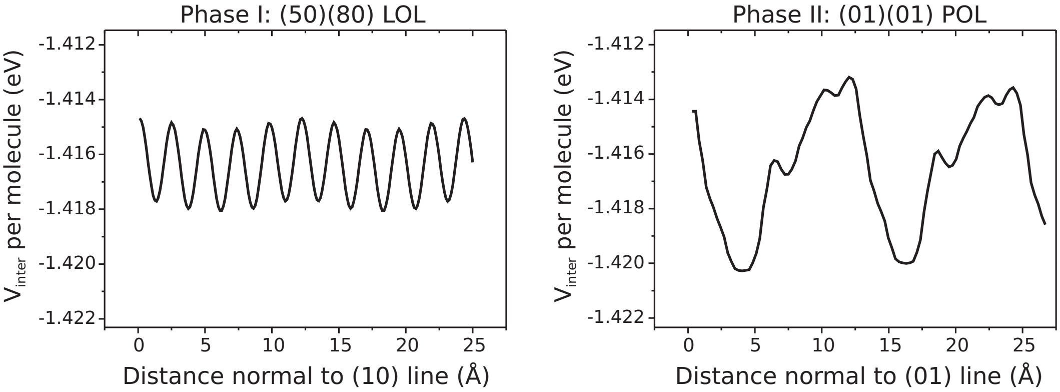

Figure 8.3: Profiles along the grayscale maps in Fig. 7.7(a) and (b). While the 1D potential energy pattern is almost harmonic for the epitaxy on a high-index lattice line (like the $(50)_{HBC}$ line), the significant contribution of higher order harmonics is visible in the case of epitaxy on $(01)_{HBC}$ lines. Here, the profile is far from being harmonic.

The apparent discrepancy of similar energetic gain for POL and LOL coincident phases found in Section 7.3 can be addressed using the curves in Figure 8.2(a). The orientation of the POL coincident lattice of PTCDA Phase **I** ($\delta = 30°$) means an angle $\zeta = 82°$ for the basis displayed in Fig. 8.2(b). This is very close to the "worst case" angle $\zeta = 84°$ at which the energetic gain on the $(01)_{HBC}$ lines is minimal. For Phase **I** PTCDA, the respective angle is $\zeta = 52°$ which means an energetic gain close to the highest value possible for a growth on the $(50)_{HBC}$ lattice lines.

The speculation that a high energetic gain is strongly correlated with a specific alignment between the graphitic bodies of substrate and adsorbate molecules does not hold. This can be concluded from the strong fluctuations in the upper curve of Fig. 8.2(a). In Fig. 8.2(c), the *optimal* ζ values are plotted for a growth along the ten HBC lattice lines providing the highest energetic gains. No single preferential orientation exists.

While the dependency $V'_{inter}(\zeta)$ gets more "noisy" with increasing lattice line indices, the potential energy map for an entire domain fulfilling the requirements for LOL coincidence simplifies with higher indices (Fig. 7.7). This shall again be illustrated by drawing a comparison between PTCDA Phases **I** and **II**. Two profiles normal to the coincident HBC lattice lines in the grayscale maps in Fig. 7.7 are compared in Figure 8.3. For the (01)(01) POL case (Phase **II**), the profile through V_{inter} is much more irregular than for the case of the (50)(80) LOL coincidence (Phase **I**) which features a close-to-harmonic profile. This observation can be understood in terms of Eqs. 4.8 and 4.9. As all higher order coefficients $E_{m \cdot i, m \cdot j}$ contribute, no harmonic profile is expected in general. The respective contributions *have* a clear effect for $i = 0$ and $j = 1$, while they are obviously irrelevant for high indices i and j.

8.3 The "natural order" of the lattice lines

Considering the experimental results for the growth of PTCDA on HBC (and also QT on HBC [42]), the most important question to be answered is whether there is a general rule that defines which HBC lattice lines are most likely to participate in LOL epitaxy. Growth on (01), $(1\bar{2})$, (50) and (61) lines has been observed experimentally. The first question that shall be discussed in this context is whether the likeliness of LOL epitaxy depends on the inner structure of the substrate and / or adsorbate molecules. It was speculated in Ref. 16 that the graphitic subunits of HBC are responsible for the occurrence of LOL epitaxy. A simple way to analyze the necessity for an inner structure is the creation of a completely artificial schematic potential by the following basic rule: The potential energy $V_{single}(\mathbf{r})$ *on* a HBC molecule is lower than *in between* two molecules. This principle can be derived from ζ averaged $V_{single}(\mathbf{r})$ maps (not shown).

A map created according to this principle is shown in Fig. 8.4(a), while the corresponding FFT is shown in Fig. 8.4(b). Recalling the discussion in Chapter 4, the FFT represents a reciprocal space image and the spot intensities are proportional to the Fourier coefficients $E_{i,j}$. These coefficients give, in turn, a good estimate for V'_{inter} in case of the growth on (ij) lattice lines. It is thus immediately clear from Fig. 8.4(b) that LOL growth, even in high order of i and j, is likely to occur on the potential in (a). The ratio of the intensities of $(1,0)$ and $(1,1)$ spots is, for example, only ≈ 2.2. Evidently, an inner structure of a molecule is not a *necessary* prerequisite for LOL epitaxy. A specific shape of the molecules together with their arrangement in a certain lattice are suf-

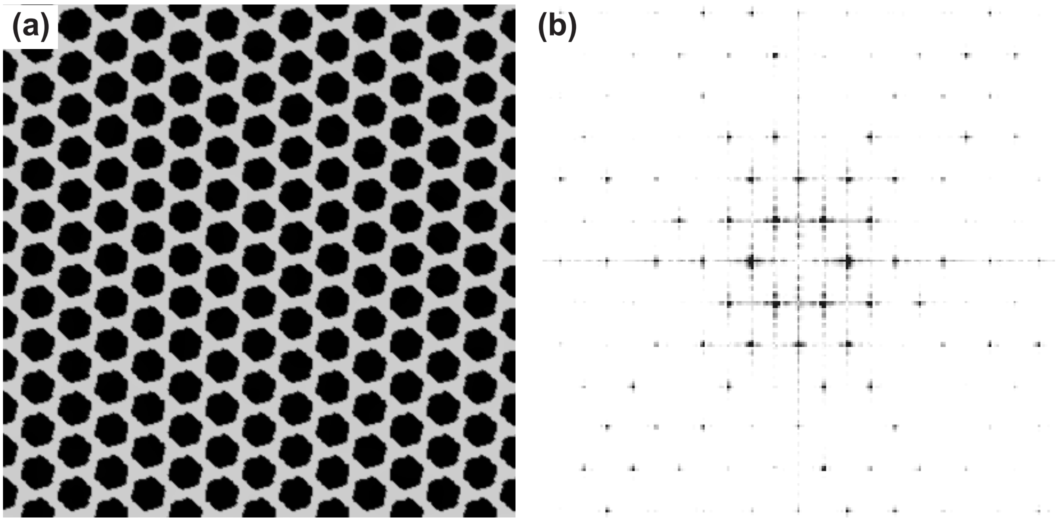

Figure 8.4: **(a)** Schematic potential energy map $V_{single}(\mathbf{r})$ with only two energy values. The occurrence of higher order spots in the FFT shown in **(b)** clearly indicates that also in the absence of any internal structure in the hexagonal "molecules", LOL growth is quite feasible.

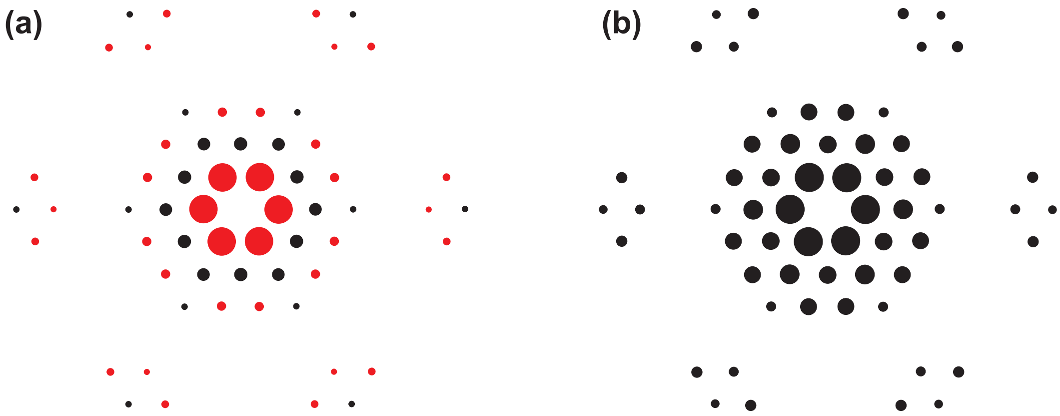

Figure 8.5: Reciprocal space plots of the highest energetic gains $|V'_{inter}(\zeta)|$ achievable under the variation of ζ. Shown are values V'_{inter} for the growth on the eight HBC lattice lines that offer the highest gain. The adsorbates are **(a)** the PTCDA basis and **(b)** a single carbon atom. The chirality of the HBC substrate is neglected by enforcing a mirror symmetry of the plot. Lattice lines of HBC that were experimentally found to participate in LOL epitaxy are shown in red.

ficient to yield considerably large higher-order Fourier coefficients. This does, however, not imply that the graphitic structure of HBC is *not* the reason for the observed LOL growth. An example for LOL epitaxy in the absence of any inner structure is the observed ordering of xenon MLs on several metal surfaces [79]. A general conclusion which is also reflected in Fig. 8.4 can be drawn from Eq. 4.1: The growth in a LOL fashion becomes reasonable as soon as $V_{single}(\mathbf{r})$ deviates significantly from a harmonic potential. A second conclusion can be drawn from the occurrence of LOL epitaxy in organic heterosystems as well as in systems of rare gases on metals: LOL growth is likely if the lattice constants of substrate and adsorbate lattice are on the same order of magnitude but *not* identical. In such cases, the relative distortion of the adsorbate's "natural" lattice which would be necessary to form a commensurate or POL overlayer is too large to be energetically favorable. The observation of a POL growth of PTCDA on HBC is the exception that proves the rule.

The specific order of the Fourier coefficients $E_{i,j}$ for the system of PTCDA on HBC shall now be analyzed in more detail. Due to the ζ-dependency of $V_{single}(\mathbf{r})$, no unambiguous results can be expected here. The discussion is hence based on the optimal, i.e., lowest value $V'_{inter}(\zeta)$ obtained for each lattice line.[2] This is the reason why no *single* potential map and its FFT can be used as in Fig. 8.4. Instead, an artificial reciprocal space pattern is created (Fig. 8.5). It exhibits a hexagonal symmetry and a filled circle is placed at each reciprocal lattice point. The area of each of these circles is proportional to $E_{i,j}$. Only the eight largest values $E_{i,j}$ are included in this plot.

---

[2] Here, the simplification $E_{i,j} = V'_{inter}$ is made. Significant deviations due to higher order hamonics $E_{mi,mj}$ occur only for (10) lines.

Now, a first conclusion on the "natural order" of lattice lines in terms of energetic gain shall be drawn. In general, the energetic gain $E_{i,j}$ decreases with increasing values i and j. This cannot be seen as a strict rule but only as an obvious trend. Depending on the specific potential $V_{single}(\mathbf{r})$ there will be most likely some coefficients $E_{i,j}$ which do not follow this trend. It shall, however, be pointed out that this principle is *independent* of the substrate's inner structure. It is responsible for the observed LOL growth of PTCDA and QT on $(1\bar{2})_{HBC}$ lattice lines as well as for the POL growth of PTCDA on HBC.

However, the high energetic gain associated with the (50), (60) and (61) lattice lines does not fit into this scheme. This gain results from the graphitic structure of HBC as has been shown for the $(61)_{HBC}$ lattice line by Mannsfeld et al. [39]. The fact that the $(50)_{HBC}$ and $(60)_{HBC}$ lines are energetically favored as well can be explained by a certain mismatch between the actual periodicity of graphite (2.14 Å) and the spacing between neighboring lattice lines which ranges from 2.02 Å for the $(60)_{HBC}$ lines to 2.42 Å for the $(50)_{HBC}$ lines.[3]

Summarizing, the four different LOL relations found on HBC can be attributed to *different* mechanisms. While the growth on low-index lines results from a quite universal principle, the growth on high-index lines can be attributed to the graphitic subunits of HBC. This argumentation does not require the existence of *similar* subunits in the adsorbates which can clearly be evidenced by repeating the same calculations for the adsorption of a single carbon atom kept at a height of 2.7 Å above the HBC molecules. The respective reciprocal-space-based plot of the energetic gains in Fig. 8.5(b) is very similar to the plot for PTCDA in (a).

The question, whether there is a direct experimental access to the coefficients $E_{i,j}$ will now be central. In Fig. 8.6, a comparison between the plot of $E_{i,j}$ in reciprocal space with two LEED patterns of a HBC ML on Au(111) (without additional adsorbates) is made. In the pattern recorded at 52.7 eV, a surprisingly high intensity in high-order spots is found. It can be excluded that this intensity is due to a double-scattering process involving the first order substrate spots (compare Fig. 3.2), as the $(10)_{Au(111)}$ spots are weak and not in the vicinity of the respective high-order spots of HBC. It turns out that the intense HBC spots indeed correspond to the groups of four filled circles in Fig. 8.6(b) which mark $E_{5,0}$, $E_{6,0}$, $E_{6,1}$ and $E_{5,-1}$ (and symmetry equivalents thereof). The LEED pattern in Fig. 8.6(c) which contains low order spots of HBC, shows the same close correspondence to the plot in (b). Evidently, the inner structure of single HBC molecules and the order in a HBC ML are reflected in both, in the coefficients $E_{i,j}$ that quantify the energetic gain of an adsorbed overlayer and in the spot intensities $f_{i,j}$ of the LEED patterns (Eq. 3.13).

---

[3] For a HBC lattice constant of $a_1 = 14$ Å.

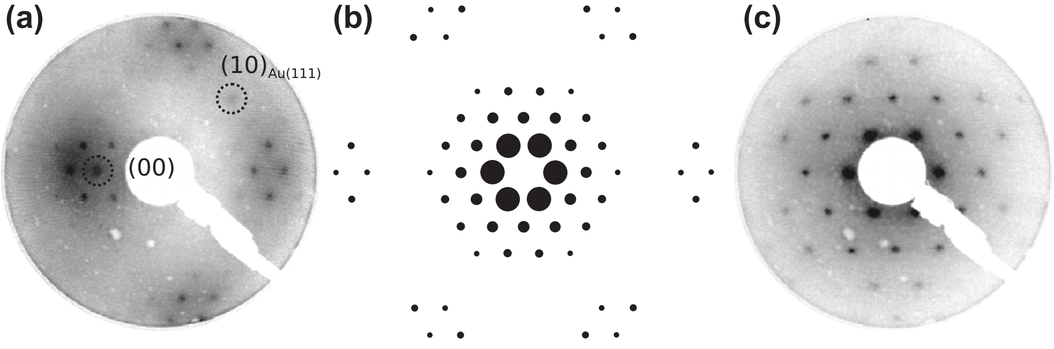

Figure 8.6: Comparison between LEED patterns of HBC taken at 52.7 eV (off center) **(a)** and at 23.3 eV **(c)** to the maximum energetic gains for a LOL growth of PTCDA on a HBC ML **(b)**. A strong coincidence between the LEED spot intensities and the energetic gain is found.

As all three images in Fig. 8.6 show reciprocal space, a direct comparison of the mathematical expressions can be made that include the important quantities. The kinematic description in Eq. 3.13 shall be used for the LEED intensities. As mentioned above, dynamic theory is not required to discuss the spot intensities as they do not result from double scattering. If Eq. 4.1 is compared to the inverse Fourier transform of Eq. 3.13 and the phase ϕ is neglected for sake of simplicity, the following set of mathematically equivalent expressions is obtained:

$$V_{single}(\mathbf{r}) = \sum_{\mathbf{G}} E_{\mathbf{G}} e^{\mathrm{i}\mathbf{G}\mathbf{r}} \tag{8.4}$$

$$\varphi(\mathbf{r}) = \sum_{\mathbf{G}} f_{\mathbf{G}} e^{\mathrm{i}\mathbf{G}\mathbf{r}} \tag{8.5}$$

The left hand sides of Eqs. 8.4 and 8.5 denote the van der Waals potential of a single adsorbate and the scattering potential for low-energy electrons, respectively. Although a strict prove cannot be given here, there is a qualitative correspondence between both quantities. In both cases the "interaction centers", either of the dispersion forces or of the electron scattering process, are the single atoms. In LEED theory, this is reflected in the atomic form factor, i.e., the sum over the scattering powers of all atoms in the unit cell. In the atomic force-field model used to calculate $V_{single}(\mathbf{r})$, one summarizes over all atoms as well (Eq. 3.15). Although this similarity shall not be stressed too much, the single adsorbate and the scattered electrons feel a potential of similar structure which is reflected in similar Fourier transforms, i.e., Fourier coefficients. This analogy should work particularly well in case of HBC as here the potential is mainly related to a single type of atoms (carbon). If several atomic species participate, the (hypothetically) different relative scaling factors between "scattering power" and "dispersion interaction" for each species perhaps mask the geometric similarity.

Concluding, LEED patterns of a substrate allow to deduce information about the energetic gain in case of a LOL epitaxial growth on this substrate. To what extent this finding can be generalized to other substrates needs to be determined by further experiments.

8.4 Prediction of epitaxial growth - a "LOL predictor"

8.4.1 Method

In the last part of this chapter, an algorithm will be outlined that allows an efficient prediction of probable overlayer lattice geometries. Although the algorithm is, as well, based on the aspect of potential energy minimization, it differs significantly from the Monte Carlo method described in Refs. 16 and 74 and implemented in PowerGrid. There are several drawbacks which limit the practical application of the Monte Carlo approach:

- Each execution of a Monte Carlo search yields one single adsorbate structure. To check whether this represents the global potential minimum, the calculation has to be repeated many times. There is no way to obtain systematic information on *local* potential energy minima, i.e., other epitaxial structures that provide a significant energetic gain.

- At least for PTCDA, the unit cell parameters resulting from the force-field calculations deviate by up to 10% from the actual values [16]. As the respective minimum in $V_{intra}(\mathbf{b}_1, \mathbf{b}_2)$ is rather narrow and very deep if compared to V'_{inter}, a free optimization of unit cell parameters and domain orientation and position does usually not yield a correct adsorption geometry.

- The energetic gain V'_{inter} is very small in case of LOL epitaxy (Tab. 7.4). Consequently, a large domain has to be considered in the calculation to reproduce the correct minimum [16]. This, in turn, implies that the lattice constants of adsorbate and substrate have to match with a very high precision to the LOL relation, i.e., the minimum in $V'_{inter}(\mathbf{a}_1, \mathbf{a}_2, \mathbf{b}_1, \mathbf{b}_2)$ is *very* narrow. It requires an extremely large number of steps to hit such a minimum by the Monte Carlo algorithm.

- An advantage of the Monte Carlo method that shall not be left unmentioned is its ability to deal with "real" domains. If, as in a small domain, the potential energy $\sum\limits_{\mathbf{r}} V_{single}(\mathbf{r})$ is *not* a 1D potential, the optimal adsorption geometry can only result from a full potential energy calculation.

A pure lattice-matching algorithm, on the other hand, suffers from major shortcomings as well. While it yields a good overview over all epitaxial structures available, no reliable ranking among the lattices is possible.[4] An important result presented in Sections 6.2 and 8.2 concerns the strong dependency of the energetic gain V'_{inter} on the azimuthal orientation of the adsorbate ζ. If this information is neglected (as in any lattice-matching method), the ranking amongst the epitaxial phases found will most likely be wrong. This has been exemplified in Figure 6.3(a). There are ζ-values for HBC on Ag(111) for which the energetic gain in a commensurate (!) phase is basically zero. Consequently, the algorithm proposed here includes pre-calculated potential energy data.
The *LOL-predictor* algorithm is a two step process:

The first step includes the creation of a "Meta"-Gridfile, a hash table, for a specific system of a substrate and an adsorbed molecular species. This file contains $V'_{inter}(i,j,\zeta)$ values for the growth on all substrate lattice lines (i,j) with $|i|,|j| < 12$ under all azimuthal orientations ζ of the adsorbed molecules. The step width for ζ has been set to 1°. This "Meta"-Gridfile is calculated by a PowerGrid script using the algorithm outlined in Sec. 8.1.

While the first step required only the definition of the substrate and the adsorbate molecule, the second step of the *LOL-predictor* relies on some experimental input concerning the adsorbate system to produce meaningful results. The basic idea is that there is a "natural", undisturbed lattice of the adsorbate which would occur if the potential $V_{single}(\mathbf{r})$ was completely flat. As this condition cannot be realized experimentally, one should take data on substrates with a rather weak corrugation. For the examples discussed here, the lattice constants and molecular orientation of QT on Au(111) [55] as well as the (102) plane of the β modification of PTCDA has been selected (Fig. 2.5). The latter choice is motivated by the observation that all PTCDA thin films in this work exhibit a geometry close to the β phase.

In order to grow in a certain epitaxial structure, the adsorbate lattice will most probably undergo a distortion away from the "natural" lattice. The distortion is energetically unfavorable which is accounted for by an energy penalty $E_{loss} > 0$ per molecule, while the achieved epitaxial growth is rewarded by the energy $E_{gain} = V'_{inter} < 0$. These two energies have to be balanced against each other to separate favorable from unfavorable epitaxial relations. Consequently, the essential criterion is $E_{net} = E_{loss} + E_{gain}$. The energy penalty E_{loss} is calculated under the assumption of a harmonic intermolecular potential

$$V^{harmon.}_{mol-mol} = V_0 + 1/2\ k(a - a_0)^2$$

as valid for small deviations from the "natural" lattice constant(s) a_0. The force constant k with $E_{loss} = 1/2\ k(a - a_0)^2$ was determined by fitting the van

---

[4] Although the authors of Ref. 110 come to a different result, the method of a fixed adsorbate unit cell geometry used there does not allow to draw this conclusion.

der Waals potential in a HBC layer as it was discussed in Chapter 5 (Fig. 5.8). The screening parameter was set to $s = 0.45$. A value of $k = 110\,\mathrm{meV}/\text{Å}^2$ was obtained in this fit and has been used in the algorithm as an universal constant for all adsorbates tested. Naturally, the validity of this approach is limited due to the simplicity of the penalty function.

The method outlined is implemented in a PERL [111] script that repeats the following steps for each substrate lattice line $(ij)_{subst}$:

- In a fast search, all adsorbate lattice lines $(kl)_{ads}$ (based on the "natural" lattice) are selected that roughly match the periodicity of the $(ij)_{subst}$ lines.

- For each selection, an adsorbate lattice is calculated that is characterized by a perfect match between $(ij)_{subst}$ and $(kl)_{ads}$ line periodicities. As this requirement is not sufficient to yield a unique result for the lattice, a solution with a minimal energy penalty E_{loss} is searched.

- The orientation ζ of the adsorbates is derived from the lattice orientation and the value $E_{gain} = V'_{inter} < 0$ is extracted from the pre-calculated "Meta"-Gridfile.

- If $E_{net} = E_{loss} + E_{gain}$ is negative, the quadruple $(ij)(kl)$ denotes a possible candidate for an epitaxial overlayer.

Finally, all possible epitaxial structures are sorted by E_{net} as this should yield a list with the most likely POL or LOL relations on top.

The algorithm provides, for example, a quite useful tool for the analysis of LEED patterns. It is a convenient procedure to check the structures obtained from the calculation one by one in the order of energetic gain. Each structure can then be compared to the LEED pattern and is either confirmed or has to be discarded. To test the quality of the prediction, the algorithm was applied to the three systems PTCDA on HBC, QT on HBC and PTCDA on Au(111).

8.4.2 Results

The Top Five hits of the *LOL-predictor* for the system PTCDA on HBC are listed in Tab. 8.1. The HBC lattice constant was set to $a_1 = 14.0\,\text{Å}$ in accordance to LEED results and the β-phase values of PTCDA have been used as the "natural" PTCDA lattice. Besides PTCDA Phase **III** that resulted from the stacking-sequence inversion, the observed phases of PTCDA are in the Top Five list, i.e., are predicted to yield the highest net energy gain. To put this result into perspective, a total of ≈ 100 relevant epitaxial relations was checked and for ≈ 40 of them an energetic gain was predicted. It is difficult to comment on the correct order of the first four entries in the list as the net

Table 8.1: Top Five results of the *LOL-predictor* for the system of PTCDA on HBC. Experimentally observed Phases are marked in gray. Energies in meV, angles in °

i	j	k	l	E_{loss}	E_{gain}	E_{net}	δ	δ_{LEED}	Phase
-5	0	5	4	0	2.99	2.99	8.9	-	undisting. from A
0	-5	8	0	0.52	3.38	2.82	0	0	I
-5	-5	2	-5	0.30	2.56	2.26	15.5	-	not observed
1	0	0	1	5.77	7.94	2.21	30	30	II
-3	0	1	-3	0.13	1.65	1.52	17.9	-	not observed

Table 8.2: Top Five results of the *LOL-predictor* for the system of QT on HBC. The experimentally observed Phase is marked in gray. Energies in meV, angles in °

i	j	k	l	E_{loss}	E_{gain}	E_{net}	δ	δ_{LEED}	Phase
-2	1	1	2	4.90	9.41	4.51	24	23.4	Kasemann et al. [42]
1	-5	8	-1	1.34	4.55	3.21	35.2	-	not observed
-1	5	0	-4	0	1.56	1.56	38.9	-	not observed
0	-3	1	-2	0.17	1.52	1.35	18	-	not observed
0	-5	6	3	0.39	1.60	1.21	17.6	-	not observed

energetic gain E_{net} is quite similar for all of them. Here, especially the penalty function is probably too simple to produce fully reliable results.

The *LOL-predictor* results for the system QT on HBC are listed in Tab. 8.2. The HBC lattice constant was again $a_1 = 14.0\,\text{Å}$. The unit cell values found for QT on Au(111) [55] have been used as the "natural" QT lattice. For this system, the prediction is much easier to interpret. The first entry fits the experimentally observed phase of QT on HBC and clearly exceeds the energetic gain of following structures. Thus, the test on this example can be named a full success.

Finally, the *LOL-predictor* is applied to a system that it was not designed for in the first place. As POL epitaxy is, however, only a subcategory of LOL epitaxy a predication should also be possible for PTCDA on Au(111). The results are displayed in Table 8.3. Again, the β phase unit cell of PTCDA has been used in the calculation. The results illustrate the power, but also the limits of the algorithm. On the one side, the Top Five hits include all experimentally found phases of PTCDA [92]. On the other side, the predicted order amongst them is not entirely reflected in the experiment. While Phase **B** is quite dominant, the rank of the non-equilibrium phase **A** is certainly not correct.

Summarizing, the *LOL-predictor* algorithm has a very high chance of finding experimentally observed overlayer geometries. Although the first hit is not

Table 8.3: Top Five results of the *LOL-predictor* for the system of PTCDA on Au(111). Experimentally observed Phases are marked in gray. Energies in meV, angles in °

i	j	k	l	E_{loss}	E_{gain}	E_{net}	δ	δ_{LEED} [92]	Phase
0	1	5	4	0.17	11.01	10.84	40	40	B
0	-1	2	5	0.04	8.45	8.41	15.6	14.5	D
0	1	8	0	0	5.55	5.55	31.1	30.1	C
-1	0	8	-1	7.63	10.67	3.04	39.9	40	B?
1	1	7	-2	1.56	4.42	2.86	6.1	7.5	A

necessarily the dominant adsorbate phase, the overall predictive power is quite good. As only the "natural" adsorbate unit cell is required, the algorithm can be used to predict results instead of just being a tool for the interpretation of experiments. Whether a substrate-adsorbate combination is likely to form stable overlayer structures can thus be estimated without much experimental efforts.

9 General Conclusions and Future Perspectives

9.1 Conclusion

In this work, several aspects of ordered and disordered organic adsorbates on metal substrates have been reported. The thickness ranged from sub-ML regime to layers consisting of two different organic species, each at ML coverage. It was the aim to shed some light onto the question how order and disorder in these systems can be understood in terms of potential energy minimization. The work combined experimental studies by LEED and STM with theoretical models that allowed potential energy calculations for the extended films. Dealing with one- and two-component systems, there were two clear focal points. On one hand, the growth of two different hydrocarbon molecules, QT and HBC, on gold and silver substrates has been investigated and modeled with an emphasis on the intermolecular interaction *in* the layer. On the other hand, the ordering in a vertical two layer system, consisting of PTCDA and HBC molecules has been studied. Here, the focus was on the interaction *between* the layers involved.

The two main aspects concerning the modeling and calculation were, firstly, to verify the applicability of the methods to the actual physical situation and, secondly, the use of the models to generalize the experimental findings. Finally, a method was proposed that allows a prediction of overlayer geometries. It has been tested successfully on both organic-inorganic and organic-organic systems.

As it is a very important concept for this work, much space was given to a discussion of epitaxy in terms of potential energy. Phenomenological descriptions of the epitaxial relation, mainly via the epitaxial matrix, are rather inappropriate for the description of the most general type of epitaxy, the LOL epitaxy, and for the treatment of the energetic aspects of epitaxial systems. Hence, one chapter was dedicated to an approach to derive the properties of epitaxial relations entirely from energetic aspects, in particular from the periodic interface potential $V_{single}(\mathbf{r})$ and the principle of potential energy minimization.

The first large part of this work deals with the properties of large planar hydrocarbons on noble metals, namely QT and HBC on Au(111) and HBC on Ag(111). A counter-intuitive behavior, the absence of aggregation at sub-ML coverage, was observed for all systems. Due to the high symmetry of HBC and the fact that it is physisorbed on Au(111), the system HBC on Au(111) was chosen for a modeling approach. The interaction between the HBC molecules was calculated including Coulomb as well as van der Waals forces. The metal substrate was accounted for by the inclusion of mirror charges and of the pushback effect. Furthermore, a screening of the attractive London forces by the metal turned out to be a key element for the understanding of the observations made. It shows that the Coulomb forces between the positively charged hydrogen atoms provide the main mechanism for the repulsion, while the dipole emerging from the pushback effect contributes only weakly. The assumption that this mechanism is quite universal is supported by the fact that a comparable repulsive behavior has been reported only for molecules without heteroatoms in the outer rim.

A second aspect of the growth of HBC is discussed in this work. With a tunable, coverage-dependent lattice constant of the ordered phase, the question of epitaxy has to be posed in a different way. The *orientation* of the adsorbate lattice becomes the dominant aspect if not only one final epitaxial structure is relevant but epitaxial structures on the whole way may influence the final orientation. On Au(111) the surface reconstruction is found to play the most important role in orienting the adsorbate lattice. In parallel, also the influence of "classical" lattice epitaxy is observed on both substrates. In particular, a ratchet-like locking into commensurate phases is found on Au(111).

The ordering principles at the organic-organic interface have been studied on the system of a PTCDA ML on a HBC ML on Au(111). Hence, it was possible to exploit the tunable lattice constant of the HBC layer to achieve the formation of *several* highly ordered phases in one and the same system. The expected dependency was observed, although the lattice constant of HBC always decreased to the fixed value of $a_1 = 14.0\,\text{Å}$ upon deposition of PTCDA. In a combined LEED and STM study, one POL and two LOL phases of PTCDA could be identified. A comparison between the different phases in terms of potential energy gain and likeliness of occurrence could be conducted. An important aspect in that sense was the verification that the potential energy calculation yields the correct adsorption geometry, i.e., mutual alignment in a certain LOL phase. This finding increases the trust that the method is an adequate tool for a general analysis of real epitaxial systems.

In the respective chapter, a method was introduced to calculate the interface energy V_{inter} independent of a certain domain geometry. The dependency of V_{inter} on the adsorbate orientation and the influence of higher order contributions to this potential was discussed exemplarily. An important aspect is the existence of a “natural” order in the LOL coefficients. While, as a general trend, the associated energetic gain decreases with increasing indices, the inner structure of a substrate unit cell may lead to “islands” of high gain at high indices. A strong resemblance between this energetic gain and the intensity of LEED spots of the substrate was found and justified by the likeness of mathematical expressions and physical origins of both quantities. Based on the calculations of V_{inter}, a method was introduced to predict the overlayer geometry in highly ordered systems. The combination of potential energy calculations with lattice-matching methods was found to yield good results for organic-organic and organic-inorganic systems. It is thus expected that the method is applicable to a wide range of systems and provides reliable information for predictive purpose and to interpret experimental results.

9.2 Outlook

As soon as the computer performance allowed the calculation of comparatively large systems by means of DFT and Hartree-Fock techniques, the development of empirical computational methods lost its momentum. As a result, the quantitative modeling of dispersion forces in this work is based on methods which are used since several decades. The idea to replace the complex van der Waals interaction between large organic molecules by pairwise additive atom-atom potentials was feasible at times of limited computer power and allows the computation of extremely large bio-molecules today. For a broad range of physical phenomena and applications, molecules of intermediate size are of particular importance. Calculations conducted for assemblies of such molecules could considerably benefit from an improved treatment of dispersion interaction. A method more closely related to the initial idea of expressing the force as a function of the molecular polarizability should be able to account much better for the specific properties of individual molecular species. If implemented, this method would in particular account for the relative orientation of two molecules with respect to each other and would also allow a more convenient treatment of the screening effects discussed in this work. Although this cannot be proven here, today’s computational power, as well as the organic crystal and sublimation temperature data available should allow a convenient empirical parameterization of such a model, especially if combined with ab-initio calculations for small model systems.

The presented investigation concerning details of the LOL epitaxy now allows a directed search for possible new structures or systems, now not only focusing on the structural properties alone, but with the general aim of adding functionalities, i.e., special electronic properties to the heterosystems. The hypothesis of a strong resemblance between probable LOL structures and high intensity LEED reflexes should be studied more thoroughly on other systems.

If it turns out to be reliable, a method is found for very fast and model independent screening of potential LOL structures and especially the usability of the respective molecular structure for the consecutive growth of heteroepitaxial systems.

The *LOL-predictor* worked much better than initially hoped. The trust in the method can easily be increased by testing its predictive power on a few other substrate-adsorbate systems. It is probably worth the effort to improve the concept. A flexible substrate, i.e., variable substrate lattice constants, and a more elaborate penalty function can easily be incorporated into the algorithm.

Appendix

Scanning tunneling spectroscopy (STS) which refers in most cases to current-voltage spectroscopy is a suitable method to study the properties of organic adsorbates as it provides information on both, the empty and the filled electronic states in just one measurement and, in principle, on a very local scale. Here, the focus is on the question how a reliable extraction of the energetic position of the molecular states can be achieved.

A.1 Conductance in a STM: The 1D WKB model

There are two different approaches to the interpretation of STS spectra in literature: Either the differential conductivity (d.c.) dI/dV or the normalized differential conductivity (n.d.c.) $(dI/dV)/(I/V)$ is used, following the argumentation of Tersoff and Hamann [112] or Stroscio et al. [113], respectively. Besides the fact that two dissimilar methods of interpretation represent an undesirable degree of freedom, both methods have originally been proposed for the interpretation of STS results on bulk inorganic samples. The use of these methods on organic adsorbates therefore evokes a problem: A rather large tunneling voltage, compared to STS on inorganic samples, is necessary to probe the molecular resonances. This motivates a revision of the evaluation of STS measurements on organics. Quite clearly, this has to involve a model of the tunneling process. One of the most widely discussed "simple" models is the 1D model of a tunnel junction introduced below.

Later, the applicability of this 1D-WKB model to the case of orbital-mediated tunneling through a thin molecular layer on a metal substrate is discussed. For that purpose, the *complete* 1D WKB model is used to calculate the density of states (DOS). Subsequently, the DOS is compared to the known approximate approaches, i.e., the d.c. and the n.d.c. Advantages and disadvantages of both quantities are highlighted. Exemplarily, four different STS measurements from literature are discussed, including examples which exhibit negative differential resistance (NDR) effects, since the NDR phenomenon is thought to be a valuable benchmark to check the significance of any model. While the applicability of the model is presumed at first, an assessment of

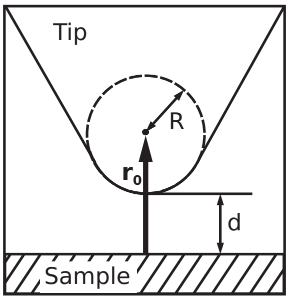

Figure A.1: Schematic picture of the tunneling geometry [112]. The tip is assumed locally spherical with a radius R.

the resulting DOS and of additional relevant parameters will later confirm or negate this assumption.

A theoretical basis for a general treatment of the tunneling process in a STM is given by Bardeen, known as the Transfer Hamiltonian approach [114].[1] Tersoff and Hamann applied this approach to a model of a flat surface and a spherical tip with an atomic s-orbital symmetry (Fig. A.1), thus creating the first *quantitative* model for the tunneling current in a STM [112]. As a result, one gets the following expression for the tunneling current I in the limit of zero temperature and very low voltages:

$$I = 32\pi^3\hbar^{-1}e^2V\Phi^2\rho_t\left(E_F\right)R^2\kappa^{-4}e^{2\kappa R} \times \sum_\nu \left|\Psi_\nu\left(\mathbf{r}_0\right)\right|^2\delta\left(E_\nu - E_F\right). \quad (A.1)$$

In this equation, I depends on the average work function $\Phi = \left(\Phi_t + \Phi_s\right)/2$ of tip and sample and on the density of states ρ_t of the tip at the Fermi level. The sample properties are represented by the value of the sample wave functions Ψ_ν with an energy E_ν at the center of curvature $\mathbf{r}_0$ of the tip (Fig. A.1), constituting the *local density of states* (LDOS). The LDOS thus represents the charge density per unit energy at E_F at a certain point above the surface [116]. From Eq. A.1 one can derive a first important relation between the LDOS and the tunneling current I(V) at very small bias, i.e., around E_F:

$$dI/dV \propto LDOS\left(E_F\right). \quad (A.2)$$

For the discussion of I(V) dependencies in STS measurements on organics, where the energy gap between the HOMO and the LUMO typically exceeds 1 eV, the limit of $V \approx 0$ is obviously inappropriate. If a sizeable bias voltage is applied, it is necessary to introduce a voltage dependence of (at least) the sample wave functions: $\Psi_\nu = \Psi_\nu\left(\mathbf{r}_0, V\right)$. An appropriate description of the tunneling process would therefore require the calculation of the sample wave functions in the electrostatic potential created between sample and tip, which is extremely complicated, especially if the tip shape is not known precisely.[2]

---

[1] For a different approach see for example [115].

[2] For a simple tip model such calculations can be found in Refs. 117 and 115.

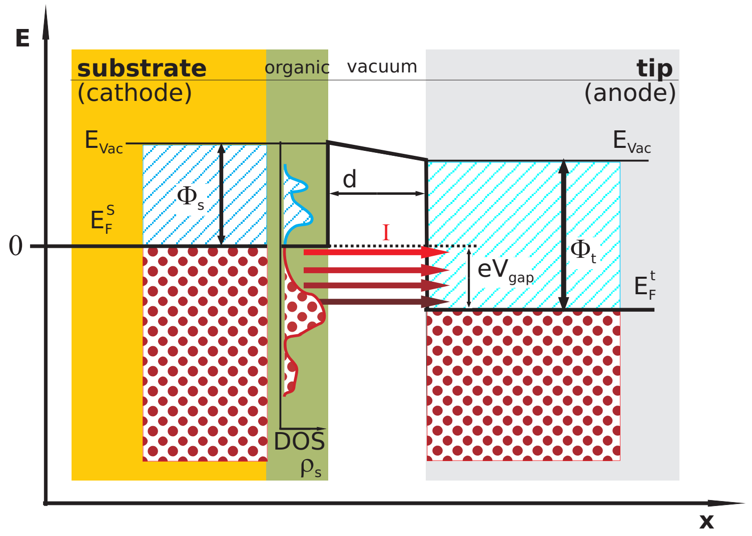

Figure A.2: The model of a one-dimensional tunnel junction with a trapezoidal barrier.

Thus, such an approach is not very useful for a general discussion of STS measurements. Instead, the standard way to introduce a voltage dependence is to use the model of a one-dimensional tunnel junction in WKB approximation.[3] The model that has first been suggested by Selloni et al. [118] and Lang [119] includes a number of approximations such as the neglect of image potential effects and inelastic tunneling, as well as the limit of zero temperature. However, by comparing the results of the full Transfer Hamiltonian calculation to the 1D WKB model in a bias voltage range of $\pm 2V$, Lang found a good agreement between both methods and concluded that "...The simple model provides a good account of the qualitative features of the results of the full calculation..." [119].

The respective equations express the tunneling current as an integral over the density of states of tip and sample and the barrier transmission function T which results from the WKB approximation, assuming a trapezoidal barrier:

$$I\left(d,V\right) \cong \frac{A\pi e\hbar^3}{2m^2} \times \int_0^{eV} T\left(d,V,E\right)\rho_s\left(E\right)\rho_t\left(E-eV\right)dE \tag{A.3}$$

with

$$T\left(d,\Phi_{s,t},V,E\right) \cong exp\left[-\frac{4}{3}\left(d+R\right)\sqrt{\frac{2m}{\hbar^2}}\left(\frac{\left(\Phi_t - E + eV\right)^{\frac{3}{2}} - \left(\Phi_s - E\right)^{\frac{3}{2}}}{\Phi_t - \Phi_s + eV}\right)\right] \tag{A.4}$$

The quantities in these equations are illustrated in Figs. A.1 and A.2.

---

[3] The Wentzel-Kramers-Brillouin-approximation or semiclassical approximation is applicable if the change in the potential $U(x)$ is small at the scale of the wavelength of Ψ.

To put this 1D WKB model into perspective, a short comparison to the Tersoff-Hamann model shall be made: The Tersoff-Hamann model aims at a more accurate description by considering individual sample wave functions, but gives no answer on how the value $|\Psi_\nu|$ at $\vec{r_0}$ should be calculated and how it changes with an applied voltage. The 1D WKB model circumvents these questions by not dealing with the wave functions directly. Instead, a density of electronic states is assumed where the individuality is reduced to a dependency on the energy E of each state. The dependencies on E and on V are then combined in the transmission function T which can be seen as a measure for the charge density of each state that reaches r_0. Thus, the quantity

$$\rho_s(E)\,T(r_0,V,E) \overset{1D\,WKB}{\equiv} LDOS(E) \tag{A.5}$$

is a generalized LDOS at r_0 in terms of the Tersoff-Hamann model.[4] From this relation, the fundamental difference between the DOS ρ_s and the LDOS of the sample becomes immediately clear. Consequently, one has to clearly distinguish between the two terms in general, notwithstanding that cases exist where LDOS and DOS bear a close resemblance to each other.

Calculating the derivative of Eq. A.3 with respect to V results in three terms:

$$\begin{aligned} \frac{dI\,(d,V)}{dV} \cong\; & A\left[eT\,(d,V,E)\,\rho_s\,(E)\,\rho_t\,(E-eV)\,|_{E=eV} \right. \\ & + \int_0^{eV} T\,(d,V,E)\,\rho_s\,(E)\,\frac{d\rho_t\,(E-eV)}{dV}dE \\ & \left. + \int_0^{eV} \frac{dT\,(d,V,E)}{dV}\rho_s\,(E)\,\rho_t\,(E-eV)\,dE \right] \end{aligned} \tag{A.6}$$

From substituting Eq. A.5 in Eq. A.6, it is evident that only for very small biases the statement $dI/dV \propto LDOS$ holds. However, for increasing bias, this relation becomes less and lesser valid, simply due to the explicit voltage dependency of T, so that the other two terms in Eq. A.6 will not vanish [120]. From this one can already conclude that the relation

$$\frac{dI}{dV} \propto \rho_s(eV)\,T\,(d,V,eV) \equiv LDOS(eV) \tag{A.7}$$

is only an approximate one. In the limit of a small bias one can even write

$$\frac{dI}{dV} \propto \rho_s(eV) \equiv DOS(eV) \tag{A.8}$$

---

[4] To highlight this analogy, not only the tip-sample distance d from Fig. A.2 is used in Eq. A.4 but $r_0 = d + R$.

by the same token, as T and ρ_t are constant. Combining Eq. A.8 and Eq. A.2 one comes to the conclusion that

$$\frac{dI}{dV} \propto DOS \propto LDOS \tag{A.9}$$

which explains why both quantities are mixed up frequently when discussing STS measurements, ignoring the fact that Eq. A.9 is only valid for small voltages.

The best and most convincing example to demonstrate the "non-proportionality" between dI/dV and the LDOS is the observation of a *negative differential resistance* (NDR), an effect that occurs especially in STS measurements on organic molecules which are separated from the metal substrate by a thin insulating layer [121, 122]. In the respective bias voltage region the current drops although the voltage is increased. Consequently, the differential conductivity dI/dV becomes negative, which cannot be the case for neither the DOS nor the LDOS, thus rendering both $dI/dV \propto LDOS$ and $dI/dV \propto DOS$ invalid. The NDR effect can, on the other hand, easily be explained by the full 1D WKB model as will be shown in the following.

A.2 Extraction of the DOS from STS measurements by means of the 1D WKB model

In Section A.1 it became obvious that the LDOS depends on the respective energy, the tip-sample distance, and the applied bias voltage. On the other hand, the sample DOS $\rho_s(E)$ depends exclusively on the energy. When performing tunneling spectroscopy at a constant tip-sample separation, there is only one free variable, the bias voltage, and thus the quantity obtained from the measurement should also depend only on one variable. Moreover, using STS as material characterization method, it is indeed the DOS one should be interested in. While a significant number of publications uses the 1D WKB model for the "forward" calculation of $I(V)$ curves, plugging in assumed tip and sample DOS distributions $\rho_t(E)$ and $\rho_s(E)$ [119, 120, 122], it shall be demonstrated here that one can invert the direction of calculation and use the model to directly calculate the DOS from measured $I(V)$ curves as a direct evaluation method.[5] In the following part, the method used will be explained briefly, and subsequently the results for four examples of STS measurements from literature will be shown.

---

[5] A comparable calculation was performed by Hamers for a STS measurement on $Si(111)-(7 \times 7)$ without giving details on the procedure used [123].

Solving the integral equation

The goal to calculate the sample DOS $\rho_s(E)$ (in terms of the 1D WKB model) from the STS $I(V)$ curve requires to solve Eq. A.3 which is a Volterra integral equation of the first kind. Although there is no analytical solution for this particular equation, it can be solved numerically, in principle, to any required accuracy. A simple but efficient method is to split up the $I(V)$ curve into a positive and a negative voltage part and to replace the integral by a numerical quadrature. For this purpose and for each polarity separately, the interval $[0, V_{max}]$ is divided into N smaller intervals of width ΔV and respective voltage steps $v_i = i\ \Delta V$. The values for ρ_s at these points are $P_i^s := \rho_s\left(ev_i\right)$ and equivalently $I_i := I\left(v_i\right)$. Then, the integral can be approximated by a sum:

$$I_j = Ce\Delta V \sum_{i=0}^{j-1} T\left(d, \Phi_{s,t}, v_j, ev_i\right) \rho_t\left(v_j, ev_i\right) P_i^s. \tag{A.10}$$

The integral kernel $T\left(d, \Phi_{s,t}, v_j, ev_i\right) \rho_t\left(v_j, ev_i\right)$ consists of two physical quantities, the transmission function T which is given by Eq. A.4 and the energy dependent tip DOS ρ_t. As the latter one is not known in most cases without further assumptions, only the *product* of tip and sample DOS can be calculated.

Since a flat tip DOS is assumed in most published STS results anyway[6], this assumption will be used here, treating ρ_t as a constant from now on and merge it with the prefactor C. The then unnecessary index "s" of P_i^s can be removed, i.e., the expression "DOS" will refer from now on always to the samples DOS, and one obtains

$$I_j = Ce\Delta V \sum_{i=0}^{j-1} T\left(d, \Phi_{s,t}, v_j, ev_i\right) P_i. \tag{A.11}$$

As the prefactor C contains the unknown value of the constant tip DOS, one can, without loss of generality, set the entire expression $Ce\Delta V$ equal to unity. No absolute value for the DOS can be obtained this way, i.e., the results are on an arbitrary scale. If one denotes the $N \times N$ coefficients $T\left(d, \Phi_{s,t}, v_j, ev_i\right)$ as a matrix $\mathbf{T}^N$ with elements T_{ji} and equivalently defines $\mathbf{I}^N = \left(I_1, \ldots, I_N\right)^\top$ and $\mathbf{P}^N = \left(P_0, \ldots, P_{N-1}\right)^\top$, Eq. A.11 can be written in matrix notation [125] as

$$\mathbf{I}^N = \mathbf{T}^N \mathbf{P}^N \tag{A.12}$$

This system of linear equations can, in principle, be solved by Gaussian elimination. As $\mathbf{T}^N$ is, however, a lower-triangular matrix, the effort is reduced to a sequential calculation of the values P_j by following the iterative rule

$$P_j = \left[I_{j+1} - \sum_{i=0}^{j-1} T_{j+1,\,i}\ P_i \right] / \ T_{j+1,\,j} \tag{A.13}$$

---

[6] For a different approach see Ref. 124.

with

$$P_0 = I_1 / \, T_{1,\,0}.$$

At least two different methods exist to calculate the coefficients T_{ji}. While the simplest approach is to set $T_{ji} = T\left(d, \Phi_{s,t}, v_j, ev_i\right)$, the Midpoint Method as recommended by Linz that yields $T_{ji} = T\left(d, \Phi_{s,t}, v_j, e\left(v_i + \Delta V/2\right)\right)$ [126] is used here.

As the $I(V)$ curve resulting from a STS measurement is already discretized in form of a list of (I, V) pairs, the voltage steps v_i and thus ΔV are given parameters. However, for the practical evaluation of Eq. A.13, it is necessary to divide the list into two subsets as mentioned above. Then, the index j in Eq. A.13 runs from 1 to $N_+ - 1$ or $N_- - 1$, respectively.

Advantageously, the computational effort for the DOS calculation proposed here is negligible on today's desktop computers, even if performed for a large set of $I(V)$ spectra. An important aspect is that the two other free variables, the tip-sample separation d and the average work function Φ can alter the result of the calculation due to their influence on T and have therefore to be discussed separately. This will be done in the next part at hand of an analytical example.

The influence of d and Φ on the transmission function

The two free variables which have an influence on the evaluation of $I(V)$ curves (as the calculation of the sample DOS by solving Eq. A.12 will be called) are the tip-sample distance d and the work functions Φ_s and Φ_t, in other words width and height of the tunneling barrier. To illustrate this effect, Fig. A.3 shows T as a normalized function of E and V for two different tip-sample distances d. As constant prefactors have already been disregarded in the derivation of Eq. A.12, the absolute value of T is not of interest anymore, but only the ratio between values of T for different points (E, V), in other words, the *slope* of T has to be considered. It is clearly visible in Fig. A.3 that the overall slope *increases* with increasing tip-sample distance while it *decreases* for a higher value of $\Phi_{s,t}$ (not shown, compare Eq. A.4).

The discussion on how the recovery of ρ is influenced by the slope of T will, for sake of clarity, be preceded by an illustration of the general impact of the transmission function on the tunneling current. Now, two cases will be discussed which can either be associated with the dashed or with the dotted red line in Fig. A.3.

Dashed line in Fig. A.3: The tunneling current carried by electrons in a state X with an energy $E_F < E_x < E_F + eV$, $V > 0$, *decreases* with increasing voltage due to the decreasing tunneling probability: $dI_x/dV < 0$. However, for negative voltages and $E_F > E_x > E_F - e\left|V\right|, V < 0$, the respective current *increases* with increasing negative voltage: $dI_x/dV > 0$. This asymmetry with

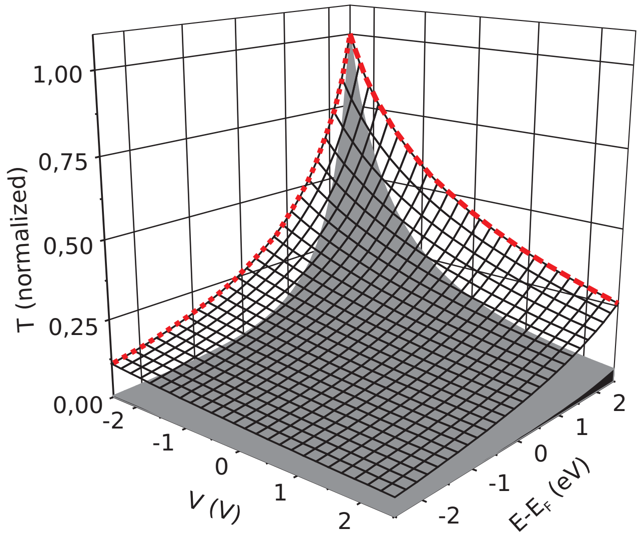

Figure A.3: Displayed is the normalized transmission function $T\left(d, \Phi_{s,t}, V, E\right)$ (Eq. (A.4)) for $\Phi_s = \Phi_t = 5$ eV and two different tip-sample distances: $d = 3.5\,\text{Å}$ (solid-gray) and $d = 1.5\,\text{Å}$ (transparent mesh). The profiles of two cuts normal to the E-V plane are marked for $d = 1.5\,\text{Å}$: $T\left(V = const, E\right)$ (red dotted line) and $T\left(V, E = const\right)$ (red dashed line).

respect to $V = 0$ includes the possibility of a decrease of the *entire* tunneling current with increasing voltage for positive bias polarity, while such a negative differential resistance (NDR) effect can be excluded for negative bias.

Dotted line in Fig. A.3: For constant bias, the tunneling probability for electrons decreases “quasi-exponentially” with its energy. This does not necessarily apply also to the respective contribution to the tunneling current which is weighted by the *number* of electrons at each energy (the DOS). The small tunneling probability for electrons in “low energy” states means, however, that a large proportion of the increase in the current with increasing negative voltage can be attributed to the effect described in the “dashed line” case above and not to the current “through” states at $E = E_F - e\,|V|$.

The choice of Φ and d for the evaluation procedure

The evaluation of experimental $I(V)$ curves by means of Eq. A.12 requires the choice of specific values for d and $\Phi_{s,t}$ and thus for the slope of T. If, as in most cases, these values have not been measured in a separate experiment [127–129], they have to be estimated. Here it is analyzed to what extent a recovered DOS curve in itself allows to determine those values.

As both parameters d and $\Phi_{s,t}$ have a comparable (but inverse) influence on the slope of T, it is, as a matter of fact, impossible to specify both values independently. Therefore, the discussion is simplified by keeping $\Phi = \Phi_s = \Phi_t$

constant at the reasonable value of 5 eV and discussing the DOS recovery exclusively in dependency on d. The argumentation given previously is the basis for the following analysis, where two scenarios, one for positive and one for negative bias polarity are discussed:

First scenario "unoccupied DOS": A potential NDR effect at positive bias can be explained by a rise of the tunneling barrier with increasing voltage. This rise and therefore also the NDR effect increases with increasing tip-sample distance (cmp. dashed line in Fig. A.3). If an $I(V)$ curve with a NDR is evaluated and the chosen value for d is too low, the *calculated* rise of the barrier and thus the decrease of $I(V)$ is weaker than in the measurement. To "compensate" for that and to generate a stronger decrease of the current, a negative value for ρ is obtained in the NDR region. This becomes trivial in the limit of $d = 0$ where the calculated DOS equals dI/dV which is inevitably negative in a NDR region. The (obvious) demand for a positive DOS thus imposes a *lower* bound for d, if a NDR effect has been observed.

Second scenario "occupied DOS": For negative bias, the current inevitably increases with increasing negative voltage. If, in the evaluation of an $I(V)$ curve, the value for d is too high, this effect is overestimated. To compensate for that and to "artificially" decrease the current to the value measured, parts of the DOS below E_F are calculated to be negative. In this case the demand for a positive DOS imposes an *upper* bound for d.

Without any additional information, the value for d which should be used to evaluate a given $I(V)$ curve cannot be determined more precisely than

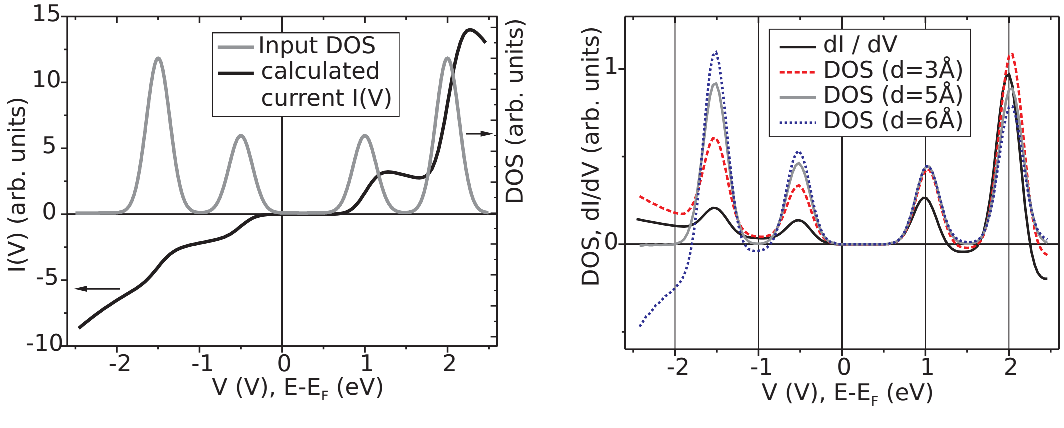

Figure A.4: **(a)** Shown is a model DOS curve with four Gaussians as representations of molecular resonances (gray) and the respective $I(V)$ curve calculated by means of Eqs. A.3 and A.4 for a flat tip DOS, $d = 5\,\text{Å}$ and $\Phi = 5\,\text{eV}$ (black). **(b)** This graph shows the results of different evaluations of the $I(V)$ curve displayed in (a). Compared are the dI/dV plot and the sample DOS ρ obtained by solving Eq. A.12 for a flat tip DOS, $\Phi = 5\,\text{eV}$ and three different tip-sample distances d. The dI/dV curve equals the DOS curve for $d = 0\,\text{Å}$.

within the limits of the upper and the (potentially existing) lower bound. An analytical example is chosen to *illustrate* the influence of different tip-sample distances on the evaluation of $I(V)$ curves. In a first step a model DOS curve is created, which exhibits general properties of a real molecular DOS, namely well separated and broadened resonances. Afterwards, the STS experiment for $d = 5\,\text{Å}$, $\Phi = 5\,\text{eV}$ is simulated by calculating an $I(V)$ curve with Eqs. A.3 and A.4 (Fig. A.4(a)). In a second step, the resulting $I(V)$ curve is evaluated by means of Eq. A.12. This is done not only for the "correct" value of $d = 5\,\text{Å}$, but also for $d = 3\,\text{Å}$ and $d = 6\,\text{Å}$, thus demonstrating the effect described above by showing that parts of the calculated DOS at positive or negative bias become negative (Fig. A.4(b)). In this analytical example, upper and lower bound for d have almost the same value of about 5 Å, leaving only this "correct" value of 5 Å as an option. However, this is not necessarily the case in the evaluation of real STS measurements.

To complete the discussion of the results given in Fig. A.4(b), it is interesting to note that, on one hand, almost no shift of the peak positions between the dI/dV plot and the three DOS curves can be observed, but on the other hand, the relative height of the peaks is strongly affected by the tip-sample distance chosen. If the usual approximation $dI/dV \propto DOS$ (Eq. A.9) is chosen, the occupied states appear therefore with strongly decreased intensity.

A.3 Practical application of the 1D WKB model

Calculation of the sample DOS for experimental I(V) curves

Using the rules to identify the maximum range for the tip-sample distance from an $I(V)$ curve, now the evaluation of $I(V)$ curves from real STS experiments on organic thin films can be conducted.

The goal to find an *unique* DOS curve belonging to a STS measurement is opposed by the uncertainty in the determination of d. As even comparably small variations in d lead to strong changes in the relative heights of the DOS peaks (Fig. A.4(b)), one should *not* expect the relative peak heights in the examples discussed in this section to be an accurate representation of the true sample DOS peak heights in the experiment, although the complete 1D WKB model and not only the differential conductivity is used for the calculation.

The applicability of the 1D WKB model will now be analyzed considering two criteria:

1. Are the values found for the upper and lower bound of the tip-sample separation reasonable, if compared to experimental findings?

2. Is the DOS curve obtained for a value d within these bounds physically meaningful?

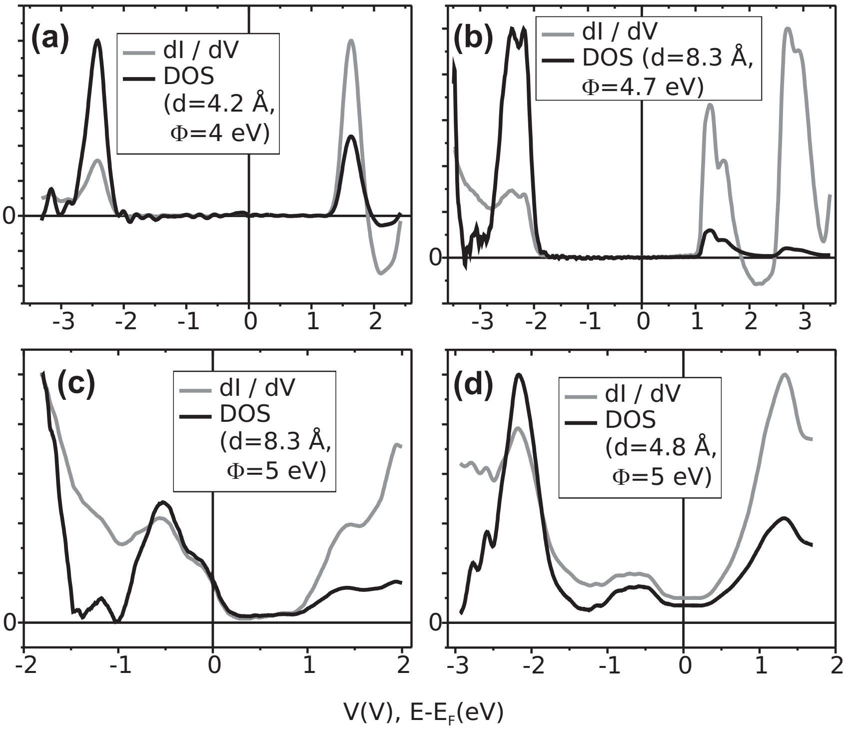

Figure A.5: Results of an evaluation with the 1D WKB model: **(a)** Repp et al. [121] **(b)** Grobis et al. [122] **(c)** Barlow et al. [130] **(d)** Tsiper et al. [131] Displayed is dI/dV versus the DOS from the calculation.

The discussion of the second criterion will be based on the interpretation given in the respective publications. The 1D WKB model is used to calculate the sample DOS for four different STS measurements from literature. A focus is put on reports demonstrating negative differential resistance, because this is the phenomenon for which the 1D WKB model is frequently used as an explanation and which is therefore most useful to demonstrate the functionality of the calculation. A second reason is given by the fact that for measurements with NDR, an upper *and* a lower bound for d can be found.

A reasonable value of 5 eV is chosen for $\Phi_{s,t}$ (except for case (a) and (b) in Fig. A.5, where a value for Φ_s of 4 eV or 4.7 eV respectively was assumed by the authors themselves [121, 122]). It is important to mention that a guess for Φ that deviates by a few 100 meV from the real value has only a weak influence on the values of the upper and lower bound for d and none at all on the conclusions drawn. To avoid ambiguity, only the DOS which was calculated using the *upper* limit for d is shown, although this is not necessarily a good guess as will become clear later. The reason for this choice lies in the fact that the upper limit is given in all four cases, while a lower limit can only be specified if a NDR is observed.

The results of the evaluation with the 1D WKB model which are displayed in Fig. A.5 are summarized here briefly:

(a) The first example in Fig. A.5 shows the evaluation of a STS measurement

from Repp et al. for individual pentacene molecules on an ultrathin NaCl layer on Cu(111) [121]. A NDR effect was observed and explained by the decoupling of metal substrate and molecules due to the NaCl layer. In this example, the upper and lower limit for d obtained from the calculation do “overlap”. As can bee seen in Fig. A.5, the DOS in the NDR region is slightly negative if calculated for the *upper* limit of $d = 4.2\,\text{Å}$. The *lower* value for d, for which the NDR effect can be explained properly by the model, is, in a clear contradiction, at approximately 10 Å.
(b) The second example shows the evaluation of a STS measurement on a C_{60} double layer on Au(111) from Grobis et al. [122]. The separation of the second monolayer from the substrate leads again to a NDR effect. The upper limit for d is 8.3 Å while the lower limit is 3.5 Å. A strong asymmetry in the density of occupied and unoccupied states is visible, while the asymmetry in the dI/dV plot is weaker.
(c) The third example shows a STS result for a CoPc layer on Au(111) from Barlow et al. [130]. As no NDR effect was observed, no lower bound for d can be determined. Figure A.5 shows the DOS for the upper bound $d = 8.3\,\text{Å}$. Again, a high asymmetry in the height of the peaks in the density of filled and empty states is visible for this particular value of d.
(d) The last example, a STS investigation by Tsiper et al., shows the result for a monolayer of PTCDA on Au(111) [131]. The upper bound for the tip-sample distance was found to be $d = 4.8\,\text{Å}$. The asymmetry in the relative height of the HOMO and LUMO peak in the DOS is small compared to example (b) and (c).

Apparently, in all calculations the density of the occupied states is higher than those of the unoccupied states. This will be discussed in more detail in the next paragraph.

Discussion of results and comparison to the differential conductivity

The results shown in Fig. A.5 allow to draw a number of reliable as well as a number of speculative conclusions. Among the former ones is the fact that the upper and, if detectable, also the lower bound for the tip-sample distance has a physically realistic value (a value of 4 Å has been found for PTCDA on S-GaAs(001) [132]). Furthermore, the position of the DOS peaks is virtually identical to the position of the respective peaks in the dI/dV curve for all examples shown. This is important as it means that the interpretation of the dI/dV peak *positions* given in the respective publications remain valid also for the calculated DOS. Obviously, the *asymmetric* transmission function T is barely influencing the positions of the peaks, while a strong influence on the relative height of the peaks is evident. In all examples, the calculated density of occupied states is higher than the density of unoccupied states, whereas a comparably weak opposite trend is visible in the respective differential con-

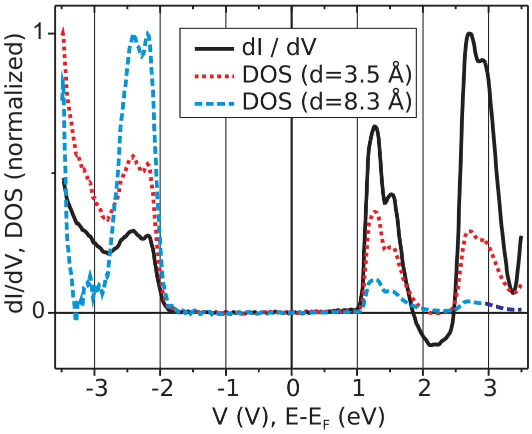

Figure A.6: Displayed is a comparison of the dI/dV plot belonging to the STS measurement by Grobis et al. [122] to two different DOS curves calculated for the upper and lower bound of the tip-sample distance d with $\Phi = 4.7\,\mathrm{eV}$.

ductivity plots. The strength of the asymmetry found in the calculated DOS curves is directly related to the tip-sample distance used: A comparably large value for d leads to a strong slope of T and thus to a pronounced asymmetry in the DOS.

It is, however, dangerous to discuss the peak heights in the DOS as well as in the dI/dV plots without further considerations. Constraints are given by the fact that the peak heights can be influenced by other effects than the 1D WKB transmission function alone, namely by the specific geometry of the involved orbitals which may not be entirely consistent with the 1D WKB model and thus result in transmission factors which are specific for each orbital [133]. A second aspect is a degeneracy of orbitals and the so called "level bunching", both resulting is a high density of states in a small energy region that cannot be resolved by STS and thus appears as one large peak (see for example Ref. [134] for electron spectroscopy results). For these very reasons, a DOS can contain peaks of quite different height. As there is, however, no physical reason for the *general* suppression of unoccupied states as it is present in *all* examples in Fig. A.5, it is rather attributed to a value of d chosen too high for the calculation.

With these qualifications, the asymmetry in the dI/dV as well as in the DOS curves can be explained consistently if one assumes the value of $d = 0$ and thus $T = const.$ to be (definitely) too small and, on the other hand, the value of the upper bound $d = d_{max}$ to overestimate the real tip-sample distance in the experiments. To illustrate this consideration, Fig. A.6 shows again the STS results of Grobis et al. (Fig. A.5 (b)) in comparison to the DOS curve for the upper *and* the lower limit for d. The DOS calculated for the lower limit $d = 3.5\,\mathrm{Å}$ exhibits a better balance in the height of the occupied and unoccupied DOS peaks than the dI/dV plot or the DOS curve for $d = 8.3\,\mathrm{Å}$, respectively.

After the analysis given here, two statements can be seen as evident: The 1D WKB model can be used successfully to evaluate STS $I(V)$ curves taken on organics and, by a rather simple argumentation, the tip-sample distance was found to be more likely below 5 Å for the cases studied.

A.4 The normalized differential conductivity

The analysis of STS evaluation procedures given here would not be complete without a discussion of the so called "normalized differential conductivity" (n.d.c.), a method that has first been suggested by Stroscio et al. [113]. The original aim of the n.d.c. was the direct comparison of STS results taken at different tip-sample separations. However, due to a number of interesting properties, the n.d.c. rapidly became a common tool for the presentation and interpretation of STS results, thus coexisting in literature with the "simple" differential conductivity. Without further discussion, the method was also transferred to the case of STS on organic samples [135–138].

The introduction of the n.d.c. was paralleled by an analysis by Lang [119] who found that for a simple model DOS, the peak position recovered by $(dI/dV)/(I/V)$ was closer to the real values than the dI/dV peak position, thus justifying the use of the n.d.c. Later, the n.d.c. was discussed in terms of the 1D WKB model by Feenstra et al. who concluded that it tends to cancel out the exponential dependencies of I and dI/dV on V and d [139]. The context in which the n.d.c. is viewed is therefore rather broad. It reaches from the mentioned cancellation of exponential backgrounds [139, 140] to the assumption that the n.d.c. is a direct measure for the sample LDOS or DOS [135, 137], while a few publications also refer to the capability of the n.d.c. to enhance features in regions with small tunneling current [136], which is reasonable as the n.d.c. can also be denoted as $d\,lnI/d\,lnV$. As the DOS can be calculated directly using the 1D WKB model, an analysis of these issues is feasible.

Two theoretical as well as two experimental examples are discussed in order to *illustrate* the relevant effects (Fig. A.7). In all cases, the normalized differential conductivity is calculated without any empirical modification (broadening or offset [141, 142]) that were developed to deal with the inherent problem of the n.d.c. in a conductance gap, where the denominator (I/V) is close to zero. Instead, the respective part of the plot (which does not hold any information anyway) is not displayed in Fig. A.7. The examples in Fig. A.7 have been chosen to represent different scenarios:

(a) A STS measurement on a model DOS is simulated using the 1D WKB model. The DOS consists of four Gaussians: Two large peaks, centered at +3 eV and -3 eV respectively, provide a background on which two (identical) smaller peaks at +1 eV and -1.5 eV are imposed. In a real experiment, the background might stem from several broad resonances ("level bunching") out-

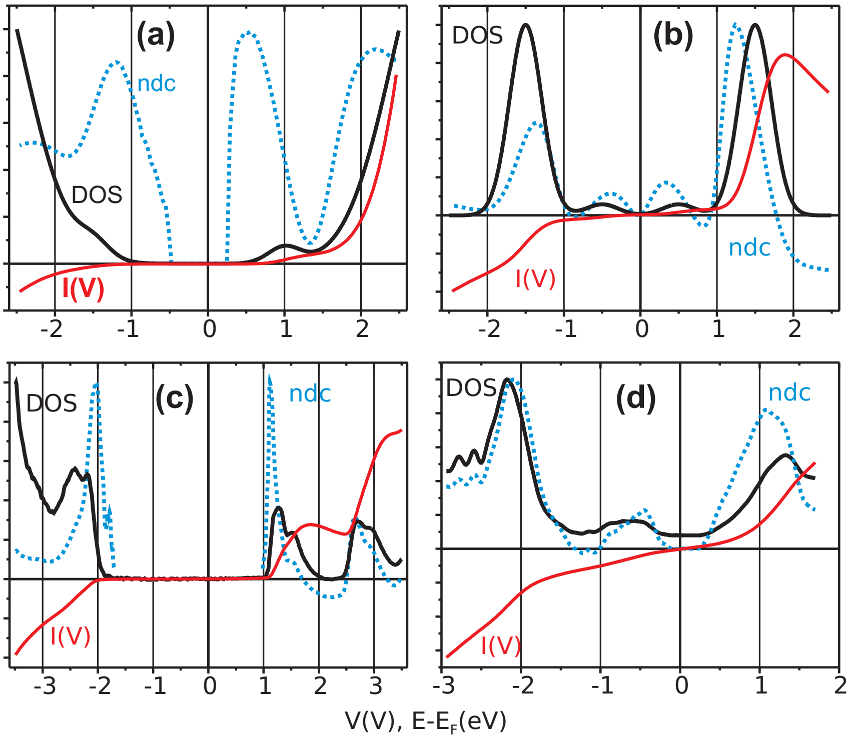

Figure A.7: Four examples of a STS evaluation using the normalized differential conductivity. Examples **(a)** and **(b)** are evaluations of $I(V)$ curves calculated for a model DOS with the 1D WKB model ($d = 5\,\text{Å}$, $\Phi = 5\,\mathrm{eV}$). Examples **(c)** and **(d)** show real STS measurements from Grobis et al. [122] and Tsiper et al. [131] (see Fig. A.5). The DOS shown was calculated for $d = 3.5\,\text{Å}$, **(c)** $\Phi = 4.7\,\mathrm{eV}$, **(d)** $\Phi = 5\,\mathrm{eV}$. As a matter of fact, the value of the n.d.c. always approaches unity at $V = 0$.

side the energy window observed. In the resulting n.d.c. curve the background is strongly reduced and the peaks are clearly visible. However, the position of the peaks is shifted by a rather large value of $0.5\,\mathrm{eV}$ and $0.3\,\mathrm{eV}$ *inwards* if compared to the peaks in the DOS.

(b) The model DOS in the second example is similar to the one shown in Fig. A.4, but with a decreased height of the inner peaks. This resembles a real STS measurement in which the contribution of HOMO and LUMO to the current is strongly suppressed for reasons (mentioned in part A.3) which go beyond the 1D WKB model [133]. One finds again a strong peak shift and, in addition, the small peaks to be more accentuated in the n.d.c. than in the DOS. This illustrates the tendency of the n.d.c. to level the peak heights within one single measurement.

(c) For the measurement from Grobis et al. [122] (Fig. A.5) the n.d.c. changes the relative heights of the peaks belonging to a double peak structure drastically, while the peak positions are affected only weakly if compared to the DOS.

(d) If the n.d.c. is calculated for the STS results from Tsiper et al. (Fig. A.5), it shows a shift of the peak at 1.3 eV while the -2.2 eV peak remains almost unchanged. Another effect is the change in shape of the Au(111) surface state around -0.5 eV which turns from a broad feature in the DOS to a clear peak in the n.d.c.

These examples offer a differentiated view onto the usability of the normalized differential conductivity for the evaluation of STS $I(V)$ spectra on organics, as desired properties are paralleled especially by unwanted peak shifts. These shifts are caused by the partially extremely high slope of the normalization function (I/V) that changes at maximum by a factor of 12 in a 0.3 V region in example (c), which clearly exceeds the real slope of the transmission function. For this reason it becomes clear that the n.d.c. is *no* useful replacement for the calculation of the DOS with the 1D WKB model in the case of organic samples. However, it cannot be denied that a subsequent normalization of the DOS *can* be useful in some cases, especially if peaks are hidden by a background or if they appear too weak as they contribute only weakly to the tunneling current (Fig. A.7(a) and (b)). In the last part of this chapter, a normalization method will be outlined that (*i*) can be used on the DOS and (*ii*) has the useful properties of the n.d.c. while the problematic peak shifts are avoided to a large extent.

A.5 A new normalization method

The aim is to develop a method that, on one hand, reduces the influence of potential backgrounds in the DOS curve recovered, and, on the other hand, emphasizes rather small peaks in regions with a low density of states. It is obviously impossible to determine the *exact* position of a peak with an unknown shape which is situated on a nonlinear background and thus visible as a shoulder only. As a sufficient and yet simple way to estimate the peak position nonetheless it is proposed to evaluate the *second* derivative of the DOS with respect to energy, which is a measure for the change in the slope of the DOS, and thus, roughly spoken, a measure for its local curvilinearity. Normally, the maximum of a peak is also the point of maximum curvilinearity, and if shoulders are considered, the x-value of maximum curvilinearity is a good measure for the position of the *original* peak (Fig. A.8).

The sign of the second derivative indicates whether the slope is increasing (positive sign) or decreasing (negative sign). The positions of peaks and shoulders in the DOS are characterized by the latter case. Therefore, the DOS peaks can be identified by looking exclusively at the *positive parts* of the quantity $-(d^2\rho/dE^2)$ as it is illustrated in Fig. A.8.

In order to emphasize small DOS peaks, an additional normalization of $-(d^2\rho/dE^2)$ by the DOS $\rho(E)$ seems appropriate. Therefore, the following

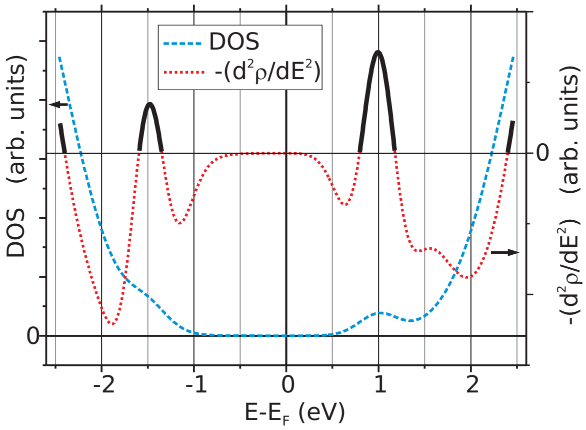

Figure A.8: Shown is the negative second derivative of the (artificial) DOS curve from Fig. A.7(a). The parts of the curve that are above zero are highlighted as they identify the two DOS peaks.

quantity has to be evaluated:

$$-\frac{d^2\rho(E)/dE^2}{\rho(E)} \tag{A.14}$$

Although peak identification is, in principle, possible using this expression, the calculation of the third derivative[7] of a measured $I(V)$ curve is not satisfactory from a practical point of view as it will, almost certainly, produce only noise. However, the explicit calculation of the second derivative of the DOS can be easily avoided by applying small modifications to the concept introduced so far. First, the second derivative is expressed as central second *difference quotient*:

$$\frac{\rho(x+\Delta x)+\rho(x-\Delta x)-2\rho(x)}{(\Delta x)^2} \tag{A.15}$$

Second, if one drops the constant factor $(\Delta x)^2$ and uses the sum of the right and left point of the interval $(x+\Delta x, x-\Delta x)$ for the normalization (rather than the central value), expression (A.14) can be written as

$$\frac{2\rho(x)-[\rho(x+\Delta x)+\rho(x-\Delta x)]}{\rho(x+\Delta x)+\rho(x-\Delta x)}. \tag{A.16}$$

As the constant offset of -1 plays absolutely no role in finding the maxima of expression (A.16), it will be neglected:

$$\frac{2\rho(x)}{\rho(x+\Delta x)+\rho(x-\Delta x)} \tag{A.17}$$

In the implementation, the method works on datasets which are given as a list of N scalar values (the DOS curve): $(V_i, \rho_i)\,,\ 0 < i \leq N$. As the main

---

[7] In this simplified view the calculation of the DOS is seen as the first derivative.

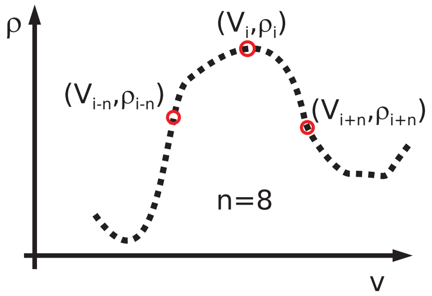

Figure A.9: The p.e.c. algorithm normalizes a DOS value ρ_i at V_i by dividing it through $(\rho_{i-n} + \rho_{i+n})/2$.

goal of the algorithm is the detection of peaks in the DOS, the result is called "*peak enhanced curve*" (p.e.c.). Following Eq. A.17, every value ρ_i is divided through the average value of two (not necessarily closest) neighbors ρ_{i-n} and ρ_{i+n}. If ρ_i marks the center of an isolated peak, both ρ_{i-n} and ρ_{i+n} should be smaller, making $2\rho_i/(\rho_{i-n} + \rho_{i+n}) > 1$ (Fig. A.9). The new (normalized) value at the i-th data point is now found by varying n within reasonable limits while searching for the maximum:

$$pec_i = \max_{0 \leq n \leq n_{max}} 2\rho_i/(\rho_{i-n} + \rho_{i+n}) \tag{A.18}$$

As results, two values are calculated for each DOS value ρ_i: A normalized value pec_i and the value n_i for which pec_i is maximal. The parameter n_{max} should be chosen in a way that $\Delta V = V_{i+n_{max}} - V_{i-n_{max}}$ equals approximately the width of a single peak at its base. Considering thermal broadening as well as broadening by inelastic effects, a value between 0.3 eV and 0.6 eV for ΔV seems reasonable. However, the functionality of the algorithm is rather tolerant with respect to the exact value of n_{max}. The lower bound of $n = 0$ guarantees that pec_i will never drop below 1. To avoid unphysical peaks resulting from noisy DOS curves, it is recommended to set all pec_i values for which n_i falls below a certain threshold parameter (for example $0.3\, n_{max}$) also to 1. This has the effect of a tunable filter, making further smoothing usually dispensable.

It has to be pointed out that the resulting curve is *not* a measure for the sample DOS anymore, but its primary aim is the identification of peaks (=molecular resonances) even if they are small or veiled by a background. The p.e.c. algorithm works rather locally as only the DOS in the interval $[V_{i-n_{max}}, V_{i+n_{max}}]$ has an influence on the normalization of ρ_i, while in the n.d.c. the total conductivity influences the result on a global scale[8]. The functionality of the p.e.c. algorithm is illustrated for the four examples from Fig. A.7 in Fig. A.10. Besides the rather small peak shift in the p.e.c. that occurs if the peaks are highly asymmetric or only present as a shoulder, two

---

[8] Example: While the outcome of the p.e.c. algorithm is not effected by the width of a conductance gap, the total conductivity and thus the n.d.c. is.

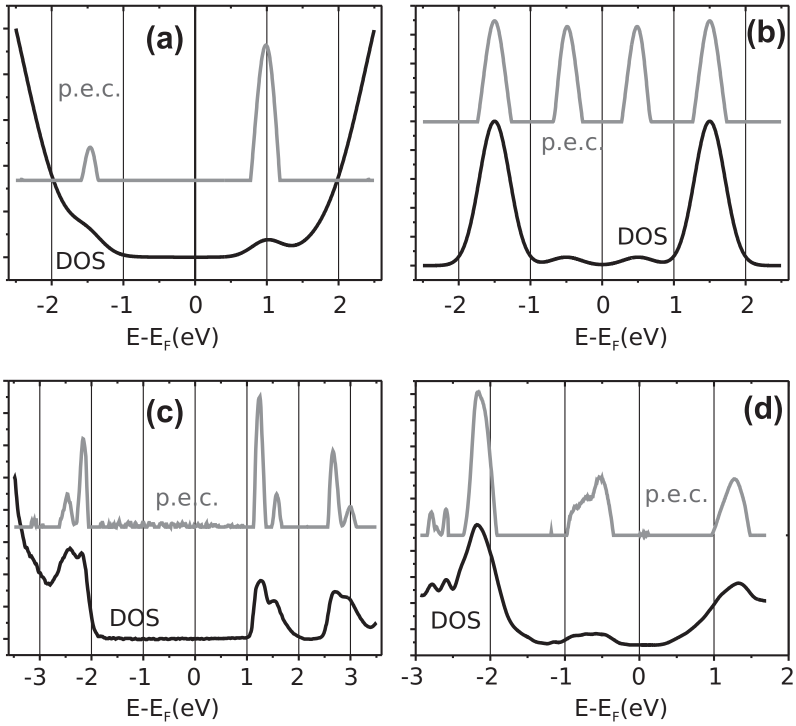

Figure A.10: Two artificial DOS curves (a), (b) and two DOS curves calculated from experimental measurements (c) Grobis et al. [122], (d) Tsiper et al. [131] are evaluated with the p.e.c. algorithm. Both experimental DOS curves are recovered for $d = 3.5\,\text{Å}$ and $\Phi = 5\,\text{eV}$. The respective parameters for the p.e.c. are: **(a)** $\Delta V = 0.5\,\text{V}$ **(b)** $\Delta V = 0.5\,\text{V}$ **(c)** $\Delta V = 0.35\,\text{V}$ and **(d)** $\Delta V = 0.6\,\text{V}$. An offset has been added to the entire DOS curve in (c) prior to the p.e.c. calculation to suppress the noise in the gap region effectively. The cutoff threshold for narrow peaks is $0.3\,n_{max}$ in all four cases.

issues are evident: The height of small peaks is indeed enhanced compared to the DOS[9] (Figs. A.10(a) and (b)), and the p.e.c.-peaks are narrower than the peaks in the DOS. This "deconvolution" is visible especially in Fig. A.10(c) where the double peak structure is clearly resolved. The background reduction as well as the narrowing of peaks can be understood if one keeps the similarity to the second derivative of the DOS in mind: Only if the first derivative is positive and decreasing or negative and increasing, the p.e.c. is larger than 1.

Concluding, a new method was outlined that has the useful properties of the n.d.c. to detect peaks but avoids strong peak shifts. It can either be used on the DOS after the recovery with the 1D WKB model or it might also be used directly on dI/dV data.

---

[9] Changes in the relative height of the peaks can be made if an offset is added to the entire curve prior to the p.e.c. calculation.

References

[1] A. Aviram and M. A. Ratner: *Molecular rectifiers.* Chem. Phys. Lett. **29**, 277 (1974).

[2] R. Jacob: *Struktur und elektronische Eigenschaften epitaktischer organischer Heterosysteme.* Diploma thesis, TU Dresden (2007).

[3] M. Eßlinger: *Hexa-peri-hexabenzocoronen auf Gold als Grundlage für organisch-organische heteroepitaktische Systeme.* Diploma thesis, TU Dresden (2009).

[4] K. Walzer, T. Toccoli, A. Pallaoro, S. Iannotta, C. Wagner, T. Fritz, and K. Leo: *Comparison of organic thin films deposited by supersonic molecular-beam epitaxy and organic molecular-beam epitaxy: The case of titanyl phthalocyanine.* Surf. Sci. **600**, 2064 (2006).

[5] M. Volmer and A. Weber: *Keimbildung in übersättigten Gebilden.* Z. Phys. Chem. **119**, 277 (1926).

[6] F. C. Frank and J. H. van der Merwe: *One-Dimensional Dislocations. I. Static Theory.* Proc. R. Soc. Lond. A **198**, 205 (1949).

[7] I. N. Stranski and L. Krastanow: Sitzungsberichte Akad. der Wiss. Wien, Math.-Naturwiss. Kl., Abt. IIB **146**, 797 (1938).

[8] T. Wagner, A. Bannani, C. Bobisch, H. Karacuban, M. Stöhr, M. Gabriel, and R. Möller: *Growth of 3,4,9,10-perylenetetracarboxylic-dianhydride crystallites on noble metal surfaces.* Org. Electron. **5**, 35 (2004).

[9] G. Binnig, H. Rohrer, C. Gerber, and E. Weibel: *Surface Studies by Scanning Tunneling Microscopy.* Phys. Rev. Lett. **49**, 57 (1982).

[10] R. Wiesendanger: *Scanning Probe Microscopy and Spectroscopy.* Cambridge University Press, Cambridge (1994).

[11] I. Horcas, R. Fernández, J. M. Gómez-Rodríguez, J. Colchero, J. Gómez-Herrero, and A. M. Baro: *WSXM: A software for scanning probe microscopy and a tool for nanotechnology.* Rev. Sci. Instrum. **78**, 013705 (2007).

[12] M. Seah and W. Dench: *Compilation of experimental data determined with various electron energies for a large variety of materials.* Surf. Interf. Anal. **1** (1979).

[13] J. J. Lander, J. Morrison, and F. Unterwald: *Improved Design and Method of Operation of Low Energy Electron Diffraction Equipment.* Rev. Sci. Instrum. **33**, 782 (1962).

[14] *Omicron SPECTALEED Manual.* Taunusstein, Germany (1997).

[15] LEEDSim by S.C.B. Mannsfeld, available from sim4tec GmbH (www.sim4tec.com).

[16] S. Mannsfeld: *Ordering in weakly bound molecular layers: Organic-inorganic and organic-organic heteroepitaxy.* Dissertation, TU Dresden (2004).

[17] C. Günther: *Organische Molekularstrahlepitaxie: Ordnungsprinzipien großer Aromaten auf Schichthalbleitern.* Logos Verlag, Berlin (1998).

[18] R. L. Park, J. E. Houston, and D. G. Schreiner: *The LEED Instrument Response Function.* Rev. Sci. Instrum. **42**, 60 (1971).

[19] T. Ogawa, K. Kuwamoto, S. Isoda, T. Kobayashi, and N. Karl: *3,4:9,10-Perylenetetracarboxylic dianhydride (PTCDA) by electron crystallography.* Acta Crystallogr., Sect. B 123 (1999).

[20] S. R. Forrest, M. L. Kaplan, P. H. Schmidt, W. L. Feldmann, and E. Yanowski: *Organic-on-inorganic semiconductor contact barrier devices.* Appl. Phys. Lett. **41**, 90 (1982).

[21] S. R. Forrest, M. L. Kaplan, and P. H. Schmidt: *Organic-on-inorganic semiconductor contact barrier diodes. I. Theory with applications to organic thin films and prototype devices.* J. Appl. Phys. **55**, 1492 (1984).

[22] K. Akers, R. Aroca, A.-M. Hor, and R. O. Loutfy: *Molecular Organization in Perylenetetracarboxylic Dianhydride Films.* J. Phys. Chem. **91**, 2954 (1987).

[23] M. Möbus, N.Karl, and T. Kobayashi: *Structure of perylene-tetracarboxylic-dianhydride thin films on alkali halide crystal substrates.* J. Cryst. Growth **116**, 495 (1992).

[24] R. Staub, M. Toerker, T. Fritz, T. Schmitz-Hübsch, F. Sellam, and K. Leo: *Scanning tunneling microscope investigations of organic heterostructures prepared by a combination of self-assembly and molecular beam epitaxy.* Surf. Sci. **445**, 368 (2000).

[25] C. Bobisch, T. Wagner, A. Bannani, and R. Möller: *Ordered binary monolayer composed of two organic molecules: Copper-phthalocyanine and 3,4,9,10-perylene-tetra-carboxylicdianhydride on Cu(111).* J. Chem. Phys. **119**, 9804 (2003).

[26] W. Chen, H. Huang, S. Chen, L. Chen, H. L. Zhang, X. Y. Gao, and A. T. S. Weea: *Molecular orientation of 3,4,9,10-perylene-tetracarboxylic-dianhydride thin films at organic heterojunction interfaces.* Appl. Phys. Lett. **91**, 114102 (2007).

[27] S. Henze, O. Bauer, T.-L. Lee, M. Sokolowski, and F. Tautz: *Vertical bonding distances of PTCDA on Au(111) and Ag(111): Relation to the bonding type.* Surf. Sci. **601**, 1566 (2007).

[28] C. Seidel, C. Awater, X. Liu, R. Ellerbrake, and H. Fuchs: *A combined STM, LEED and molecular modelling study of PTCDA grown on Ag(110).* Surf. Sci. **371**, 123 (1997).

[29] S. Mannsfeld, M. Toerker, T. Schmitz-Hübsch, F. Sellam, T. Fritz, and K. Leo: *Combined LEED and STM study of PTCDA growth on reconstructed Au(111) and Au(100) single crystals.* Org. Electron. **2**, 121 (2001).

[30] J. Wu, J. Qu, N. Tchebotareva, and K. Müllen: *Hexa-peri-hexabenzocoronene/perylenedicarboxymonoimide and diimide dyads as models to study intramolecular energy transfer.* Tetrahedron Lett. **46**, 1565 (2005).

[31] R. Goddard, M. W. Haenel, W. C. Herndon, C. Krüger, and M. Zander: *Crystallization of Large Planar Polycyclic Aromatic Hydrocarbons: The Molecular and Crystal Structures of Hexabenzo [bc,ef,hi,kl,no,qr]coronene and Benzo [1,2,3-bc:4,5,6-b'c']dicoronenene.* J. Am. Chem. Soc. **117**, 30 (1995).

[32] U. Zimmermann and N. Karl: *Epitaxial growth of coronene and hexa-peri-benzocoronene on* MoS_2(0001) *and graphite (0001): a LEED study of molecular size effects.* Surf. Sci. **268**, 296 (1992).

[33] N. Karl and C. Guenther: *Structure and Ordering Principles of Ultrathin Organic Molecular Films on Surfaces of Layered Semiconductors Organic-on-Inorganic MBE.* Cryst. Res. Technol. **34**, 243 (1999).

[34] M. Keil, P. Samori, D. A. dos Santos, T. Kugler, S. Stafström, J. D. Brand, K. Müllen, J. L. Brédas, J. P. Rabe, and W. R. Salaneck: *Influence of the Morphology on the Electronic Structure of Hexa*-peri-*hexabenzocoronene Thin Films.* J. Phys. Chem. B **104**, 3967 (2000).

[35] P. Ruffieux, O. Gröning, M. Bielmann, C. Simpson, K. Müllen, L. Schlapbach, and P. Gröning: *Supramolecular columns of hexabenzocoronenes on copper and gold (111) surfaces.* Phys. Rev. B **66**, 073409 (2002).

[36] P. Ruffieux, K. Palotás, O. Gröning, D. Wasserfallen, K. Müllen, W. A. Hofer, P. Gröning, and R. Fasel: *Site- and Orientation-Selective Anchoring of a Prototypical Molecular Building Block.* J. Am. Chem. Soc. **129**, 5007 (2007).

[37] M. Treier, P. Ruffieux, R. Schillinger, T. Greber, K. Müllen, and R. Fasel: *Living on the edge: A nanographene molecule adsorbed across gold step edges.* Surf. Sci. Lett. **602**, 84 (2008).

[38] T. Schmitz-Hübsch, F. Sellam, R. Staub, M. Törker, T. Fritz, C. Kübel, K. Müllen, and K. Leo: *Direct observation of organic-organic heteroepitaxy: perylenetetracarboxylic-dianhydride on hexa-peri-benzocoronene on highly ordered pyrolytic graphite.* Surf. Sci. **445**, 358 (2000).

[39] S. C. B. Mannsfeld, K. Leo, and T. Fritz: *Line-on-Line Coincidence: A New Type of Epitaxy Found in Organic-Organic Heterolayers.* Phys. Rev. Lett. **94**, 056104 (2005).

[40] F. Sellam, T. Schmitz-Hübsch, M. Toerker, S. Mannsfeld, H. Proehl, T. Fritz, K. Leo, C. Simpson, and K. Müllen: *LEED and STM investigations of organic-organic heterostructures grown by molecular beam epitaxy.* Surf. Sci. **478**, 113 (2001).

[41] R. Forker, D. Kasemann, T. Dienel, C. Wagner, R. Franke, K. Müllen, and T. Fritz: *Electronic Decoupling of Aromatic Molecules from a Metal by an Atomically Thin Organic Spacer.* Adv. Mater. **20**, 4450 (2008).

[42] D. Kasemann, C. Wagner, R. Forker, T. Dienel, K. Müllen, and T. Fritz: *Line-on-Line Organic-Organic Heteroepitaxy of Quaterrylene on Hexa-peri-hexabenzocoronene on Au(111).* Langmuir **25**, 12569 (2009).

[43] M. Lee, J.-W. Kim, S. Peleshanko, K. Larson, Y.-S. Yoo, D. Vaknin, S. Markutsya, and V. V. Tsukruk: *Amphiphilic Hairy Disks with Branched Hydrophilic Tails and a Hexa*-peri-*hexabenzocoronene Core.* J. Am. Chem. Soc. **124**, 9121 (2002).

[44] S. P. Brown, I. Schnell, J. D. Brand, K. Müllen, and H. W. Spiess: *The competing effects of $\pi - \pi$ packing and hydrogen bonding in a hexabenzocoronene carboxylic acid derivative : A ^1H solid-state MAS NMR investigation.* Phys. Chem. Chem. Phys. **2**, 1735 (2000).

[45] M. G. Debije, J. Piris, M. P. de Haas, J. M. Warman, Z. Tomović, C. D. Simpson, M. D. Watson, and K. Müllen: *The Optical and Charge Transport Properties of Discotic Materials with Large Aromatic Hydrocarbon Cores.* J. Am. Chem. Soc. **126**, 4641 (2004).

[46] Y. Geerts, H. Quante, H. Platz, R. Mahrt, M. Hopmeier, A. Boehm, and K. Muellen: *Quaterrylenebis(dicarboximide)s: near infrared absorbing and emitting dyes.* J. Mater. Chem. **8**, 2357 (1998).

[47] R. Hayakawa, M. Petit, T. Chikyow, and Y. Wakayama: *Analysis of carrier transport in quaterrylene thin film transistors formed by ultraslow vacuum deposition.* J. Appl. Phys. **104**, 024506 (2008).

[48] R. Hayakawa, M. Petit, T. Chikyow, and Y. Wakayama: *Interface engineering for molecular alignment and device performance of quaterrylene thin films.* Appl. Phys. Lett. **93**, 153301 (2008).

[49] C. Beck and R. Wengenmayr: *Coole Farben in heißen Autos.* Techmax **3**, 1–4 (2004).

[50] K. A. Kerr, J. P. Ashmore, and J. C. Speakman: *The Crystal and Molecular Structure of Quaterrylene: A Redetermination.* Proc. R. Soc. Lond. A **344**, 1637 (1975).

[51] J. R. Fryer and D. J. Smith: *High resolution electron microscopy of molecular crystals I. Quaterrylene, $C_{40}H_{20}$.* Proc. R. Soc. Lond. A **381**, 225 (1982).

[52] R. Hayakawa, M. Petit, Y. Wakayama, and T. Chikyow: *Growth of quaterrylene thin films on a silicon dioxide surface using vacuum deposition.* Org. Electron. **8**, 631 (2007).

[53] M. Adachi and Y. Nagao: *Design of Near-Infrared Dyes Based on π-Conjugation System Extension 2. Theoretical Elucidation of Framework Extended Derivatives of Perylene Chromophore.* Chem. Mater. **13**, 662 (2001).

[54] T. Maeda, S. Isoda, and T. Kobayashi: *Epitaxial Growth and Defect Structures of Quaterrylene Studied Using High Resolution Electron Microscopy.* Phys. Stat. Sol. (a) **191**, 489 (2002).

[55] R. Franke, S. Franke, C. Wagner, T. Dienel, T. Fritz, and S. C. B. Mannsfeld: *Epitaxial nanolayers of quaterrylene: Influence of the substrate on the growth of the first and second monolayers.* Appl. Phys. Lett. **88**, 161907 (2006).

[56] R. Forker: *Electronic Coupling Effects and Charge Transfer between Organic Molecules and Metal Surfaces.* Dissertation, Technische Universität Dresden, Institut fü Angewandte Photophysik (2009).

[57] A. Gavezzotti and G. R. Desiraju: *A Systematic Analysis of Packing Energies and Other Packing Parameters for Fused-Ring Aromatic Hydrocarbons.* Acta Cryst. B **44**, 427 (1988).

[58] C. Calandra, G. Chiarotti, U. Gradmann, K. Jacobi, F. Manghi, A. A. Maradudin, S. Y. Tong, and R. F. Wallis: *Landolt-Börnstein - Physics of Solid Surfaces*, vol. 24 of *New Series.* Springer, New York Berlin Heidelberg (1994).

[59] R. J. Needs and M. Mansfield: *Calculations of the surface stress tensor and surface energy of the (111) surfaces of iridium, platinum and gold.* J. Phys. Condens. Matter. **1**, 7555 (1989).

[60] A. R. Sandy, S. G. J. Mochrie, D. M. Zehner, K. G. Huang, and D. Gibbs: *Structure and phases of the Au(111) surface: X-ray-scattering measurements.* Phys. Rev. B **43**, 4667 (1991).

[61] C. Kittel: *Introduction to Solid State Physics.* John Wiley & Sons, Inc., New York, Chichester, Brisbane, Toronto, Singapore (1996).

[62] J. M. Cowley: *Diffraction Physics.* Elsevier, Amsterdam-Lausanne-New York-Oxford-Shannon-Tokyo (1995).

[63] J. J. P. Stewart: *Optimization of parameters for semiempirical methods I. Method.* J. Comput. Chem. **10**, 209 (1989).

[64] F. Ortmann, F. Bechstedt, and W. G. Schmidt: *Semiempirical van der Waals correction to the density functional description of solids and molecular structures.* Phys. Rev. B **73**, 205101 (2006).

[65] S. Grimme: *Semiempirical GGA-type density functional constructed with a long-range dispersion correction.* J. Comput. Chem. **27**, 1787 (2006).

[66] A. Hauschild, K. Karki, B. C. C. Cowie, M. Rohlfing, F. S. Tautz, and M. Sokolowski: *Molecular Distortions and Chemical Bonding of a Large π-Conjugated Molecule on a Metal Surface.* Phys. Rev. Lett. **94**, 036106 (2005).

[67] N. Atodiresei, V. Caciuc, P. Lazic, and S. Blügel: *Chemical versus van der Waals Interaction: The Role of the Heteroatom in the Flat Absorption of Aromatic Molecules* C_6H_6*,* C_5NH_5*, and* $C_4N_2H_4$ *on the Cu(110) Surface.* Phys. Rev. Lett. **102**, 136809 (2009).

[68] W. L. Jorgensen, D. S. Maxwell, and J. Tirado-Rives: *Development and Testing of the OPLS All-Atom Force Field on Conformational Energetics and Properties of Organic Liquids.* J. Am. Chem. Soc. **118**, 11225 (1996).

[69] W. Damm, A. Frontera, J. Tirado-Rives, and W. L. Jorgensen: *OPLS All-Atom Force Field for Carbohydrates.* J. Comput. Chem. **18**, 1955 (1997).

[70] A. K. Rappé, C. J. Casewit, K. S. Colwell, W. A. Goddard III, and W. M. Skiff: *UFF, a full periodic table force field for molecular mechanics and molecular dynamics simulation.* J. Am. Chem. Soc. **114**, 10024 (1992).

[71] S. Müllegger and A. Winkler: *Hexaphenyl thin films on clean and carbon covered Au(111) studied with TDS and LEED.* Surf. Sci. **600**, 1290 (2006).

[72] S. Lukas, S. Vollmer, G. Witte, and C. Wöll: *Adsorption of acenes on flat and vicinal Cu(111) surfaces: Step induced formation of lateral order.* J. Chem. Phys. **114**, 10123 (2001).

[73] R. Zacharia, H. Ulbricht, and T. Hertel: *Interlayer cohesive energy of graphite from thermal desorption of polyaromatic hydrocarbons.* Phys. Rev. B **69**, 155406 (2004).

[74] S. C. B. Mannsfeld and T. Fritz: *Advanced Modelling of Epitaxial Ordering of Organic Layers on Crystalline Surfaces.* Mod. Phys. Lett. B **20**, 585 (2006).

[75] R. L. Park and H. H. Madden: *Annealing changes on the (100) surface of palladium and their effect on CO adsorption.* Surf. Sci. **11**, 188 (1968).

[76] D. E. Hooks, T. Fritz, and M. D. Ward: *Epitaxy and Molecular Organization on Solid Substrates.* Adv. Mater. **13**, 227 (2001).

[77] A. Hoshino, S. Isoda, H. Kurata, and T. Kobayashi: *Scanning tunneling microscope contrast of perylene-3,4,9,10-tetracarboxylic-dianhydride on graphite and its application to the study of epitaxy.* J. Appl. Phys. **76**, 4113 (1994).

[78] B. Kuchta and R. D. Etters: *Calculated properties of monolayer and multilayer* N_2 *on graphite.* Phys. Rev. B **36**, 3400 (1987).

[79] L. W. Bruch and J. A. Venables: *Geometrical considerations in monolayer physisorption.* Surf. Sci. **148**, 167 (1984).

[80] H. Proehl, M. Toerker, F. Sellam, T. Fritz, K. Leo, C. Simpson, and K. Müllen: *Comparison of ultraviolet photoelectron spectroscopy and scanning tunneling spectroscopy measurements on highly ordered ultrathin films of hexa-peri-hexabenzocoronene on Au(111).* Phys. Rev. B **63**, 205409 (2001).

[81] R. Franke: *Epitaxial nanolayers of large organic molecules: Quaterrylenes on organic and inorganic substrates.* Dissertation, TU Dresden (2007).

[82] L. Gross, F. Moresco, P. Ruffieux, A. Gourdon, C. Joachim, and K.-H. Rieder: *Tailoring molecular self-organization by chemical synthesis: Hexaphenylbenzene, hexa-peri-hexabenzocoronene, and derivatives on Cu(111).* Phys. Rev. B **71**, 165428 (2005).

[83] L. Gao, Z. T. Deng, W. Ji, X. Lin, Z. H. Cheng, X. B. He, D. X. Shi, and H.-J. Gao: *Understanding and controlling the weakly interacting interface in perylene/Ag(110).* Phys. Rev. B **73**, 075424 (2006).

[84] C. Seidel, R. Ellerbrake, L. Gross, and H. Fuchs: *Structural transitions of perylene and coronene on silver and gold surfaces: A molecular-beam epitaxy LEED study.* Phys. Rev. B **64**, 195418 (2001).

[85] S. Müllegger, I. Salzmann, R. Resel, G. Hlawacek, C. Teichert, and A. Winkler: *Growth kinetics, structure, and morphology of para-quaterphenyl thin films on gold(111).* J. Chem. Phys. **121**, 2272 (2004).

[86] W. X. Huang and J. M. White: *Growth and Orientation of Naphthalene Films on Ag(111).* J. Phys. Chem. B **108**, 5060 (2004).

[87] I. Fernandez-Torrente, S. Monturet, K. J. Franke, J. Fraxedas, N. Lorente, and J. I. Pascual: *Long-Range Repulsive Interaction between Molecules on a Metal Surface Induced by Charge Transfer.* Phys. Rev. Lett. **99**, 176103 (2007).

[88] C. Stadler, S. Hansen, I. Kröger, C. Kumpf, and E. Umbach: *Tuning intermolecular interaction in longrange-ordered submonolayer organic films.* Nature Phys. **5**, 153 (2009).

[89] HyperChem by Hypercube, Inc. (www.hyper.com).

[90] N. D. Lang and W. Kohn: *Theory of Metal Surfaces: Induced Surface Charge and Image Potential.* Phys. Rev. B **7**, 3541 (1973).

[91] P. C. Rusu, G. Giovannetti, C. Weijtens, R. Coehoorn, and G. Brocks: *Work Function Pinning at Metal-Organic Interfaces.* J. Phys. Chem. C **113**, 9974 (2009).

[92] L. Kilian, E. Umbach, and M. Sokolowski: *A refined structural analysis of the PTCDA monolayer on the reconstructed Au(111) surface- "Rigid or distorted carpet?".* Surf. Sci. **600**, 2633 (2006).

[93] I. Chizhov, A. Kahn, and G. Scoles: *Initial growth of 3,4,9,10-perylenetetracarboxylic-dianhydride (PTCDA) on Au(111): a scanning tunneling microscopy study.* J. Cryst. Growth **208**, 449 (2000).

[94] H. Ishii, K. Sugiyama, E. Ito, and K. Seki: *Energy Level Alignment and Interfacial Electronic Structures at Organic/Metal and Organic/Organic Interfaces.* Adv. Mater. **11**, 605 (1999).

[95] Y. Zou, L. Kilian, A. Schöll, T. Schmidt, R. Fink, and E. Umbach: *Chemical bonding of PTCDA on Ag surfaces and the formation of interface states.* Surf. Sci. **600**, 1240 (2006).

[96] J. Mahanty: *Screening of the intermolecular van der Waals interaction at a metal surface.* Phys. Rev. B **35**, 4113 (1987).

[97] O. Sinanoglu and K. S. Pitzer: *Interactions between Molecules Adsorbed on a Surface.* J. Chem. Phys. **32**, 1279 (1960).

[98] A. D. McLachlan: *Van der Waals forces between an atom and a surface.* Mol. Phys. **7**, 381 (1964).

[99] D. Langbein: *Springer Tracts in modern physics Vol. 72: Theory of Van der Waals Attraction.* Springer-Verlag Berlin Heidelberg New York (1974).

[100] J. Israelachvili: *Intermolecular & Surface Forces.* Academic Press - London, Amsterdam, Burlington, San Diego (2006).

[101] W. Hendel, Z. Khan, and W. Schmidt: *Hexa-peri-benzocoronene, a candidate for the origin of the diffuse interstellar visible absorption bands?* Tetrahedron **42**, 1127 (1986).

[102] A. Pulisciano, S. J. Park, and R. E. Palmera: *Surface plasmon excitation of Au and Ag in scanning probe energy loss spectroscopy.* Appl. Phys. Lett. **93**, 213109 (2008).

[103] D. Kasemann: *Präparation und Charakterisierung von epitaktischen Doppel- und Mischschichten aus Quaterrylen und anderen Aromaten.* Diploma thesis, TU Dresden (2006).

[104] J. K. Gimzewski, S. Modesti, C. Gerber, and R. R. Schlittler: *Observation of a new Au(111) reconstruction at the interface of an adsorbed C_{60} overlayer.* Chem. Phys. Lett. **213**, 401 (1993).

[105] W. Chen, V. Madhavan, T. Jamneala, and M. F. Crommie: *Scanning Tunneling Microscopy Observation of an Electronic Superlattice at the Surface of Clean Gold.* Phys. Rev. Lett. **80**, 1469 (1998).

[106] S. Reineke, F. Lindner, G. Schwartz, N. Seidler, K. Walzer, B. Lüssem, and K. Leo: *White organic light-emitting diodes with fluorescent tube efficiency.* Nature **459**, 234 (2009).

[107] C. D. Simpson, J. Wu, M. D. Watson, and K. Müllen: *From graphite molecules to columnar superstructures - an exercise in nanoscience.* J. Mater. Chem. **14**, 494 (2004).

[108] M. Campione: *Rubrene Heteroepitaxial Nanostructures With Unique Orientation.* J. Phys. Chem. C **112**, 16178 (2008).

[109] M. Campione, L. Raimondo, M. Moret, P. Campiglio, E. Fumagalli, and A. Sassella: *Organic-Organic Heteroepitaxy of Semiconductor Crystals: α-Quaterthiophene on Rubrene.* Chem Mater. **21**, 4859 (2009).

[110] J. A. Last, D. E. Hooks, A. C. Hillier, and M. D. Ward: *The Physicochemical Origins of Coincident Epitaxy in Molecular Overlayers: Lattice Modeling vs Potential Energy Calculations.* J. Phys. Chem. B **103**, 6723 (1999).

[111] J. K. Ousterhout: *Scripting: Higher-Level Programming for the 21st Century.* IEEE Computer **31**, 23 (1998).

[112] J. Tersoff and D. R. Hamann: *Theory and Application for the Scanning Tunneling Microscope.* Phys. Rev. Lett. **50**, 1998 (1983).

[113] J. A. Stroscio, R. M. Feenstra, and A. P. Fein: *Electronic Structure of the Si(111)2x1 Surface by Scanning-Tunneling Microscopy.* Phys. Rev. Lett. **57**, 2579 (1986).

[114] J. Bardeen: *Tunneling from a Many-Particle Point of View.* Phys. Rev. Lett. **6**, 57 (1961).

[115] F. R. Zypman and L. F. Fonseca: *Electron-diffraction effects on scanning tunneling spectroscopy.* Phys. Rev. B **55**, 15912 (1997).

[116] J. Tersoff and D. R. Hamann: *Theory of the scanning tunneling microscope.* Phys. Rev. B **31**, 805 (1985).

[117] F. R. Zypman, L. F. Fonseca, and Y. Goldstein: *Theory of tunneling spectroscopy for semiconductors.* Phys. Rev. B **49**, 1981 (1994).

[118] A. Selloni, P. Carnevali, E. Tosatti, and C. D. Chen: *Voltage-dependent scanning-tunneling microscopy of a crystal surface: Graphite.* Phys. Rev. B **31**, 2602 (1985).

[119] N. D. Lang: *Spectroscopy of single atoms in the scanning tunneling microscope.* Phys. Rev. B **34**, 5947 (1986).

[120] V. A. Ukraintsev: *Data evaluation technique for electron-tunneling spectroscopy.* Phys. Rev. B **53**, 11176 (1996).

[121] J. Repp, G. Meyer, S. M. Stojković, A. Gourdon, and C. Joachim: *Molecules on Insulating Films: Scanning-Tunneling Microscopy Imaging of Individual Molecular Orbitals.* Phys. Rev. Lett. **94**, 026803 (2005).

[122] M. Grobis, A. Wachowiak, R. Yamachika, and M. F. Crommie: *Tuning negative differential resistance in a molecular film.* Appl. Phys. Lett. **86**, 204102 (2005).

[123] R. J. Hamers: *Scanning Tunneling Microscopy and Spectroscopy Theory, Techniques, and Applications*, chap. 4, 75–80. VCH (1993).

[124] A. I. Onipko, K.-F. Berggren, Y. O. Klymenko, L. I. Malysheva, J. J. W. M. Rosink, L. J. Geerligs, E. van der Drift, and S. Radelaar: *Scanning tunneling spectroscopy on π-conjugated phenyl-based oligomers: A simple physical model.* Phys. Rev. B **61**, 11118 (2000).

[125] D. Colton, H. Engl, A. Louis, J. McLaughlin, and W. Rundell (Eds.): *Surveys on Solution Methods for Inverse Problems*, 68. Springer-Verlag (2000).

[126] P. Linz: *Numerical methods for Volterra integral equations of the first kind.* The Computer Journal **12**, 393 (1969).

[127] B. Koslowski, C. Dietrich, A. Tschetschetkin, and P. Ziemann: *Evaluation of scanning tunneling spectroscopy data: Approaching a quantitative determination of the electronic density of states.* Phys. Rev. B **75**, 035421 (2007).

[128] M. Passoni, F. Donati, A. L. Bassi, C. S. Casari, and C. E. Bottani: *Recovery of local density of states using scanning tunneling spectroscopy.* Phys. Rev. B **79**, 045404 (2009).

[129] B. Koslowski, H. Pfeifer, and P. Ziemann: *Deconvolution of the electronic density of states of tip and sample from scanning tunneling spectroscopy data: Proof of principle.* Phys. Rev. B **80**, 165419 (2009).

[130] D. E. Barlow, L. Scudiero, and K. W. Hipps: *Scanning Tunneling Microscopy Study of the Structure and Orbital-Mediated Tunneling Spectra of Cobalt(II) Phthalocyanine and Cobalt(II) Tetraphenylporphyrin on Au(111): Mixed Composition Films.* Langmuir **20**, 4413 (2004).

[131] E. Tsiper, Z. Soos, W. Gao, and A. Kahn: *Electronic polarization at surfaces and thin films of organic molecular crystals: PTCDA.* Chem. Phys. Lett. **360**, 47 (2002).

[132] N. Nicoara, O. Custance, D. Granados, J. M. García, J. M. Gómez-Rodríguez, A. M. Baró, and J. Méndez: *Scanning tunnelling microscopy and spectroscopy on organic PTCDA films deposited on sulfur passivated GaAs(001).* J. Phys. Condens. Matter. **15**, 2619 (2003).

[133] P. Sautet and M.-L. Bocquet: *Shape of molecular adsorbates in STM images: A theoretical study of benzen on Pt(111).* Phys. Rev. B **53**, 4910 (1996).

[134] I. Hill, A. Kahn, J. Cornil, D. dos Santos, and J. Bredas: *Occupied and unoccupied electronic levels in organic π-conjugated molecules: comparison between experiment and theory.* Chem. Phys. Lett. **317**, 444 (2000).

[135] R. Strohmaier, C. Ludwig, J. Petersen, B. Gompf, and W. Eisenmenger: *STM investigations of NTCDA on weakly interacting substrates.* Surf. Sci. **351**, 292 (1996).

[136] P. G. Collins, J. C. Grossman, M. Côté, M. Ishigami, C. Piskoti, S. G. Louie, M. L. Cohen, and A. Zettl: *Scanning Tunneling Spectroscopy of C_{36}.* Phys. Rev. Lett. **82**, 165 (1999).

[137] M. Törker, T. Fritz, H. Pröhl, R. Gutierrez, F. Großmann, and R. Schmidt: *Electronic transport through occupied and unoccupied states of an organic molecule on Au: Experiment and theory.* Phys. Rev. B **65**, 245422 (2002).

[138] C. Baldacchini, C. Mariani, M. G. Betti, L. Gavioli, M. Fanetti, and M. Sancrotti: *Molecular gap and energy level diagram for pentacene adsorbed on filled d-band metal surfaces.* Appl. Phys. Lett. **89**, 152119 (2006).

[139] R. M. Feenstra, J. A. Stroscio, and A. P. Fein: *Tunneling spectroscopy of the Si(111)2x1 surface.* Surf. Sci. **181**, 295 (1987).

[140] W. Deng and K. W. Hipps: *Tip-Sample Distance Dependence in the STM-Based Orbital-Mediated Tunneling Spectrum of Nickel(II) Tetraphenylporphyrin Deposited on Au(111).* J. Phys. Chem. B **107**, 10736 (2003).

[141] P. Mårtensson and R. M. Feenstra: *Geometric and electronic structure of antimony on the GaAs(110) surface studied by scanning tunneling microscopy.* Phys. Rev. B **39**, 7744 (1989).

[142] M. Prietsch, A. Samsavar, and R. Ludeke: *Structural and electronic properties of the Bi/GaP(110) interface.* Phys. Rev. B **43**, 11850 (1991).

List of Figures

List of Tables

Abbreviations

1D	one dimensional
2D	two dimensional
3D	three dimensional
bcc	body-centered cubic
CCD	charge-coupled device
d.c.	differential conductivity
DFT	density functional theory
DOS	density of states
fcc	face-centered cubic
FFT	fast Fourier transform
GCD	greatest common divisor
HBC	hexa-*peri*-hexabenzocoronene
hcp	hexagonal close-packed
HOMO	highest occupied molecular orbital
HOPG	highly oriented pyrolytic graphite
LDOS	local density of states
LEED	low-energy electron diffraction
LJ	Lennard-Jones
LOL	line-on-line
LUMO	lowest unoccupied molecular orbital
ML	monolayer
n.d.c.	normalized differential conductivity
NDR	negative differential resistance
OFET	organic field-effect transistor
OLED	organic light-emitting diode
OMBE	organic molecular beam epitaxy

OPLS	optimized potentials for liquid simulations
p.e.c.	peak enhanced curve
Pc	phthalocyanine
PE	potential energy
PM3	parameterized model number 3
POL	point-on-line
PTCDA	3,4,9,10-perylenetetracarboxylic dianhydride
QT	quaterrylene
SFM	scanning force microscopy
SPA-LEED	spot profile analysis-low energy electron diffraction
STM	scanning tunneling microscope / microscopy
STS	scanning tunneling spectroscopy
TDS	thermal desorption spectroscopy
TTF	tetrathiafulvalene
UFF	universal force field
UHV	ultra-high vacuum
UPS	ultraviolet photoelectron spectroscopy
WKB	Wentzel-Kramers-Brillouin

Publications

Several parts of this dissertation have been published in peer-reviewed scientific journals and/or presented at international conferences. In the following, all contributions submitted so far are listed chronologically.

Articles

A1 R. Franke, S. Franke, S. C. B. Mannsfeld, C. Wagner, T. Dienel, and T. Fritz: *Epitaxial nanolayers of quaterrylene: Influence of the substrate on the growth of the first and second monolayers.* Appl. Phys. Lett. **88**, 161907 (2006).

A2 K. Walzer, T. Toccoli, A. Pallaoro, S. Iannotta, C. Wagner, T. Fritz, and K. Leo: *Comparison of organic thin films deposited by supersonic molecular-beam epitaxy and organic molecular-beam epitaxy: The case of titanyl phthalocyanine.* Surf. Sci. **600**, 2064 (2006).

A3 C. Wagner, R. Franke, and T. Fritz: *Evaluation of I(V) curves in scanning tunneling spectroscopy of organic nanolayers.* Phys. Rev. B **75**, 235432 (2007).
(Selected for July 2, 2007 issue of Virtual Journal of Nanoscale Science & Technology)

A4 C. Wagner, R. Franke, T. Dienel, R. Forker, R. Jacob, and T. Fritz: *Degradation and segregation: Thermal stability and highly ordered epitaxial thin films of large aromatic molecules.* Appl. Phys. Lett. **91**, 113111 (2007).

A5 R. Forker, D. Kasemann, T. Dienel, C. Wagner, R. Franke, K. Müllen, and T. Fritz: *Electronic Decoupling of Aromatic Molecules from a Metal by an Atomically Thin Organic Spacer.* Adv. Mater. **20**, 4450 (2008)

A6 D. Kasemann, C. Wagner, R. Forker, T. Dienel, K. Müllen, and T. Fritz: *Line-on-Line Organic-Organic Heteroepitaxy of Quaterrylene on Hexa-peri-hexabenzocoronene on Au(111).* Langmuir **25**, 12569 (2009)

A7 C. Wagner, D. Kasemann, C. Golnik, R. Forker, M. Esslinger, K. Müllen, and T. Fritz: *Repulsion Between Molecules on a Metal: (Sub-) Monolayers of Hexa-peri-hexabenzocoronene on Au(111).* Phys. Rev. B (2009), accepted for publication

A8 C. Weiss, C. Wagner, C. Kleimann, F.S. Tautz, and R. Temirov: *Imaging Pauli repulsion in scanning tunneling microscopy.*
Phys. Rev. Lett. (2009), submitted

Talks

T1 R. Franke, C. Wagner, S. Franke, and T. Fritz: *Organic small band semiconductors: STM and STS studies on the growth and electronic properties of quaterrylenes on Au.* ECOSS 23, Berlin, Germany (2005)

T2 C. Wagner, R. Franke, S. Franke, and T. Fritz: *The Influence of Substrate and Substituents on the Growth of Quaterrylene Derivatives on Gold.* DPG-Spring meeting, Dresden, Germany (2006)

T3 R. Franke, C. Wagner, S. Franke, and T. Fritz: *Organic small bandgap semiconductors: Electronic properties of quaterrylene derivatives on Au(111).* DPG-Spring meeting, Dresden, Germany (2006)

T4 R. Franke, C. Wagner, S. Franke, S.C.B. Mannsfeld, and T. Fritz: *Epitaxial Nanolayers of Organic Small Band Gap Semiconductors: Growth and Electronic Properties of Quaterrylenes on Au.* AVS 53, San Francisco, USA (2006)

T5 C. Wagner, R. Franke, and T. Fritz: *The Evaluation of I(V) Curves in Scanning Tunnelling Spectroscopy of Organic Nanolayers Revisited.* DPG-Spring meeting, Regensburg, Germany (2007)

T6 C. Wagner: *The Evaluation of I(V) Curves in Scanning Tunnelling Spectroscopy of Organic Nanolayers Revisited.* Minerva-School 2006, Safed, Israel (2007)

T7 C. Wagner, R. Forker, and T. Fritz: *Multiple distance scanning tunneling spectroscopy of organic layers.* DPG-Spring meeting, Berlin, Germany (2008)

T8 C. Wagner, M. Esslinger, D. Kasemann, and T. Fritz: *Multiple Distance Scanning Tunneling Spectroscopy of Organic Layers.* ICN+T 2008, Keystone (Colorado), USA (2008)

T9 C. Wagner, D. Kasemann, M. Esslinger, R. Forker, C. Golnik, and T. Fritz: *A quantitative model for the monolayer growth of hydrocarbons on noble metals: HBC on Ag(111) and Au(111).* DPG-Spring meeting, Dresden, Germany (2009)

T10 R. Forker, C. Golnik, C. Wagner, M. Esslinger, and T. Fritz: *In-situ optical spectroscopy of ultrathin quaterrylene films epitaxially grown on graphite and mica.* DPG-Spring meeting, Dresden, Germany (2009)

Posters

P1 C. Wagner, R. Franke, and T. Fritz: *Structure and Electronic Properties: The Case of QTCDI on Au(111).* Niels Bohr Summer Institute 2005, Copenhagen, Denmark (2005)

P2 C. Wagner, R. Franke, T. Fritz: *The Evaluation of I(V)-Curves in STS of Organic Nanolayers Revisited.* SPS'06 & SPSTM-1, Hamburg, Germany (2006)

P3 D. Kasemann, R. Franke, C. Wagner, and T. Fritz: *Quaterrylene and HBC on Au(111), Explored by STM / STS.* SPS'06 & SPSTM-1, Hamburg, Germany (2006), SFB624-Symposium, Bonn, Germany (2006)

P4 D. Kasemann, R. Franke, C. Wagner, R. Forker, and T. Fritz: *Epitaxial Heterolayers of Quaterrylene and HBC on Au(111).* 383th WE Heraeus-Seminar, Bad Honnef, Germany (2007)

P5 C. Wagner, R. Franke, S. Franke, T. Dienel, R. Forker and T. Fritz: *Ordering of large aromatic hydrocarbons on surfaces: The influence of substituents on the growth of quaterrylene derivatives.* ICN+T2007, Stockholm, Sweden (2007)

P6 R. Jacob, C. Wagner, T. Dienel, and T. Fritz: *Interface energetics in highly ordered organic-organic heterosystems: Thermal induced layer swap in the system HBC on PTCDA*. DPG-Spring meeting, Berlin, Germany (2008)

P7 C. Wagner, D. Kasemann, R. Forker, M. Esslinger and T. Fritz: *Tailoring and properties of highly ordered organic-organic heterojunctions: Epitaxy of large aromatic hydrocarbons.* Max Bergmann Seminar 2008, Dresden, Germany (2008)

Danksagung

Die folgenden Danksagungen sind mit dem Abschluss eines Lebensabschnitts verbunden, an den ich mich sehr gerne erinnere. An dieser Stelle möchte ich allen danken, die zum Gelingen dieser Arbeit beigetragen haben. Besonderer Dank gilt

- Prof. Karl Leo für die Möglichkeit, meine Dissertation an seinem Institut anfertigen zu können. Die sehr gute Ausstattung und angenehme Atmosphäre haben ihren Teil zum Gelingen dieser Arbeit beigetragen.

- Prof. Torsten Fritz für die hervorragende unmittelbare Betreuung in seiner Arbeitsgruppe, für viele Diskussionen, Rat- und Vorschläge, die mir oft den Tag gerettet haben. Seine lockere und angenehme Art, die OMBE AG zu leiten, werde ich in freundlicher Erinnerung behalten.

- Prof. Friedrich Th. Reinert für sein Interesse am Thema meiner Arbeit und die bereitwillige Übernahme des Zweitgutachtens.

Allen meinen Bürogenossen am IAPP, in order of appearance and disappearance: Robert Franke, Sebastian Franke, Daniel Kasemann, Reiner Jacob, Christian Golnik, Moritz Eßlinger, Roman Forker, Torben Menke und Axel Fischer sowie den weiteren (ehemaligen) Mitgliedern der OMBE Gruppe möchte ich für ihre große Hilfsbereitschaft danken, sowie für viel Unterhaltsames, das den gemeinsamen Büro- und Laboralltag nie eintönig hat werden lassen. Spezieller Dank gilt

- Dr. Stefan Mannsfeld für zwei großartige Stückchen Software, LEEDSim und PowerGrid, auf die unsere Arbeitsgruppe zugreifen konnte. Insbesondere die Nutzung des frei programmierbaren PowerGrid Interpreters hat die Arbeit oft erleichtert oder sogar erst ermöglicht.

- Rainer Jacob und Moritz Eßlinger, deren Diplomarbeiten ich begleiten konnte, für das große Engagement und die Begeisterungsfähigkeit für und bei der gemeinsamen Arbeit, speziell auch in Zeiten, die eher durch Rückschläge und Verzögerungen gekennzeichnet waren.

- Torben Menke und Roman Forker für die Hilfe und Orientierung in den Tiefen der LaTex-Formatierung. Roman weiterhin für die vielen Tipps und Hinweise, die die Erstellung dieser Arbeit für mich beschleunigt und vereinfacht haben.

Natürlich gab und gibt es eine Zeit vor und nach der Dissertation und sogar während des Schreibens verbringt man, entgegen anders lautender Vorurteile, nicht den ganzen Tag im Büro. Daher möchte ich auch meiner Familie und insbesondere meinen Eltern recht herzlich für die jahrelange Unterstützung und Förderung in allen Lebenslagen und -bereichen danken. Ein ganz wichtiger Dank gilt meiner Frau Anna-Maria für ihre Liebe, ihren Optimismus und ihr Verständnis für lange Arbeitstage. Um so mehr, als dass es nicht ganz leicht war, mir seit der Geburt unserer Tochter, deren erstes Lebensjahr mit dem letzten Jahr dieser Dissertation zusammenfällt, stets den Rücken frei zu halten. Schlussendlich danke ich meiner Tochter Paula Elena dafür, dass sie es immer ganz schnell geschafft hat, dass ich zu Hause die Arbeit hinter mir lassen und den Kopf frei kriegen konnte.

Erklärung

Diese Dissertation wurde am Institut für Angewandte Physik/Photophysik der Fakultät Mathematik und Naturwissenschaften an der Technischen Universität Dresden unter wissenschaftlicher Betreuung von Prof. Dr. Karl Leo angefertigt.

Hiermit versichere ich, dass ich die vorliegende Arbeit ohne unzulässige Hilfe Dritter und ohne Benutzung anderer als der angegebenen Hilfsmittel angefertigt habe; die aus fremden Quellen direkt oder indirekt übernommenen Gedanken sind als solche kenntlich gemacht. Die Arbeit wurde bisher weder im Inland noch im Ausland in gleicher oder ähnlicher Form einer anderen Prüfungsbehörde vorgelegt.

Ich versichere weiterhin, dass keinerlei frühere Promotionsverfahren stattgefunden haben.

Ich erkenne die Promotionsordnung der Fakultät Mathematik und Naturwissenschaften an der Technischen Universität Dresden vom 20.03.2000, in der Fassung der vom Fakultätsrat am 19.06.2002 und 12.07.2002 beschlossenen und mit Erlass des Sächsischen Staatsministeriums für Wissenschaft und Kunst vom 18.03.2003 genehmigten Änderungen gemäß Satzung vom 16.04.2003 sowie gemäß der Änderungssatzung vom 17.07.2008, an.

Christian Wagner
Dresden, den 21.12.2009